INAUGURAL–DISSERTATION
zur
Erlangung der Doktorwürde
der
Naturwissenschaftlich–Mathematischen
Gesamtfakultät
der
Ruprecht–Karls–Universität
Heidelberg

vorgelegt von
M. Tech. Srikanth Reddy Gopireddy
aus Nizambad, India

Tag der mündlichen Prüfung: 06.12.2013

Numerical Simulation of Bi-component Droplet Evaporation and Dispersion in Spray and Spray Drying

Gutachter: Prof. Dr. Eva Gutheil
PD Dr. N. Dahmen

Dreams can never become a reality without hard work

– Swamy Vivekananda

Abstract

Spray drying is one of the most widely used drying techniques to convert liquid feed into a dry powder. The modeling of spray flows and spray drying has been studied for many years now, to determine the characteristics of the end products, e.g. particle size, shape, density or porosity. So far, the simulation of polymer or sugar solution spray drying has not been studied because drying behavior as well as properties are unknown. Previous studies concentrated on the systems of milk, salt solution, colloids or other materials for which the thermal and physical properties are well tabulated.

The present study deals with the modeling and simulation of polyvinylpyrrolidone (PVP)/water and mannitol/water spray flows. PVP is a polymer, widely used as a pharmaceutical excipient, and mainly manufactured by BASF under several patented names, whereas mannitol is a sugar, which is used in dry powder inhalers and tablets. Experimental studies have shown that the powder properties of PVP and mannitol are significantly influenced by the drying conditions. The growing importance of PVP or mannitol powders and the inability of existing studies to predict the effect of drying conditions on the properties of the end product have prompted the development of a new reliable model and numerical techniques.

Evaporating sprays have a continuous phase (gas) and a dispersed phase, which consists of droplets of various sizes that may evaporate, coalesce, or breakup, as well as have their own inertia and size-conditioned dynamics. A modeling approach which is more commonly used is the Lagrangian description of the dispersed liquid phase. This approach gives detailed information on the micro-level, but inclusion of droplet coalescence and breakup increase computational complexity. Moreover, the Lagrangian description coupled with the Eulerian equations for the gas phase, assuming a point-source approximation of the spray, is computationally expensive. As an alternative to Lagrangian simulations, several Eulerian methods have been developed based on the Williams' spray equation. The Euler – Euler methods are computationally efficient and independent of liquid mass loading in describing dense turbulent spray flows.

The objective of this thesis is the modeling and simulation of spray flows and spray drying up to the onset of solid layer formation in an Euler – Euler framework. The behavior of droplet distribution under various drying conditions in bi-component evaporating spray flows is examined using, for the first time, direct quadrature method of moments (DQMOM) in two dimensions. In DQMOM, the droplet size and velocity distribution of the spray is modeled by approximating the number density function in terms of joint radius and velocity. Transport equations of DQMOM account for droplet evaporation, heating, drag, and droplet–droplet interactions.

At first, an evaporating water spray in nitrogen is modeled in one dimension (ax-

ial direction). Earlier studies in spray flows neglected evaporation or considered it through a simplified model, which is addressed by implementing an advanced droplet evaporation model of Abramzon and Sirignano, whereas droplet motion and droplet coalescence are estimated through appropriate sub-models. The assumption of evaporative flux to be zero or computing it with weight ratio constraints was found to be unphysical, which is improved by estimating it using the maximum entropy formulation. The gas phase is not yet fully coupled to the DQMOM but its inlet properties are taken to compute forces acting on droplets and evaporation. The simulation results are compared with quadrature method of moments (QMOM) and with experiment at various cross sections. DQMOM shows better results than QMOM, and remarkable agreement with experiment.

Next, water spray in air in two-dimensional, axisymmetric configuration is modeled by extending the one-dimensional DQMOM. The DQMOM results are compared with those of the discrete droplet model (DDM), which is an Euler – Lagrangian approach. Droplet coalescence is considered in DQMOM but neglected in DDM. The simulation results are validated with new experimental data. Overall, DQMOM shows a much better performance with respect to computational effort, even with the inclusion of droplet coalescence.

Before extending DQMOM to model PVP/water spray flows, a single droplet evaporation and drying model is developed, because most of the evaporation models available in the literature are valid for salts, colloids or milk powder. The negligence of solid layer formation effects on the droplet heating and evaporation is addressed, and treatment of the liquid mixture as the ideal solution is improved by including the non-ideality effect. The PVP or mannitol in water droplet evaporation and solid layer formation are simulated, and the results are compared with new experimental data, which shows that the present model effectively captures the first three stages of evaporation and drying of a bi-component droplet.

Finally, PVP/water spray flows in air are simulated using DQMOM including the developed bi-component evaporation model. Simulation results are compared with new experimental data at various cross sections and very good agreement is observed.

In conclusion, water and PVP/water evaporating spray flows, and preliminary stages of PVP/water and mannitol/water spray drying, i.e., until solid layer formation, are successfully modeled and simulated, and show good agreement with experiment.

Keywords: Sprays, PVP, Mannitol, DQMOM, Bi-component droplet

Zusammenfassung

Sprühtrocknung ist eines der am häufigsten eingesetzten Verfahren, um eine zugeführte Flüssigkeit in ein trockenes Pulver umzuwandeln. Die Modellierung von Sprühtrocknungsprozessen und des Sprays selbst wird seit vielen Jahren betrieben, um die Eigenschaften der Endprodukte, wie z.B. Partikelgröße, Form, Dichte oder Porosität, bestimmen zu können. Die Sprühtrocknung von Polymer- oder Zuckerlösungen wurde bisher noch nicht numerisch untersucht, da deren Trocknungsverhalten und Eigenschaften unbekannt sind. Bislang wurden nur Systeme mit Milch, Salzlösungen oder Kolloiden untersucht, deren thermische und physikalische Eigenschaften gut belegt sind.

Die vorliegende Arbeit widmet sich der Modellierung und Simulation von Polyvinylpyrrolidon (PVP)/Wasser und Mannitol/Wasser-Sprays. PVP ist ein Polymer, weit verbreitet als pharmazeutisches Bindemittel und von der BASF unter verschiedenen patentierten Namen hergestellt, während Mannitol, ein Zucker, hauptsächlich in Trockenpulverinhalatoren und Tabletten verwendet wird. Experimentelle Studien haben gezeigt, dass die Eigenschaften von PVP- und Mannitol-Pulvern von den Trocknungsbedingungen signifikant beeinflusst werden. Die zunehmende Bedeutung von PVP- und Mannitol-Pulvern und das Fehlen geeigneter Methoden zur Bestimmung des Einflusses der Trocknungsbedingungen auf die Eigenschaften der Endprodukte haben die Entwicklung eines neuen zuverlässigen Modells sowie numerischer Methoden angeregt.

Verdampfende Sprays bestehen aus einer kontinuierlichen Phase (Gas), und einer zerstäubten Phase, die aus Tropfen unterschiedlicher Größe besteht, die verdampfen, koaleszieren oder auch aufbrechen können, die aber auch ihre eigene Trägheit und größenabhängige Dynamik besitzen. Ein häufig verwendeter Modellierungsansatz ist die Beschreibung der zerstäubten, flüssigen Phase im Lagrangeschen Bezugssystem. Dieser Ansatz liefert detaillierte Informationen auf Mikroebene, aber Tropfen-Interaktionen wie Koaleszenz und Aufbrechen sind schwierig zu implementieren. Zudem ist der Lagrange-Ansatz, gekoppelt mit den Gleichungen der Gasphase im Eulerschen Bezugssystem unter Annahme der Punktquellen-Annäherung, zeitintensiv. Die Alternative zu Lagrange-Simulationen sind verschiedene Eulersche Methoden, die auf der Basis der Williams-Spraygleichung entwickelt wurden. Die Beschreibung von dichten turbulenten Sprayströmungen ist bei Verwendung dieser Euler – Euler Methoden zeiteffizient und unabhängig von der Massenladung der flüssigen Phase.

Die Zielsetzung der vorliegenden Arbeit ist die Modellierung und Simulation der Sprühtrocknung bis zum Beginn der Partikelbildung im Eulerschen Bezugssystem. Zur Untersuchung des Verhaltens der Tropfenverteilung unter verschiedenen Trocknungsbedingungen wurde erstmals die Methode *direct quadrature method of moments* (DQMOM) zur Betrachtung der verdampfenden Zweikomponentensprays eingesetzt. In der

DQMOM wird die Tropfengrößen- und Geschwindigkeitsverteilung des Sprays modelliert, indem die Zahlendichtefunktion angenähert wird. Die Transportgleichungen der DQMOM berücksichtigen Tropfenverdampfung, Aufheizung, Widerstand und Tropfen-Tropfen-Interaktionen.

Zuerst wird ein verdampfendes Wasserspray in Stickstoff in eindimensionaler Konfiguration, d.h. in axialer Richtung des Sprays, modelliert. Frühere Spraystudien vernachlässigten Verdampfungseffekte oder berücksichtigten diese durch ein vereinfachtes Modell. In dieser Arbeit wird die Tropfenverdampfung jedoch durch das Modell von Abramzon und Sirignano beschrieben, während Tropfenbewegung und -koaleszenz mit geeigneten Modellen abgeschätzt werden. Da die Vernachlässigung des Verdampfungsflusses oder seine Berechnung durch Einschränkungen des Gewichtsverhältnisses sich als unphysikalisch herausstellte, wurde der Fluss hier durch die Maximum-Entropie-Methode berechnet. Die Gasphase ist noch nicht vollständig an die DQMOM gekoppelt, stattdessen dienen die Gas-Einlaufbedingungen als Grundlage zur Berechnung der Kräfte, die auf Tropfen und Verdampfung wirken. Die Resultate der Simulationen werden mit der Quadratur-Momentenmethode (QMOM) und Experimenten an verschiedenen Querschnitten verglichen. Die DQMOM zeigt bessere Ergebnisse als die QMOM und auch erstaunliche Übereinstimmung mit dem Experiment.

Als nächstes wird das Wasserspray in umgebender Luft in zweidimensionaler, axialsymmetrischer Konfiguration durch Erweiterung der eindimensionalen DQMOM modelliert. Die DQMOM-Resultate werden mit denen des diskreten Tropfenmodells (DDM), ein Euler – Lagrange Ansatz, verglichen. Tropfenkoaleszenz wird in der DQMOM berücksichtigt, in der DDM aber vernachlässigt. Die Simulationsergebnisse werden durch aktuelle experimentelle Daten validiert. Insgesamt zeigt die DQMOM deutlich bessere Recheneffizienz, sogar unter Einschluss der Tropfenkoaleszenz.

Bevor die DQMOM auf PVP/Wasser-Sprays erweitert wird, wird ein Verdampfungs- und Trocknungsmodell für einen Einzeltropfen entwickelt, da die meisten der in der Literatur bekannten Verdampfungsmodelle auf Salze, Kolloide oder Milchpulver angewendet werden. Das Modell berücksichtigt die Partikelbildung in Zusammenhang mit der Tropfenaufheizung und -verdampfung, und die Behandlung der flüssigen Mischung als ideale Lösung wird durch Einschluss nicht-idealer Effekte verbessert. Die Ergebnisse der Simulation dieses Modells werden mit aktuellen experimentellen Daten verglichen, und es kann gezeigt werden, dass das entwickelte Modell die ersten drei Phasen der Verdampfung und des Trocknens eines Zweikomponententropfen effektiv erfassen kann.

Schließlich wird ein PVP/Wasser-Spray in umgebender Luft mittels DQMOM simuliert unter Anwendung des entwickelten Zweikomponentenverdampfungsmodells. Die Ergebnisse werden mit aktuellen experimentellen Daten an mehreren Querschnitten verglichen, und es konnte eine sehr gute Übereinstimmung festgestellt werden.

Letztendlich können verdampfende Wasser- und PVP/Wasser-Sprays und die Frühphasen der Sprühtrocknung von PVP/Wasser- und Mannitol/Wasser-Tropfen, d.h. bis zum Einsetzen der Bildung einer festen Schicht, erfolgreich modelliert und simuliert werden, unter guter Übereinstimmung mit dem Experiment.

Stichwörter: Sprays, PVP, Mannitol, DQMOM, Zweikomponententropfen

Contents

List of Tables

List of Figures

1. Introduction

Drying has found applications in many areas of industry such as chemical, food, pharmaceutical, polymer, ceramics and mineral processing. The basic idea of drying is to remove liquid by evaporation from the material that has either dissolved or suspended solids to a dried powder. The objectives can be, to reduce the transportation costs, to increase the shelf life of a material, which is done for instance in the preservation of milk, tomato, etc. or because the material has better properties in dry form than when dissolved.

Spray drying is one of the most widely used drying techniques and it is a process for converting a liquid feed into a powder by evaporating the solvent. The other drying techniques to produce powders mainly include freeze drying, supercritical drying and vacuum drying. Compared to other evaporation processes, spray drying has the great advantage that products can be dried without much loss of volatile or thermally unsteady or degradable compounds. These advantages are especially important in the production of pharmaceutical bulk materials such as polymers (e.g. polyvinylpyrrolidone), carbohydrates (e.g. mannitol) and food powders (e.g. milk and coffee powders) [1, 2]. Spray dryers are extensively used in industry, usually placed at the end-point of a process plant, which play an important role in the whole process, not because of their capital investment, size and operating costs but mainly because of their high energy efficiency and throughput production.

Spray drying can be structured into several steps primarily consisting of the atomization of liquid feed into a population of poly-disperse droplets followed by the convection of droplets and gas, the evaporation of the liquid solvent from the droplets, droplet-droplet collisions, which might lead to coalescence, aggregation and eventually breakup. In some cases, chemical reactions are also involved, e.g. in the production of polymer via monomer polymerization using spray drying. These sub-processes are inter-dependent. The atomization leads to droplets with specific size distribution and kinetic energy, thus influencing the droplets convection and probability of collision. The drying gas in most of the cases is the ambient air heated to a desired temperature with controlled relative humidity and this hot air is either co-flow or counter-flow depending on the system requirement and the thermal sensibility of the material. A schematic diagram of the typical spray drying process in shown in Fig. 1.1 [3]. A review of available spray drying designs, process types and applications is given by Masters [1].

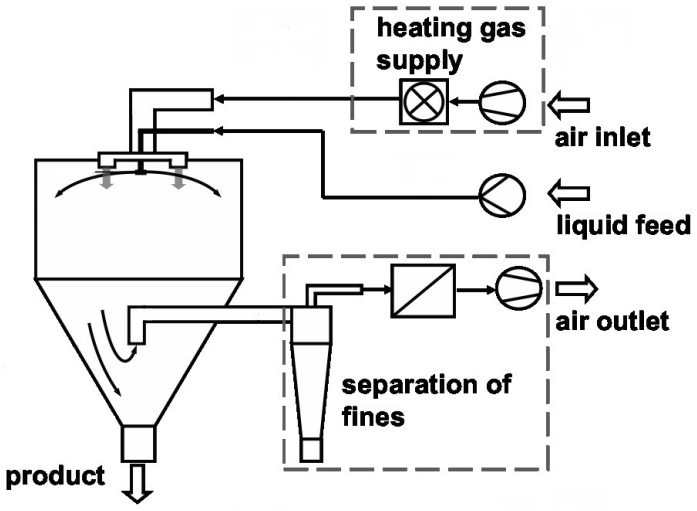

Fig. 1.1: A schematic diagram of the spray drying process [3].

Spray drying is a complex process and it is very difficult to predict the quality, properties and characteristics of the product such as particle size, density, porosity, flowability, shape, compressibility, etc. for the given drying conditions. The industrial practice to design is always based on the field experience and know-how followed by experimentation in pilot plant trials, which can be very expensive in case of rare materials [1, 4]. Problems associated with scale-up and hydrodynamics of the driers have resulted in limited success. The progress in computational techniques and computing prowess has given the advantage to develop a robust model of heat and mass transfer based on the equations of fluid flow within the spray chamber, which can predict the whole spray drying process i.e., from the liquid feed stock entering into the dryer to the end product, thereby resulting in cost effective and economic spray drier designs [1, 5].

The modeling of spray flows and the spray drying has been studied for many years now, which is done to predict the characteristics of the spray drying end products, e.g. particle size, shape, density or porosity. The previous studies mainly concern the systems of whole milk, salt solution, colloids or other materials for which the physical and thermal properties are well tabulated. The simulation of polymer or sugar solution spray drying is not studied so far because of unknown drying behavior of these materials and unavailability of properties.

The present study deals with the modeling and simulation of polyvinylpyrrolidone (PVP)/water and mannitol/water spray flows, with an aim to predict the effect of drying conditions on the evolution of droplet properties. The synthesis, applications of PVP and mannitol, and the motivation to choose these systems are elaborated in the following paragraphs.

PVP is a water-soluble polymer made from the monomer N-vinylpyrrolidone [6, 7].

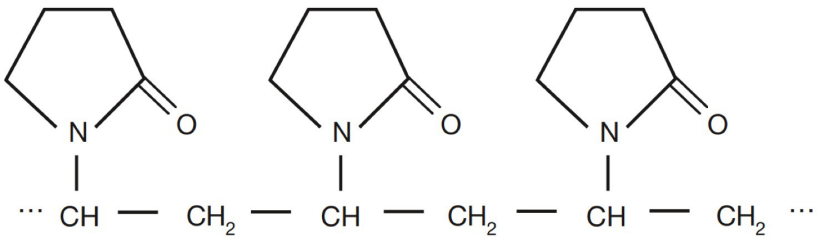

Fig. 1.2: Chemical structure of polyvinylpyrrolidone $(C_6H_9NO)_n$ [8].

It is a unique polymer providing a remarkable combination of properties that no other molecule is yet able to match. PVP offers a variety of properties, such as good initial tack, transparency, chemical and biological inertness, very low toxicity as well as high media compatibility and cross linkable flexibility. PVP was first synthesized by Prof. Walter Reppe and a patent was filed in 1939 for one of the most interesting derivatives of acetylene chemistry. Soluble PVP is obtained by free-radical polymerization of vinylpyrrolidone in water or 2-propanol, yielding the chain structure as shown in Fig. 1.2. There exists several grades of PVP, which are classified based on molecular weight, and spray drying technology is used in production of all types of PVPs [8].

PVP was initially used as a blood plasma substitute and later in a wide variety of applications in medicine, pharmacy, cosmetics and industrial production [9]. It is used as a binder in many pharmaceutical tablets; it simply passes through the body when taken orally. PVP binds to polar molecules exceptionally well, owing to its polarity. This has led to its application in coatings for photo-quality ink-jet papers and transparencies, as well as in inks for ink jet printers. PVP is also used in personal care products, such as shampoos and toothpastes, in paints, and adhesives that must be moistened, e.g. old-style postage stamps and envelopes [10]. It has also been used in contact lens solutions and in steel-quenching solutions. PVP is the basis of the early formulas for hair sprays and hair gels, and still continues to be a component of some [10]. As a food additive, PVP is a stabilizer and has E number E1201 [9]. In year 2006, the total world wide production of PVP was 31,000 tonnes, out of which 47% was used in cosmetics and 27% in pharmaceuticals [9]. Figure 1.3 [11] shows the scanning electron microscope (SEM) images of PVP powder produced via spray drying. In the evaporation and drying of PVP dissolved in water droplet, the molecular entanglement prior to solid layer formation is observed, which is different from the colloids, silica or salt in water droplet where crust formation is found. It is observed that the spray drying yields hollow or solid particles with spherical or non-spherical shape but the initial droplet size, gas temperature and velocity and other drying conditions show enormous effect on the final powder characteristics such as flowability, particle density,

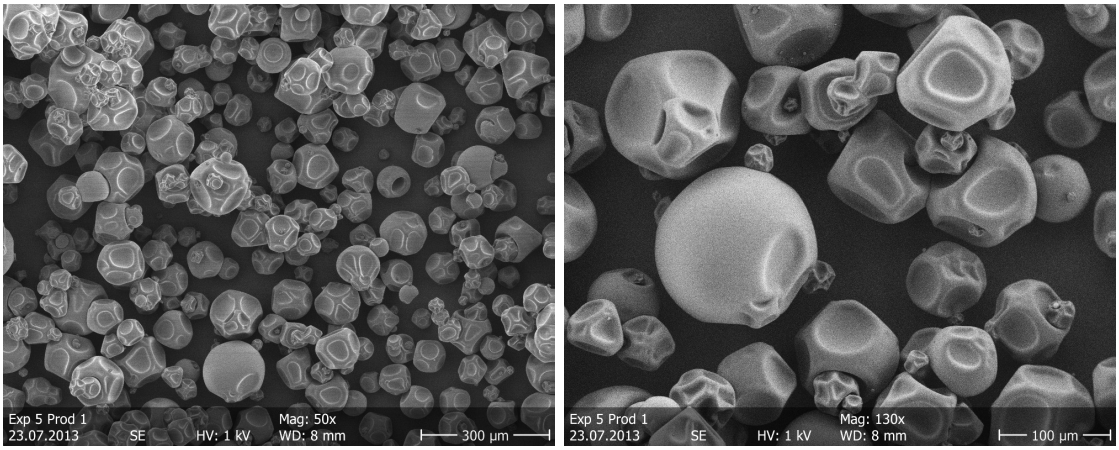

Fig. 1.3: SEM images of spray dried PVP [11].

porosity and shape [1]. To produce PVP powder with specific required properties is very important, for example, a uniform particle size distribution of PVP powder in pharmaceuticals not only helps in flowability of the powder but also improves the appealing of the final product.

Similar to PVP, mannitol has several useful applications. Mannitol is a sugar alcohol and it is widely used as a carrier particle in tablets. Mannitol is commonly produced via the hydrogenation of fructose, which is formed from either starch or sucrose (common table sugar) [13]. Although starch is a cheaper source than sucrose, the transformation of starch is much more complicated. Hydrogenation of starch yields a syrup containing about 42% fructose, 52% dextrose, and 6% maltose [13]. Sucrose is simply hydrolyzed into an invert sugar syrup, which contains about 50% fructose. In both cases, the syrups are chromatographically purified to contain 90–95% fructose [13]. The fructose is then hydrogenated over a nickel catalyst into mixture of isomers sorbitol and mannitol with a typical yield of 50% sorbitol and 50% mannitol [13]. The chemical structure of mannitol is shown in Fig. 1.4 [12].

For many years active pharmaceutical ingredients (APIs) are delivered to the lung

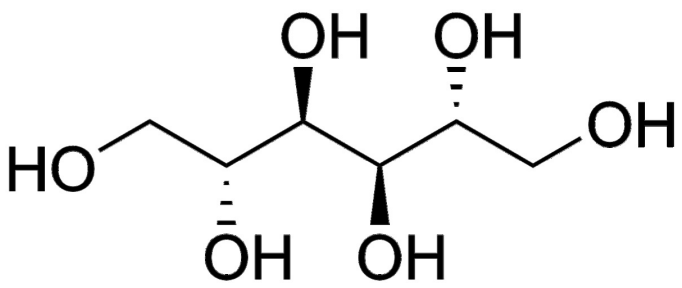

Fig. 1.4: Chemical structure of mannitol ($C_6H_8(OH)_6$) [12].

via inhalation aerosols. Dry powder inhalers (DPI) are commonly used to achieve aerosols of a micronized solid API. To guarantee a reliable and constant dosing, the flow properties of the formulation are of high interest. Since the micronized API with a particle size of 1 µm - 5 µm [14] exhibits poor flowability, carriers consisting of larger particles are added to the formulation in order to carry the API particles on their surface. Due to the sufficiently large size of the carrier particles, the adhesive mixtures exhibit adequate flowability. In addition to the flowability the surface structure of the carrier is crucial to the formulation performance [15] and has to be controlled during development. In the last decade, mannitol was identified as a possible carrier for DPIs [16] and efforts were made to tailor the surface structure [17–19]. Spray dried mannitol particles in general have a spherical shape and can consist of two major polymorphs [17, 20]. Similar to PVP, recent studies [21, 22] of mannitol spray drying reveal that process parameters like droplet size, gas temperature and relative humidity exhibit strong correlation with the final powder characteristics. Compared to PVP/water, evaporation and drying of mannitol/water droplet leads to crust formation on the droplet surface prior to complete dried particle.

The growing attention and wide applications of PVP and mannitol, as well as the effects of spray drying process on the final powder characteristics explains the particular interest towards these systems. The scarcity in thermal and physical properties of PVP and mannitol, and unknown behavior of evaporation and drying of PVP/water as well as mannitol/water droplets is a challenge for developing a mathematical model, numerical technique and validation. This project is part of the German Science Foundation (DFG) priority program "SPP1423", where spray flows and spray drying of PVP/water and mannitol/water are exclusively studied. This thesis deals with mathematical modeling and numerical simulation of both mono and bi-component (PVP/water and mannitol/water) droplet evaporation and dispersion in sprays and spray drying with an objective to numerically investigate the effect of drying conditions such as gas temperature, gas velocity, relative humidity, initial droplet size and velocity distribution on the evolution of droplet properties, which will enable in better understanding the spray flows thereby helps in designing the spray dryer.

The computational methods in the area of multiphase flow can primarily be categorized into two methods, (1) Lagrangian particle tracking method and (2) Euler – Euler or two continua/fluid methods. In both of these classical approaches, the continuous gas phase is modeled using the Navier – Stokes equations. Considering the presence of turbulence in the system, the Navier – Stokes equations can be solved on a fine computational mesh, which allows to capture all the macroscopic structures since all the considered length scales are considerably larger than the molecular length and time scales. Such a numerical resolution is defined as direct numerical simulation (DNS).

DNS solves all the characteristic scales of a turbulent flow and it requires no modeling of scales. DNS is implemented in a numerous flow problems for example particle dispersion [23, 24], turbulent reacting flows [25], spray flames [26], etc. A complete DNS of the spray drying is still not imaginary due to its high computational efforts [27, 28].

The alternative to DNS is the large eddy simulation (LES) [29–34] in which the large eddies are resolved and small eddies are modeled using a subgrid-scale model. This method requires spatial and temporal resolution of the scales in inertial subrange. The main disadvantage of LES method is that the accuracy of the flow field depends on the subgrid-model and filter size. Still, large computational time, and storage analysis of the huge data sets pose significant problems.

The attractive approach to solve Navier – Stokes equations is the Reynolds-averaged Navier – Stokes (RANS) numerical simulation [35–37], where the instantaneous Navier – Stokes equations are averaged with respect to time whereby an instantaneous quantity is decomposed into its time-averaged and fluctuating quantities. RANS equations together with the turbulence closure model can be solved to resolve the turbulent flow and compute the mean flow field quantities [35–37]. There are several RANS turbulence closure models, which are extensively discussed by Pope [37], and the most notable turbulence models include $k - \epsilon$ and extended $k - \epsilon$ model [37].

The other methods like volume of fluid (VOF) [38] and lattice-Boltzmann (LB) [39] approaches also exist in the multi-phase flows to model the flow around the droplets or particles, and therefore the fluid flow can be fully resolved. These methods may be characterized under the DNS method for multi-phase flow problems to define the interfaces.

In the Lagrangian particle tracking method, the droplets are injected into the gas and their trajectories are tracked by numerically evaluating the Lagrangian equations of motion. A typical spray consists of a large number of droplets and with limited computational resources, numerical parcels are implemented instead of droplets where each parcel contains of several number of droplets [35].

In Euler – Lagrangian approach, droplet–droplet interactions such as coalescence and breakup, which occur quite frequently in spray flows are difficult to account for due to computational complexity. The computational cost can be very expensive due to the large number of droplets needed to reach the statistical convergence, and computational cost is also dependent on mass loading of the dispersed phase.

In the two-continua method, also known as Euler – Euler approach, a set of conservation equations is written for each phase, and the sets are coupled through their respective source terms. This was first proposed by Elghobashi and Abou-Arab [40] with the aim to establish a two-phase turbulence model. They derived a two-equation model based on the principle of $k - \epsilon$ model, and the Reynolds-averaged conservation

equations are written in terms of volume fraction of each phase such that the sum of the volume fractions is unity. When the phases are equally distributed in the domain of interest with only moderate separation between the phases, the classical Euler – Euler approach is appropriate.

Euler – Euler methods offer significant advantages over the Euler – Lagrange approach, e.g. the two-continua method is independent of disperse phase mass loading, and also the coupling between dispersed and carrier phase does not require averaging over the parcels unlike in Euler – Lagrangian.

The merits of Euler – Euler methods play an important role when unsteady, turbulent gas-liquid flows with high dispersed phase mass loading are considered. Additionally, Euler – Euler methods can outperform the Euler – Lagrange in case of unsteady spray flows and the computational cost do not depend on the droplet mass loading. Most of the Euler – Euler methods in the field of spray flows are based on the description of dispersed phase as a number density function (NDF) and the evolution of this NDF due to physical processes of spray flows are described by the NDF transport equation, also known as population balance equation (PBE) [41]. This NDF transport equation is derived based on the kinetic equation [42] similar to the molecular kinetic theory, and it is known as general particle-dynamic equation in the field of aerosol science [43, 44].

There exists several Euler – Euler methods based on the kinetic equation such as Williams' spray equation and are categorized mainly as multi-fluid methods [45–47] and moment based methods [48–54]. In the multi-fluid approach, the distribution function is discretized using a finite volume technique that yields conservation equations for mass and momentum of droplets in fixed size intervals called sections or fluids [46]. This approach has recently been extended to higher order of accuracy [55], but discretization of droplet size space is still a problem that needs to be addressed. On the contrary, moment based methods such as quadrature method of moments (QMOM) [51, 52, 56–58] or direct quadrature method of moments (DQMOM) [53, 54, 59] do not pose this problem and they are found to be efficient and robust in the poly-disperse multiphase flow problems.

The scope of this work is modeling and simulation of mono and bi-component evaporating spray flows in an Euler – Euler framework. The focus is on the description of the characteristics of the spray flows and spray drying process, and the influence of the droplet size distribution on the droplet properties. In particular, spray inhomogeneity associated with the atomization process and its transport in the convective medium is not well understood. Subtle information is available about the particle formation and its influence on the properties of the resulting powder in spray drying.

The present study aims to develop a comprehensive spray model, which can be

used to simulate the bi-component droplet evaporation and dispersion in spray flows and spray drying, and to predict the evolution of the droplet properties. In order to understand the behavior of droplet distribution under various drying conditions, the droplet size and velocity distribution of the spray is modeled using DQMOM. Transport equations of DQMOM should account for droplet evaporation, heating, drag and droplet–droplet interactions, which are calculated through appropriate sub-models. The systems of interest for the current study include water spray in nitrogen in one physical dimension, water and polyvinylpyrrolidone (PVP)/water spray in air in two-dimensional, axisymmetric configuration. These systems were chosen for implementing and validating the numerical results. The experimental data for water spray in one-dimensional configuration was provided by Dr. R. Wengeler, BASF, Ludwigshafen, whereas Prof. G. Brenn, TU Graz, Austria, provided the data for the two-dimensional water and PVP/water spray flows. The system of PVP or mannitol dissolved in water is also considered to verify numerical results of the single bi-component droplet evaporation and solid layer formation.

Earlier studies based on DQMOM for spray flows either used simplified model for evaporation [60] or neglected the evaporation itself [61]. In the present study, the evaporation rate is computed using an advanced droplet evaporation model of Abramzon and Sirignano [62] for water spray, which accounts for variable liquid and film properties and includes the convective effects. For bi-component spray, the existing models to compute the evaporation rate neglect the non-ideality effect induced by non-evaporating component (e.g. PVP or mannitol) and ignore the solid layer resistance on the evaporation and droplet heating. In this study, for both PVP/water and mannitol/water droplet evaporation and solid layer formation, a mathematical model is formulated considering the non-ideality effect and solid layer resistance in the evaporation and heating. The evaporative flux, which is a point-wise quantity of the number density function of zero-droplet size, was either assumed to be zero [61, 63] or estimated with weight ratio constraints [60]. However, the later procedure was found to pose problems or to behave unphysical in multi-variate distributions [64, 65]. In the present study, evaporative flux is computed using the maximum entropy formulation [65–67].

The objectives of the current study are: modeling the evaporating water spray in nitrogen using DQMOM in one physical dimension and comparison of simulation results with QMOM and experiment, followed by extending the transport equations of DQMOM to two dimensions to simulate water spray in air, which is done for the first time, in axisymmetric configuration. The validation of DQMOM results with the discrete droplet (DDM) model [68], which is a well established Euler – Lagrangian technique, and with the new experimental data. In these configurations, the various physical processes due to gas–liquid and droplet–droplet interactions are accounted

for through appropriate sub-models. In order to simulate PVP/water spray flows, existing evaporation model needs modifications to include the effects of non-ideality and solid layer formation on droplet heating and evaporation, so the present work aims to develop a mathematical model, which can predict the bi-component single droplet evaporation and solid layer formation prior to drying with prerequisites to account for non-ideality of liquid mixture and effect of solid layer resistance on droplet heating and evaporation. Final objective is to extend DQMOM to simulate PVP/water spray flows using the developed bi-component evaporation model and subsequent verification of the simulation results with that of the new experimental data. Complete spray drying is not yet simulated, which requires coupling of gas phase with the DQMOM and accounting for droplet temperature in transport equations of DQMOM.

The dissertation is grouped into the following chapters. A review of the numerical simulation of sprays, governing equations of DDM and QMOM followed by the development of DQMOM and its transport equations are described in Chapter 2. The details of individual source terms of the spray flows such as bi-component droplet evaporation, droplet motion and droplet–droplet interactions and their equations are also elucidated in Chapter 2. In Chapter 3, numerical schemes to solve the single droplet evaporation and solid layer formation as well as DQMOM transport equations are explained along with the solution procedure of QMOM and Euler – Lagrangian approach DDM. A Wheeler algorithm to compute the initial data for DQMOM simulations and closure for QMOM unclosed moments is also given in Chapter 3. Chapter 4 presents the results and discussion starting from the water spray in nitrogen in one-dimension, followed by water spray in air in two-dimensional, axisymmetric configuration. The single droplet evaporation and solid layer formation model results are presented for both mannitol/water and PVP/water droplets. Finally, the results of PVP/water spray are presented. The conclusions and perspective future work are given in Chapter 5.

2. Mathematical Modeling

Spray constitutes of poly-disperse liquid droplets dispersed in gas medium. A typical sketch of a pressure-atomized spray breakup and its development is depicted in Fig. 2.1 [69, 70]. Here poly-disperse means that the properties of the disperse phase entities can be different for each entity. For example, evaporating sprays have a region near the nozzle where the liquid jet is not disperse, followed by a region after breakup of the primary jet that is composed of individual droplets having different properties such as size, velocity, temperature etc., which are defined as the poly-disperse droplets [41, 71]. To describe the poly-disperse characteristics of the spray flows, the mathematical modeling approach of Euler – Lagrangian and Euler – Euler framework is discussed, and the sub-models for the physical processes of sprays such as evaporation, forces, coalescence and breakup are elucidated in this chapter. Though the focus of this work is to model the spray flows using the direct quadrature method of moments (DQMOM), but the models like quadrature method of moments (QMOM) and discrete droplet model (DDM), which were used to compare and validate the DQMOM results, are also presented in this chapter.

2.1 State of the Art

The existing modeling approaches in the area of multiphase flows mainly include, (1) Lagrangian particle tracking method and (2) Euler – Euler or two continua/fluid meth-

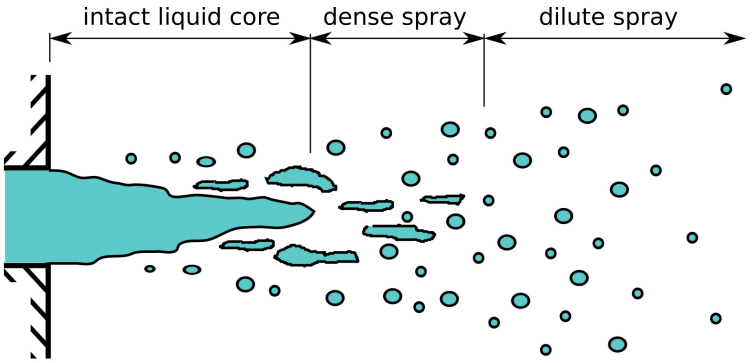

Fig. 2.1: Sketch of a pressure-atomized spray formation [69, 70].

ods. In the Lagrangian particle tracking method, the gas phase behavior is typically predicted by solving the unsteady Reynolds-averaged Navier – Stokes equations with an appropriate turbulence model and sub-models for various source terms [35, 37, 72]. In this method, droplets are injected into the gas and their trajectories are tracked by numerically evaluating the Lagrangian equations of motion.

A typical spray consists of a large number of droplets and with limited computational resources, numerical parcels are implemented instead of droplets where each parcel contains several number of droplets. The Euler–Lagrangian models are classified as locally homogeneous flow (LHF) method [73–75] and separated flow (SF) method [76–78].

The locally homogenous flow approximation of the LHF model for two-phase flow problems implies that the interphase transport rates are infinitely fast, so that both phases have same velocity and are in thermal equilibrium at each point of the flow [75]. This model neglects the slip effect between the liquid phase and gas phase. LHF approximation is the limiting case, which accurately represents spray with very small droplets [72].

Compared with the LHF model, the SF model has been used more widely in multiphase flow problems, because it provides the finite rate exchange of mass, momentum and energy between the phases [72]. The SF model assumes that each phase displays different properties and flows with different velocities, but the conservation equations are written only for the combined flow. In addition, the pressure across any given cross-section of a channel carrying a multiphase flow is assumed to be the same for both phases [72]. The SF models are further subdivided into discrete droplet model (DDM) [76–78], continuous droplet model (CDM) and continuous formulation model (CFM). The differences in these methods are explained by Faeth [72].

In DDM, the spray is divided into representative samples of discrete droplets whose motion and transport are tracked through the flow field, using a Lagrangian formulation. This procedure computes the liquid properties based on finite number of particles, called as parcels which are used to represent the entire spray [72, 76]. The gas phase is solved using Eulerian formulation, similar to the LHF method. The effect of droplets on the gas phase is considered by introducing appropriate source terms in the gas phase equations of motion. This type of formulation is is found to be convenient for considering a relatively complete representation of droplet transport processes [72].

The CDM was first introduced by Williams [79]. In this method, droplet properties are represented by a statistical distribution function defined in terms of droplet diameter, position, time, velocity, temperature, etc. [80]. Conservation principles yield a transport equation for the distribution function, which is solved along with the gas phase equations to deduce the properties of the spray [72, 79, 80]. Similar to DDM,

the governing equations for the gas phase include appropriate source terms to compute the effects of droplets.

The other important SF method for modeling sprays is the CFM, which employs a continuum formulation of the conservation equations for both phases [81, 82]. The motion of both droplets and gas are treated as interpenetrating continua. The work of Faeth [72] gives an extensive review of all the Euler – Lagrangian models.

The Euler – Lagrangian approach is so far considered to be effective in many applications, which gives detailed information at the micro-level, however it has significant drawbacks as listed by Archambault [67]. For instance, inclusion of droplet–droplet interactions such as coalescence and breakup, which occur quite frequently in spray flows, increases the computational complexity. The computational cost could be very expensive due to the large number of droplets needed to reach the statistical convergence, and it may pose difficulties and numerical instabilities in coupling of Lagrangian description of dispersed phase with the Eulerian equations of the gas phase. The computational cost is also dependent on mass loading of the dispersed phase. According to Archambault [67], the vertices of the droplet trajectory and numerical grid of the gas phase never coincide, hence a sub-grid model is required in order to compute the exchange rate between the phases [83]. Grid independent solutions are quite difficult to obtain [84], which could be because of an insufficient number of droplets in a grid cell leading to a significant error as can be observed in the regions of high droplet number density.

The study of Garcia *et al.* [85] and Riber *et al.* [86] describe and analyze the comparison of computational time between Euler – Euler and Euler – Lagrangian in homogeneous and non-homogeneous flows.

There is a tremendous amount of literature available on the Eulerian – Lagrangian approaches in spray flows and spray drying [76, 87–93], and references therein. As the focus of the current work is about Euler – Euler approach to spray flows, this section presents the review of available literature in this area.

A numerous Eulerian models have been recently developed where the disperse phase described based on a kinetic equation and continuum phase is resolved using Navier–Stokes equations. The basic idea in kinetic equation based Eulerian methods is that instead of solving the usual Euler equations for the dispersed phase, the evolution of the moment transform of the kinetic equation is solved, which resembles Navier – Stokes - like equation, and this equation is coupled to the continuum phase with the appropriate source terms. Such a kinetic equation is first derived by Williams [42], known as Williams' spray equation which is analogous to Boltzmann's equation of molecules [94, 95]. The derivation of Williams' spray equation is given by Archambault [67] and Ramakrishna [41]. This equation describes the temporal evolution of the probable

number of droplets within a range of droplet characteristics such as size, velocity, temperature and solute mole fraction within the droplet, which constitutes the phase-space at a spatial location. The solution of this equation coupled with the gas phase flow field equations provides the average properties of the spray, for example mean droplet diameter, Sauter mean droplet diameter, mean droplet velocity and many other statistical properties.

Among the existing Eulerian models, the multi-fluid method allows the detailed description of poly-disperse droplet size and velocity through correlations. Such an approach has been shown to be derived from the Williams' spray equation, Eq. (2.23), by Laurent and Massot [45] under the mono-kinetic spray assumption, which states that the velocity dispersion of the spray distribution function at a given time, spatial location and droplet size has to be zero. This assumption is important since it defines the validity limit of the multi-fluid model and also results in the "pressure-less gas dynamics" structure of the transport equations for conservation of mass and momentum of droplets [96]. These conservation equations are derived by discretizing the droplet distribution using a finite volume technique in fixed size intervals called sections or fluids.

This approach has been extended to higher order of accuracy [46], but discretization of droplet size phase-space is still a problem that needs to be addressed. The issues related to the mono-kinetic assumption have to be relaxed if the coalescence of droplets are to be considered, which is addressed by introducing a semi-kinetic equation and the results are presented for the evaporation and coalescence in spray flows [47, 97]. However, the validation in multi-dimensional configurations and the evaluation of the level of accuracy of such model versus the reference Lagrangian simulations as well as the related issue of a detailed study of the effective computational cost of the two approaches is not yet understood [98].

Next most notable method is the method of classes (CM) or discretized population balances (DPB) which is based on the discretization of droplet internal co-ordinates of the population balance equation [99–102] into a finite series of bins. The CM's compute the mean properties of the population such as droplets or particles within these bins by solving the discretized population balance equation. CM's are divided into two categories namely, (1) zero-order methods, and (2) higher order methods. In zero-order methods, the droplet size distribution (DSD) is considered to be constant in each class, and they are "extremely stable". Recently, Vanni [103] reviewed and compared the wide variety of zero-order CM's. In higher order methods, the DSD is defined in a specific functional form for every section of discretization, and these methods are usually more accurate but less robust [101–103]. The CM's present the main disadvantage of requiring a large number of classes to work with good accuracy,

and if the final application of the solution is implementation in a computational fluid dynamics (CFD) code, then the solution has to be done in every cell of computational domain, resulting in a very high computational time and memory problems.

On grounds of CM approach to solve the Williams' spray equation, Tambour [104] discretized the size axis of the droplet size distribution into sections which are also known as bins to derive sectional equations. The droplet evaporation, collision and other physical processes are handled using the source terms among these bins. However, this method is found to be first order accurate with respect to the droplet size [105], thus resulting in a strong numerical diffusion when few sections are used. The problem of finding an appropriate way to improve the accuracy of this method and also minimizing the number of sections becomes critical, especially when considering industrial codes, which are intended to perform complex three-dimensional simulations. Later this approach is extended to higher oder by Dufour and Villedieu [55], but still requirement of high number of sections needs to be addressed.

The other option is QMOM [51], which is based on the solution of moment transport equations of kinetic equation and the evaluation of unknown moments with the quadrature approximation. In this method, the distribution function is approximated with n-point Gaussian quadrature [51]. The moments are transported at every time and space step and the quadrature weights (number density), droplet radius, velocity and other phase-space variables, termed as abscissas, are computed using the product-difference (PD) algorithm of Gordon [106]. This method was first introduced by McGraw [51] in describing the aerosol dynamics to improve the method of moments (MOM) [107–113], and it is found to be a reliable method than MOM as the closure problem was observed with MOM [107, 114]. This method is proven to be promising in the problems of coagulation, aggregation and breakage [48–50], gas-particle flows [115]. One of the main limitations of QMOM is that since the dispersed phase is represented through the moments of the size distribution, the phase-average velocity of different phases must be used to solve the transport equations for the moments. Thus, in order to use this method in the context of sprays for which the inertia determines the dynamic behavior of the droplets, it is necessary to extend QMOM to handle cases where each droplet size is convected by its own velocity [53]. The efficiency and applicability of such methods [60, 116, 117] for moment inversion in multi-variate poly-disperse systems have remained a question of interest [115], which are characteristic in many technical applications. In the work of Marchisio and Fox [71], a comprehensive review of the existing moment methods is given.

Recently CQMOM was introduced by Yuan and Fox [118], to address the issues related to moment inversion. CQMOM is a novel moment-inversion algorithm, which works even for multi-variate moments. One apparent disadvantage of CQMOM (as

well as other multi-variate moment-inversion algorithms [115, 119]), according to Yuan and Fox [118], is the existence of multiple permutations (i.e., the order of conditioning). In the context of multi-dimensional quadrature, there are a number of interesting open questions concerning CQMOM. For example, in order to have a realizable quadrature, the abscissas found from the conditional moments must lie in support of the distribution function. For one-dimensional distribution functions with compact supports, it is shown that the abscissas will always lie realizable [118, 120]. However, it still needs to be found under which conditions boundedness will hold for the abscissas found from CQMOM for a two-dimensional (or higher) distribution function with compact support [118]. For certain applications (e.g. turbulent reacting flows), guaranteed boundedness is critical because the source terms are only defined on the support of the distribution function. As per revelations made by Yuan and Fox [118], the other open question is whether further improvements in the moment-inversion algorithm are possible to increase the number of optimal moments controlled, perhaps up to the maximum number of degrees of freedom determined by the number of quadrature nodes [118].

In order to overcome these problems, DQMOM has turned out to be an attractive alternative to QMOM, which was introduced by Fan *et al.* [121], later extended and validated by Marchisio and Fox [53]. This approach is found to be a powerful method in the multiphase flow problems to include all the physical processes of interest. The principal physical processes that the droplets encounter during the spray flows are (1) transport in real space or convection, (2) droplet evaporation and drying, (3) acceleration or deceleration of droplets due to forces induced by the surrounding gas, and (4) coalescence and collision of droplets leading to poly-dispersity. In DQMOM [53], the transport equations of weights and abscissas are solved directly rather than the moment equations, which is done in QMOM, thus avoiding the "moments" to "weights and abscissas" conversion through moment-inversion algorithm, so the word "direct" implies. DQMOM also allows each droplet to convect with its own velocity.

The DQMOM is proven to be a robust method in the field of multiphase flows and it is applied to various research problems other than spray flows after its development by Marchisio and Fox [53]. DQMOM is adapted and validated for the coagulation and sintering of particles by extending to bi-variate population balance equations [54]. Recently, DQMOM has been applied in studying exhaust particle formation and evolution in the wake of ground vehicle [122], and DQMOM is compared with classes method for simulations of bubbly flows [123]. In latest studies, DQMOM is employed in modeling poly-disperse fluidized powders [124], and modeling of turbulent combustion [125]. It is also used in combination with micro-mixing model and compared with stochastic field method for treating turbulent reactions [59].

In the field of spray flows, DQMOM in combination with multi-fluid method is

applied to study multi-component (fuel mixture) droplet evaporation [126]. Gumprich *et al.* [127, 128] analyzed the dense turbulent sprays using DQMOM, and DQMOM coupled with Eulerian multi-size moment model [129]. Madsen [61] extended DQMOM to include droplet coalescence in spray flows by neglecting the effects of evaporation, whereas Fox *et al.* [60] further improved DQMOM to model evaporating and coalescing spray flows but his study assumed simplified models for evaporation and coalescence. So far DQMOM has not been considered to treat the process of spray drying.

In the present study, DQMOM is used to describe the disperse phase consisting of poly-disperse liquid droplets, whereas the gas phase is not yet resolved but its inlet flow properties are taken for computing the droplet motion and evaporation. In this work, the DQMOM is implemented in two dimensions, which is done for the first time, and applied to study bi-component evaporating spray flows.

2.2 Euler – Lagrangian Approach

In the Euler – Lagrangian approach, the mean field equations are used only for the continuous gas phase. The droplet properties are defined along the path lines followed by the droplet. The trajectories of droplets are tracked for each droplet group by using a set of equations that describe their physical transport in flow field. In the current study, the discrete droplet model is used to define the droplet phase whereas the gas phase is modeled using the Navier – Stokes equations.

2.2.1 Gas Flow

The Euler – Lagrangian model DDM includes Euler equations for the gas phase with source terms for the dilute spray, which is described in Lagrangian coordinates. The instantaneous Navier – Stokes equations in an axisymmetric, two-dimensional configuration with no swirl for a dilute spray yield [68, 130]

$$\frac{\partial \rho}{\partial t} + \frac{\partial (\rho u_j)}{\partial x_j} = S_{l,1}, \tag{2.1}$$

$$\frac{\partial (\rho u_i)}{\partial t} + \frac{\partial (\rho u_i u_j)}{\partial x_j} = -\frac{\partial p}{\partial x_i} + \frac{\partial \tau_{ij}}{\partial x_j} + \rho g_i + S_{l,u_i}, \tag{2.2}$$

where ρ, u_i and p are the density, velocity component and pressure of the gas flow, respectively. g_i is the acceleration due to gravity and the quantities $S_{l,1}$ and S_{l,u_i} are the source terms due to spray evaporation [130, 131]. τ_{ij} is the viscous stress tensor given by

$$\tau_{ij} = \mu \left(\frac{\partial u_i}{\partial x_j} + \frac{\partial u_j}{\partial x_i} - \frac{2}{3} \frac{\partial u_k}{\partial x_k} \delta_{ij} \right), \tag{2.3}$$

where δ is the tensorial Kronecker delta given by

$$\delta_{ij} = \begin{cases} 1 & : \quad i = j \\ 0 & : \quad i \neq j. \end{cases} \tag{2.4}$$

Neglecting the processes of radiation, friction heating, Dufour effect, and the viscous heating, the conservation equation of total stagnant enthalpy can be written as

$$\frac{\partial(\rho h)}{\partial t} + \frac{\partial(\rho u_j h)}{\partial x_j} = \frac{\partial p}{\partial t} - \frac{\partial J^d_{q,j}}{\partial x_j} - \frac{\partial J^c_{q,j}}{\partial x_j} + S_{l,h}, \tag{2.5}$$

where h is the enthalpy of the gas flow and the terms on the right hand side (R.H.S) are the change rate of the pressure, the heat diffusion term, the heat conduction term and the source term due to spray evaporation, $S_{l,h}$, respectively. The heat conduction term is expressed by the Fourier's Law

$$J^c_{q,j} = -\lambda \frac{\partial T}{\partial x_j} = \frac{\lambda}{\bar{C}_p} \left(\frac{\partial h}{\partial x_j} - \sum_{\alpha=1}^{N_s} h_\alpha \frac{\partial Y_\alpha}{\partial x_j} \right), \tag{2.6}$$

where λ, T, $\bar{C}_p$ are thermal conductivity, gas temperature and specific heat capacity, respectively. N_s refers to the number of chemical species while h_α and Y_α are the enthalpy and mass fraction of species α. The heat diffusion term $J^d_{q,j}$ is written as

$$J^d_{q,j} = \sum_{\alpha=1}^{N_s} h_\alpha J^m_\alpha = -\sum_{\alpha=1}^{N_s} \rho h_{s,\alpha} D_{\alpha,M} \frac{Y_\alpha}{\partial x_j}, \tag{2.7}$$

where $h_{s,\alpha}$ and $D_{\alpha,M}$ are the specific sensible enthalpy of species α and diffusion coefficient of species α, respectively. Assuming a unity Lewis number, which is defined as the ratio of thermal diffusion to mass diffusion, (Le $= k/(\rho C_p D)$, and equal diffusibility of all species, the total heat flux is

$$J_q = J^c_{q,j} + J^d_{q,j} = -\frac{\lambda}{\bar{C}_p} \left(\frac{\partial h}{\partial x_j} - \sum_{\alpha=1}^{N_s} h_\alpha \frac{\partial Y_\alpha}{\partial x_j} \right) - \sum_{\alpha=1}^{N_s} \rho h_{s,\alpha} D_{\alpha,M} \frac{Y_\alpha}{\partial x_j}. \tag{2.8}$$

$$\frac{\partial(\rho h)}{\partial t} + \frac{\partial(\rho u_j h)}{\partial x_j} = \frac{\partial p}{\partial t} + \frac{\partial}{\partial x_j} \left(\Gamma_h \frac{\partial h}{\partial x_j} \right) + S_{l,h}. \tag{2.9}$$

The conservation equation of species mass can be written as

$$\frac{\partial(\rho Y_\alpha)}{\partial t} + \frac{\partial(\rho u_j Y_\alpha)}{\partial x_j} - \frac{\partial}{\partial x_j} \left(\rho D_\alpha \frac{\partial Y_\alpha}{\partial x_j} \right) = S_\alpha + \delta_{L,\alpha} S_{l,Y_\alpha}, \tag{2.10}$$

where D_α is the diffusion coefficient of species α while S_α and $S_{l,\alpha}$ are the source terms due to chemical reactions and spray evaporation, respectively. The mass fraction may be used to formulate mixture fraction. The advantage of an appropriately defined

mixture fraction is that the source term S_α will be zero. In the present work, for the water and polyvinylpyrrolidone (PVP)/water spray in air, the only possibility is to define the mixture fraction with reference to hydrogen as oxygen appears in both gas and liquid. A detailed study of different reference elements are given by Gutheil and Williams [132]. Thus the mass fraction Z_{A} of element A, where A is either N or H or O, is defined as

$$Z_{\mathrm{A}} = \sum_{i=1}^{n} \frac{a_{\mathrm{IA}} M_{\mathrm{A}}}{M_{\mathrm{I}}} Y_{\mathrm{I}}, \tag{2.11}$$

where a_{IA} is the mass of element A in molecule I and M_{A} and M_{I} are the molecular weights of element A and element I, respectively. Using this definition, mixture fraction can be defined as

$$\xi = \frac{Z_{\mathrm{A}} - Z_{\mathrm{A,min}}}{Z_{\mathrm{A,max}} - Z_{\mathrm{A,min}}}. \tag{2.12}$$

Multiplying Eq. (2.10) by $\frac{a_{\mathrm{IA}} M_{\mathrm{A}}}{a_{\mathrm{lA}} M_{\mathrm{I}}}$ and summing over total number of species under the assumption of equal diffusivity, the following conservation equation for mixture fraction is obtained

$$\frac{\partial(\rho\xi)}{\partial t} + \frac{\partial(\rho u_i \xi)}{\partial x_i} = \frac{\partial}{\partial x_i}\left(\Gamma_M \frac{\partial \xi}{\partial x_i}\right) + S_{l,\xi}, \tag{2.13}$$

where $\Gamma_M = \rho D_M$ is the mass diffusion coefficient of the mixture.

Equations (2.1), (2.2), (2.9) and (2.13) are the instantaneous conservation equations of mass, momentum, energy and mixture fraction. These equations need to be averaged for application to turbulent flows, and the general averaging types include time-averaging, ensemble-averaging and Favre- or density-weighted averaging [37]. For turbulent compressible flows, a density-weighted averaging i.e., Favre-averaging for Navier – Stokes equations is useful, and for more details about this approach, see [35, 72, 76, 77].

2.2.2 Discrete Droplet Model (DDM)

The discrete droplet model (DDM) is a well established Euler – Lagrange approach for dilute sprays [72, 133, 134]. The droplet positions and velocities are captured using Lagrangian particle tracking method, thereby the source terms for the Eulerian equations of the gas phase are computed. The model captures the trajectories and dynamics of individual droplets, which are assumed to be parcels [35, 72, 76, 77]. A parcel refers to a collection of droplets, which are described by a set of properties, i.e., $(\mathbf{x}_{p,k}, r_{p,k}, \mathbf{v}_{p,k}, m_{p,k}, T_{p,k}, \Delta V_{ij})$, where $\mathbf{x}_{p,k}$ is the position, $r_{p,k}$ is the radius, $\mathbf{v}_{p,k}$ is the velocity, $m_{p,k}$ is the liquid mass and $T_{p,k}$ is the temperature of k^{th} parcel in control volume ΔV_{ij}. By tracking the trajectories of a system of parcels, the model captures

the flow properties, i.e., droplet dynamics, evaporation and heating, and these are described through sub-models. These sub-models for the different physical processes of interest are given in Subsection 2.4.

The Lagrangian droplet equations are coupled to the gas phase through Eqs. (2.1) – (2.13), and the spray source terms are formulated using the particle-source-in-cell (PSIC) model [76, 130]. The system of gas and liquid phase equations is solved through a hybrid finite volume technique [130] with appropriate initial and boundary conditions. The DDM simulations were performed by Humza [68], so the details of initial and boundary conditions and numerical solution procedure of DDM are given in his work [68].

2.3 Euler – Euler Approach

In the Euler – Euler approach, the disperse phase is generally described by a number density function (NDF). In order to understand the proposed modeling approach of DQMOM one needs to be familiar with the definition of the NDF, the NDF transport equation, and its underlying terms, which are explained in the next subsections.

2.3.1 Treatment of the Spray

The disperse phase constitutes of discrete droplets and each of these droplets can be identified by a number of properties known as coordinates. In general, the coordinates are categorized as internal and external. The external coordinates are spatial coordinates. Internal coordinates refer to the properties of the droplets such as droplet velocity, mass, volume (or surface area, size), and enthalpy (or temperature). The NDF contains the information about the population of droplets inside a control volume [28, 41].

Let us consider a population of droplets in a spray dispersed in a control volume located at the physical point $\mathbf{x} = (x_1, x_2, x_3)$ where the size of the control volume is

$$\mathrm{d}\mathbf{x} = \mathrm{d}x_1 \mathrm{d}x_2 \mathrm{d}x_3. \tag{2.14}$$

Let $\xi = (\xi_1, \xi_2, ..., \xi_N)$ be the internal-coordinate vector. The NDF $n_\xi(\xi; \mathbf{x}, t)$ is defined as the probable number of droplets in the physical volume $\mathrm{d}\mathbf{x}$ and in phase-space volume $\mathrm{d}\xi$, given by $n_\xi \mathrm{d}\mathbf{x}\mathrm{d}\xi$.

The NDF is an average quantity of the dispersed phase, and it has mathematical characteristics of an averaged function, i.e., it is smooth and differentiable with respect to time t, physical space $\mathrm{d}\mathbf{x}$ and phase-space $\mathrm{d}\xi$. The number density of droplets contained in the phase-space volume $\mathrm{d}\xi$ per unit volume of physical space is $n_\xi \mathrm{d}\xi$. By integrating the NDF over all the possible internal-coordinates, different average

quantities of interest can be obtained. For instance, the total number density per unit physical volume $N(\mathbf{x}, t)$, which is defined as the total probable number of droplets in a unit physical volume, and it is also known as zeroth moment, $M_\xi(0)$, obtained as

$$N(\mathbf{x}, t) = M_\xi(0) = \int n_\xi(\xi; \mathbf{x}, t) \mathrm{d}\xi. \tag{2.15}$$

Similarly, the first moment defines the mean of the distribution, which is generally denoted by μ. The other moments which are common in probability and statistics are central moments [135], which are defined based on the distribution of droplets about the mean of the NDF. Thus the n^{th} moment is given as

$$M(n) = \int (\xi - \bar{\xi})^n \; n_\xi(\xi; \mathbf{x}, t) \mathrm{d}\xi, \tag{2.16}$$

where the second moment ($n = 2$) is known as variance, generally denoted by σ^2, and the third and fourth moments define the skewness and kurtosis of the distribution [135], respectively. Typical log-normal distribution with different values of mean, μ, and variance, σ^2, are shown in Fig. 2.2.

Likewise, when the NDF is defined with respect to more than one internal coordinate, the moments of NDF are known as multi-variate moments, which can be computed as

$$M_\xi(\mathbf{k}) = \int {\xi_1}^{k_1} {\xi_2}^{k_2} .... {\xi_N}^{k_N} n_\xi(\xi) \mathrm{d}\xi, \tag{2.17}$$

where $\mathbf{k} = (k_1, k_2, ...k_N)$ is a vector containing the order of the moments with respect to each component of ξ. In the description of spray flows, the NDF is in general described based on the droplet radius and velocities as the internal coordinates, ξ.

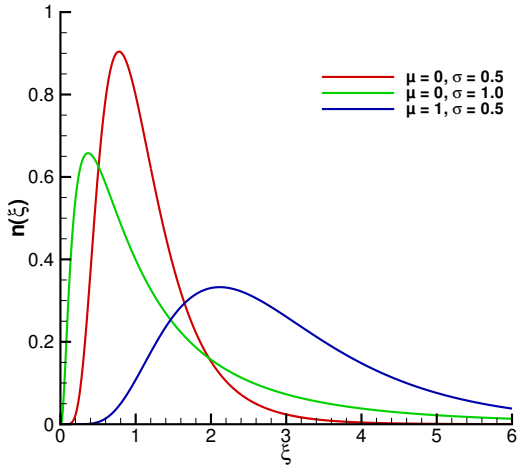

Fig. 2.2: A typical log-normal distribution with different values of μ and σ.

For the purpose of understanding the average properties of the spray dynamics from the simulations, the calculation procedure of mean droplet diameter and Sauter mean diameter is defined below. The considered NDF is defined based on the droplet diameter d. The mean droplet diameter, denoted as $d_{1,0}$ or d_{10}, can be computed from the droplet diameter based NDF $n_d(d)$as

$$d_{1,0} = \frac{1}{N}\int_0^\infty dn_d(d)\mathrm{d}d, \tag{2.18}$$

where N is the total number density given by

$$N = \int_0^\infty n_d(d)\mathrm{d}d. \tag{2.19}$$

Similarly, the Sauter mean diameter, $d_{3,2}$, or simply d_{32}, which is a very frequently used characteristic parameter especially in spray flows and spray drying, is given by

$$d_{3,2} = \frac{\int_0^\infty d^3 n_d(d)\mathrm{d}d}{\int_0^\infty d^2 n_d(d)\mathrm{d}d}. \tag{2.20}$$

Any other average droplet diameter can be extracted by simply dividing the $k+1^{\text{th}}$ moment with k^{th} moment, i.e.,

$$d_{k+1,k} = \frac{\int_0^\infty d^{k+1} n_d(d)\mathrm{d}d}{\int_0^\infty d^k n_d(d)\mathrm{d}d} = \frac{M_{k+1}}{M_k}. \tag{2.21}$$

Here, M_{k+1} and M_k are the moments of droplet diameter based NDF. The equation of averaged droplet diameter changes with the definition of NDF, i.e., averaged droplet diameter is different in diameter based NDF from that of volume based NDF, and the relation between volume based NDF and diameter based NDF is given by

$$n_V(V;\mathbf{x},t) = k_V d^3 n_d(d;\mathbf{x},t), \tag{2.22}$$

where k_V is the volume shape factor.

2.3.2 NDF Transport Equation

The evolution of the NDF due to physical processes is, in general, written in terms of a transport equation known as population balance equation. This transport equation is a simple continuity equation written in terms of the NDF, and it can be derived based on the balance for droplets/dispersed entities in a fixed subregion of internal coordinates and physical space [41]. This type of equation is known by different names in different fields. In aerosol dynamics, it is known as particle-dynamics equation, and in evaporating spray flows it is known as Williams-Boltzmann equation or simply,

Williams' spray equation, which was first introduced by Williams [42]. The derivation of such an equation is given by Archambault [67] and Ramakrishna [41].

In modeling the spray flows, the principal physical processes that must be accounted for are transport or convection, droplet evaporation, forces experienced by the droplets, and droplet–droplet interactions leading to poly-dispersity. Williams' spray equation either accounts for these physical processes or it can be easily extended to include, and it has proven to be a useful starting point for testing novel methods for describing poly-disperse dense liquid sprays. The Williams' spray equation [42], is given by

$$\frac{\partial f}{\partial t} + \frac{\partial (\mathbf{v} f)}{\partial \mathbf{x}} = -\frac{\partial \left(Rf\right)}{\partial r} - \frac{\partial (\mathbf{F} f)}{\partial \mathbf{v}} + Q_f + \Gamma_f. \tag{2.23}$$

Equation (2.23) describes the transport of the number density function $f(r, \mathbf{v}; \mathbf{x}, t)$ in terms of time, t, and Euclidean space, $\mathbf{x}$. In Eq. (2.23), first term at the left hand side (L.H.S) accounts for changes in the NDF with time and the second term includes the convective changes, $\mathbf{v}$ and $\mathbf{F}$ denote droplet velocity and total forces acting on the droplet per unit mass, respectively. The first term in the R.H.S includes the effect of evaporation, where R is the change in the droplet radius with time, i.e., $R = \mathrm{d}r/\mathrm{d}t$, and r is the droplet radius. The last two terms in Eq. (2.23) refer to the droplet–droplet interactions; Q_f represents the increase in f with time due to droplet formation or destruction by processes such as nucleation or breakup, and Γ_f denotes the rate of change in f due to droplet collisions.

The next subsections present the governing equations of the liquid phase defined through QMOM and DQMOM, which are used to solve Williams' spray equation.

2.3.3 Quadrature Method of Moments (QMOM)

Moment methods are an important class of approximate methods derived to solve kinetic equations, but require closure to truncate the moment set. In QMOM, closure is achieved by inverting a finite set of moments to reconstruct a point distribution from which all unclosed moments (e.g. spatial fluxes) can be related to the finite moment set [28, 51]. Figure 2.3 shows the typical quadrature approximation of the NDF in QMOM. The derivation of QMOM starts with the moment transformation of Williams' spray equation, which is done in the current study with multi-variate moments of droplet radius and velocity denoted by $M(k_1, k_2; \mathbf{x}, t)$ where k_1 and k_2 are the moment orders with respect to droplet radius and droplet velocity, respectively . The moment transformed Williams spray equation is given as [28],

$$\frac{\partial M(k_1, k_2)}{\partial t} + \frac{\partial M(k_1, k_2 + 1)}{\partial \mathbf{x}} = \int_{-\infty}^{\infty} \int_{0}^{\infty} r^{k_1} \mathbf{v}^{k_2} \left[-\frac{\partial \left(Rf\right)}{\partial r} - \frac{\partial (\mathbf{F} f)}{\partial \mathbf{v}} + Q_f + \Gamma_f \right] \mathrm{d}r \mathrm{d}\mathbf{v}. \tag{2.24}$$

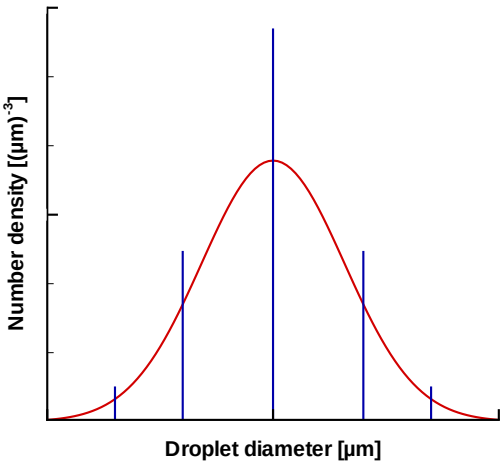

Fig. 2.3: Approximation of NDF in QMOM.

In the evolution of every moment $M(k_1, k_2)$ one higher order moment, i.e., $M(k_1, k_2+1)$ appears, see Eq. (2.24), which can be closed by using the product-difference algorithm (PD) [106]. The PD algorithm is quite efficient in a number of practical cases; however, it generally becomes less stable as the number of nodes, N, increases. It is difficult to predict *a priori* when this will occur, since it depends on the absolute values of the moments, but typically problems can be expected when $N > 10$ [71]. Another issue with PD algorithm is if the distributions with zero mean present, which can occur when the internal coordinate droplet velocity is ranging between positive and negative values, in this case the algorithm blows up due to the division by zero in the calculation of the coefficient matrix of the PD algorithm [71]. The alternative approach to the PD algorithm, which can handle cases with zero mean and remains stable even in the cases of $N > 10$, is the Wheeler algorithm proposed by Sack and Donovan [136]. The step by step procedure of implementing PD and Wheeler algorithms with corrections for moment realizability are given by Marchisio and Fox [71] with example calculations.

The substitution of different sub-models for the droplet evaporation, total force acting on droplets, droplet breakup and collision in the R.H.S of the Eq. (2.24) and with the help of PD or Wheeler algorithm for the unknown moment terms, yields a closed transported moment equation, which can then be solved to find the change in moments with time and spatial location. As discussed in the literature review, see Section 2.1, this method lacks the ability to handle multi-variate moments as the moment-inversion algorithm gets cumbersome. The different sub-models to describe the various physical processes of interest are described in Subsection 2.4. The numerical solution for the QMOM moment transport equations with initial and boundary conditions, and closure

of the unknown moments applying the Wheeler algorithm are explained in Chapter 3.

2.3.4 Direct Quadrature Method of Moments (DQMOM)

In DQMOM, the NDF is approximated as sum of the Dirac-delta functions. Substitution of this assumed NDF in Williams' spray equation yields transport equations in terms of the phase-space [60]. For the present study, a joint droplet radius-velocity number density function is considered, which is approximated in DQMOM as a sum of the product of weighted Dirac-delta functions [53] of radii and velocities [60],

$$f(r, \mathbf{v}) = \sum_{n=1}^{N} w_n \delta(r - r_n)\delta(\mathbf{v} - \mathbf{v}_n), \tag{2.25}$$

where w_n and r_n are chosen as N representative quantities of weights and radii, and $\mathbf{v}_n$ are the corresponding velocities. Such an approximation with a three-node ($N = 3$) closure can be depicted as shown in Fig. 2.4. Application of DQMOM to Williams' spray equation results in closed transport equations in terms of droplet weights or number densities, radii and velocities, which are written as

$$\frac{\partial w_n}{\partial t} + \frac{\partial (w_n \mathbf{v}_n)}{\partial \mathbf{x}} = a_n, \tag{2.26}$$

$$\frac{\partial (w_n \rho_\mathrm{l} r_n)}{\partial t} + \frac{\partial (w_n \rho_\mathrm{l} r_n \mathbf{v}_n)}{\partial \mathbf{x}} = \rho_\mathrm{l} b_n, \tag{2.27}$$

and

$$\frac{\partial (w_n \rho_\mathrm{l} r_n \mathbf{v}_n)}{\partial t} + \frac{\partial (w_n \rho_\mathrm{l} r_n \mathbf{v}_n \mathbf{v}_n)}{\partial \mathbf{x}} = \rho_\mathrm{l} \mathbf{c}_n, \tag{2.28}$$

where a_n, b_n and $\mathbf{c}_n$ are the source terms that account for droplet evaporation, forces on droplet (drag, buoyancy, lift, basset and virtual mass effect and gravity etc.), coalescence and breakup. These Eqs. (2.26) – (2.28) form a set of coupled hyperbolic partial differential equations, which can be solved simultaneously by using appropriate initial and boundary conditions to find $w_n(\mathbf{x}, t)$, $r_n(\mathbf{x}, t)$ and $\mathbf{v}_n(\mathbf{x}, t)$, and thereby the evolution of droplet distribution function f can be computed.

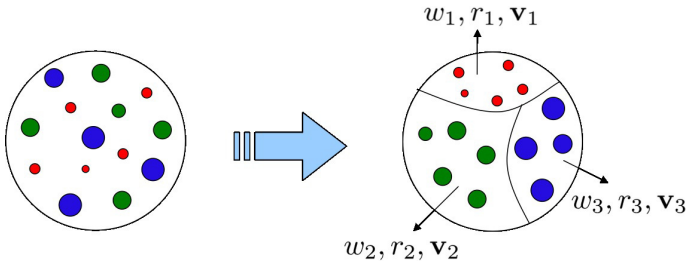

Fig. 2.4: NDF approximation in DQMOM.

The Eqs. (2.26) – (2.28) are closed by modeling the source terms, i.e., a_n, b_n and $\mathbf{c}_n$, using the physical models to account for effects of droplet evaporation, forces on droplet, coalescence and breakup. These source terms are calculated through the moment transformation of phase-space terms, which yields the following linear system

$$P_{k,\mathbf{l}} = \int r^k \mathbf{v}^l \left[-\frac{\partial(Rf)}{\partial r} - \frac{\partial(\mathbf{F}f)}{\partial \mathbf{v}} + \Gamma_f + Q_f \right] \mathrm{d}r\mathrm{d}\mathbf{v}. \tag{2.29}$$

The exact form of the DQMOM linear system relies on the choice of moments, and it can be generated from

$$\begin{aligned} \int r^k \mathbf{v}^l \left[\frac{\partial f}{\partial t} + \frac{\partial(\mathbf{v}f)}{\partial \mathbf{x}} \right] \mathrm{d}r\mathrm{d}\mathbf{v} &= \sum_{n=1}^{N} (1-k) r_n^k v_{1,n}^{l_1} v_{2,n}^{l_2} v_{3,n}^{l_3} a_n \\ &+ \sum_{n=1}^{N} (k - l_1 - l_2 - l_3) r_n^{k-1} v_{1,n}^{l_1} v_{2,n}^{l_2} v_{3,n}^{l_3} b_n \\ &+ \sum_{n=1}^{N} r_n^k v_{1,n}^{l_1} v_{2,n}^{l_2} v_{3,n}^{l_3} (l_1 v_{1,n}^{-1} c_{1,n} + l_2 v_{2,n}^{-1} c_{2,n} + l_3 v_{3,n}^{-1} c_{3,n}) \\ &+ \delta_{k0} u_1^{l_1} u_2^{l_3} u_3^{l_3} \psi, \end{aligned} \tag{2.30}$$

where ψ is the evaporative flux, and u_1, u_2, and u_3 are three components of the gas velocity. The complete linear system is formed by combining Eqs. (2.29) and (2.30), which consists of $5N+1$ unknowns, a_n, b_n, $\mathbf{c}_n$ and ψ. To obtain a solution for this linear system, the moments are chosen in a way that the resulting coefficient matrix is non-singular. Previous validation studies of DQMOM, and comparison of its performance with QMOM have demonstrated that by using two-node closure ($N = 2$) approximation for f is sufficient to track the lower order moments with small errors [48, 49, 54]. Increasing the number of nodes, N, to three ($N = 3$) have improved the results, and in general the evaporation and coalescence terms can be accurately approximated with $N = 2$–4 [48, 49, 54, 60]. In the present work, a three-node closure is used, i.e., N is set to be 3, and the corresponding moment set is chosen as [60, 137] $k \in \{1, ..., 2N\}$; $l \in \{0, 1\}$, where l is composed of three components l_1, l_2, and l_3. The chosen set of k and l values conserves the mass and momentum of droplets, and these values are found to give non-singular source terms matrix [60]. Along with these moments set, the calculation of the source terms from the linear system requires the mathematical formulation for the evaporation, forces on droplet and droplet–droplet interactions, which enter as sub-models and these sub-models. The sub-models are individually discussed and mathematical formulation is given in Subsection 2.4.

The evaporation term in Eq. (2.29) can be simplified by evaluating the integral on the R.H.S, which is given as

$$-\int r^k \mathbf{v}^l \frac{\partial(Rf)}{\partial r} = -(r^k \mathbf{v}^l Rf)|_{r=0}^{r=\infty} + k \int_0^{\infty} r^{k-1} \mathbf{v}^l \frac{\partial\,(Rf)}{\partial r} \mathrm{d}r. \tag{2.31}$$

With the assumption that the maximum droplet size is a finite value, the above equation can be further simplified as

$$-\int r^k \mathbf{v}^l \frac{\partial(Rf)}{\partial r} = \delta_{k0}\psi\mathbf{v}^l + k\int_0^\infty r^{k-1}\mathbf{v}^l \frac{\partial\,(Rf)}{\partial r}\mathrm{d}r, \tag{2.32}$$

where δ_{k0} is the Kronecker delta, which is defined as $\delta_{k0} = 1$ if $k = 0$ and $\delta_{k0} = 0$ for any other k value. The quantity $\psi = Rf(0)$ is the evaporative flux, which is a point wise quantity of the NDF representing the number of droplets having zero size. This quantity in DQMOM is computed by weight ratio constraints, which are introduced by Fox *et al.* [60] where ψ is treated as an additional variable along with a_n, b_n and c_n's.

These ratio constraints of weights, radii and velocities [60] are given by

$$\frac{\mathrm{D}}{\mathrm{D}t}\left(\frac{w_n}{w_{n+1}}\right) = 0; \quad \frac{\mathrm{D}}{\mathrm{D}t}\left(\frac{r_n}{r_{n+1}}\right) = 0; \tag{2.33}$$

$$\frac{\mathrm{D}}{\mathrm{D}t}\left(\frac{v_{j,n}}{v_{j,n+1}}\right) = 0, \tag{2.34}$$

where j is the index for three velocity components. Fox *et al.* [60] show that the estimation of evaporative flux via weight ratio constraints is found to give acceptable results in a stationary one-dimensional configuration. However, Fox *et al.* [60] suggests that this calculation procedure is found to pose problems in the case of complicated distribution functions [64].

In the current study, this is addressed by implementing the maximum entropy (ME) principle proposed by Mead and Papanicolaou [66] for water and PVP/water spray flow in air, which estimates the evaporative flux through reconstruction of the droplet distribution using its moments.

The principle of maximum entropy in the problem of moments is that the distributions that satisfy the given moment set (also called as constraints), the most likely or least biased probability density function is the the one whose statistical entropy is a maximum. This formulation allows the determination of a number density function from the limited amount of information such as few known moments of a distribution [66]. The implementation of this method to compute ψ is explained by Massot *et al.* [98].

The ME method is first introduced by Mead and Papanicolaou [66] to compute a distribution for the given moment set based on the maximization of the following Shannon entropy from the information theory [66],

$$\mathcal{H}[f] \equiv -\int_{r_{\min}}^{r_{\max}} f(x)\ln f(x)\mathrm{d}x. \tag{2.35}$$

Mead and Papanicolaou have proven that there exists ME distribution satisfying the above entropy principle [66] for the case when the vector of moments M belongs to

the interior of the moment space $M = \{M(0), M(1), ..M(N)\}$. This is a standard constrained optimization problem where the constraints are to satisfy the given moments. In the ME method, following the moments satisfaction condition, below equation is the explicit representation of the ME approximation,

$$f_M^{ME}(x) \equiv \exp\left(-\Sigma_{j=0}^{N}\, \xi_j x^j\right), \tag{2.36}$$

where the coefficients $\xi_0, \xi_1 ... \xi_N$ are the Lagrange multipliers, and N is the number of moments. These coefficients are computed based on the condition of minimizing the following convex potential:

$$\Delta \equiv \int_{r_{\min}}^{r_{\max}} \left[\exp\left(-\Sigma_{j=0}^{N}\, \xi_j x^j\right) - 1\right] \mathrm{d}x + \Sigma_{j=0}^{N}\, \xi_j M(j). \tag{2.37}$$

The stationary points of Eq. (2.37) are given by $\frac{\partial \Delta}{\partial \xi_i} \equiv 0$, which yields the following equation

$$\int_{r_{\min}}^{r_{\max}} x^i \exp\left(-\Sigma_{j=0}^{N}\, \xi_j x^j\right) \mathrm{d}x \equiv M(i). \tag{2.38}$$

The solution of the above equation gives ξ_i, and substitution of these ξ_i in Eq. (2.36) yields the required NDF. The above equation can be solved numerically using a Newton method, with the initial guess as $\xi \equiv (-\ln M(0)/(r_{\min} - r_{\max})), 0, ...0)$, and updated ξ's are estimated by

$$\xi^{+} \equiv \xi - H^{-1}(M - \langle X \rangle_{\xi}). \tag{2.39}$$

Here H is the Hessian matrix defined by $H_{i,j} \equiv \frac{\partial \Delta}{\partial \xi_i \partial \xi_j} \equiv \langle x^{i+j} \rangle$ for i, $j \equiv 0, 1, ...N$, and $\langle X \rangle_{\xi} \equiv (\langle x^0 \rangle_{\xi}, ... \langle x^N \rangle_{\xi})$ is the vector of approximated moments, which are expressed as

$$\left\langle x^k \right\rangle_{\xi} \equiv \int_{r_{\min}}^{r_{\max}} x^i \exp\left(-\Sigma_{j=0}^{N}\, \xi_j x^j\right) \mathrm{d}x. \tag{2.40}$$

The numerical procedure to implement this approach is same as done by Mead and Papanicolaou [66] and Massot *et al.* [98], where a double-precision 24-point Gaussian quadrature method very efficiently produces the required accuracy for $\left\langle x^k \right\rangle_{\xi}$. More details about the derivation of this method and numerical solution procedure are given by Mead and Papanicolaou [66].

As the systems of interest in the present study are water spray in quiescent air or nitrogen as well as PVP/water spray in quiescent air, currently the gas phase is not fully coupled with DQMOM transport equations but its inlet properties taken from the experiment are used to compute the droplet motion and evaporation.

2.4 Single Droplet Modeling

This section presents the physical processes due to gas–liquid and droplet–droplet interactions, namely, droplet heating and evaporation, forces acting on the droplet, droplet

collisions and breakup, which enter as source terms in QMOM, DQMOM and DDM.

2.4.1 Droplet Heating and Evaporation

In spray flows, particularly in spray drying processes, the droplet evaporation can be critical because (1) it has direct effect on drying rate of droplets yielding powder, and (2) it influences the final powder characteristics. The evaporation process can be very complex under realistic spray drying conditions. Factors that increase the complexity of the evaporation models are (1) the multi-component character of the liquid solution, (2) the interaction between droplets in the turbulent gas environment, and (3) large differences in volatility of solutes. The study of single droplet heating and evaporation forms a basis for simulating complex spray flows. As stated before, few studies have been carried out for application of DQMOM on evaporating sprays [60, 126, 138]. However, these studies consider a simplified evaporation model to calculate the change in droplet size with time, i.e., either as a linear function of droplet volume or non-linear function of droplet volume, which is similar to the well established d^2 law. In the present study, an advanced droplet evaporation model of Abramzon and Sirignano [62] is used for the single component droplet evaporation, whereas, for the bi-component PVP/water droplet, the focus is to develop a mathematical model, which can predict the evaporation and drying of a single bi-component droplet, thereby include the developed model to study the PVP/water and mannitol/water droplet evaporation and solid layer formation. The following subsections present the mathematical models for mono- and bi-component droplet evaporation.

2.4.1.1 Single Component Droplet

The droplet evaporation is a complex process where simultaneous heat and mass transfer occurs leading to regressing droplet size. Fluid dynamics plays a major role when there is a relative motion between the droplets and the surrounding gas. The flow properties have a critical impact on the mass, momentum and energy exchanges between the gas and the droplets. Droplet evaporation was first studied by Langmuir [139] in 1918. Earlier studies reported that the droplet surface decreases constantly with time [140], famously known as d^2 law. After Langmuir [139], several studies were carried out in this area. Most notable works in droplet evaporation descriptions include the studies of Chigier [141], Clift *et al.* [142], Glassman [143], Lefebvre [144], and Williams [145]. A review of existing droplet evaporation models is given by Faeth [72], Law [146] and Sirignano [140].

The study of Abramzon and Sirignano [62] introduced a model for single component droplet evaporation, which includes the convection effects, droplet heating, and variable

liquid and film properties.

The work of Sirignano [140] classified the single component droplet evaporation models into six types, and they are given in the order of complexity as, (1) constant droplet temperature model (also known as the d^2 law), (2) infinite liquid conductivity model (uniform but time dependent droplet temperature), (3) conduction limit (spherically symmetric transient droplet heating) model, (4) effective conductivity model, (5) vortex model of droplet heating, and (6) Navier – Stokes solution. There are various differences among these models, and some of these models are shown to be limits of another model [140].

Recent study of Sazhin [147] gives an overview of all the existing droplet evaporation models, particularly in the field of combustion studies.

For evaporating water spray flow in air, the spatial gradients of the temperature within the droplet will not be significant when the evaporation conditions are room temperature and atmospheric pressure. Thus, in the current study, uniform but time dependent droplet temperature with convective effects can be used to predict the evaporation rate, and the droplet size regression. Therefore, for evaporating water sprays under room temperature and pressure conditions, the model of Abramzon and Sirignano [62] is implemented, which is a uniform temperature model that includes the convective effects, and considers the variable liquid and film properties. Here film means a thin layer across the droplet surface where the saturation of liquid vapor exists, and this vapor mass fraction is computed based on the vapor-liquid equilibrium.

The rate of change of droplet mass with time due to convective evaporation and droplet heating in water spray is computed as [62]

$$\dot{m} = 2\pi R \rho_{\mathrm{f}} D_{\mathrm{f}} \widetilde{\mathrm{Sh}} \ln(1 + B_M), \tag{2.41}$$

where R is the droplet radius, ρ_{f} is the density in the film, D_{f} is the water diffusivity in the film, $\widetilde{\mathrm{Sh}}$ is the modified Sherwood number that accounts for the convective effects of droplet evaporation [62], given as

$$\widetilde{\mathrm{Sh}} = 2 + \frac{\mathrm{Sh} - 2}{B_M} (1 + B_M) \ln(1 + B_M). \tag{2.42}$$

Here, Sh is the Sherwood number, which is defined as the ratio of convective mass transfer to the diffusion mass transport, and it is generally written in terms of the droplet Reynolds number, $\mathrm{Re_d}$, and Schmidt number, Sc, given by [62]

$$\mathrm{Sh} = 1 + (1 + \mathrm{Re_d\ Sc})^{1/3} f(\mathrm{Re_d}). \tag{2.43}$$

The droplet Reynolds number is defined as the ratio of inertial forces to viscous forces, which is written as $\mathrm{Re_d} = 2r\rho_{\mathrm{g}}|\mathbf{u} - \mathbf{v}|/\mu_{\mathrm{f}}$. The Schmidt number is used to characterize

the fluid flows in which there is simultaneous momentum and mass diffusion, and it is defined as the ratio between momentum diffusion and mass diffusion, written as $\mathrm{Sc} = \mu_\mathrm{f}/(\rho_\mathrm{g} D_\mathrm{f})$. In Eq. (2.43), the function $f(\mathrm{Re_d})$ depends upon the droplet Reynolds number, and in case of low Reynolds number, it may be calculated as defined by Abramzon and Sirignano [62], with $f(\mathrm{Re_d}) = 1$ for $\mathrm{Re_d} \leq 1$ and $f(\mathrm{Re_d}) = \mathrm{Re_d}^{0.077}$ for $\mathrm{Re_d} \leq 400$.

In Eq. (2.41), B_M is the Spalding mass transfer number, expressed in terms of the mass fraction of vaporized liquid as,

$$B_M = \frac{Y_\mathrm{s} - Y_\infty}{1 - Y_\mathrm{s}}. \tag{2.44}$$

Here Y_s and Y_∞ are mass fractions of the water at the droplet surface and in the bulk of surrounding gas, respectively. Y_s is computed from the vapor-liquid equilibrium through the vapor pressure of water, which is written as [148]

$$Y_\mathrm{s} = \frac{M_\mathrm{w}}{M_\mathrm{w} + \bar{M}(\bar{p}/p_\mathrm{w} - 1)}. \tag{2.45}$$

The quantities M_w and p_w denote molar mass and vapor pressure of water while $\bar{M}$ and $\bar{p}$ represent molar mass and mean pressure of the surrounding gas, respectively.

Although the initial temperatures of gas and the droplet are equal and are at room temperature, the droplet temperature is subject to change due to evaporation. Time evolution of droplet temperature for water spray is computed using the uniform temperature model [62],

$$m C_{p\mathrm{L}} \frac{\mathrm{d}T_\mathrm{s}}{\mathrm{d}t} = Q_\mathrm{L} = \dot{m} \left[\frac{C_{p\mathrm{Lf}}(T_\infty - T_\mathrm{s})}{B_T} - L_V(T_\mathrm{s}) \right], \tag{2.46}$$

where m is the droplet mass, Q_L is the net heat transferred to the droplet per unit time, $C_{p\mathrm{L}}$ and $C_{p\mathrm{Lf}}$ are the specific heat capacity of the liquid and in film, respectively, T_s is the temperature at droplet surface, T_∞ is the temperature of the surrounding gas, and $L_V(T_\mathrm{s})$ is the temperature dependent latent heat of vaporization at T_s. B_T is the Spalding heat transfer number, which is calculated in terms of the mass transfer number using the relation [62]

$$B_T = (1 + B_M)^\phi - 1, \tag{2.47}$$

where the exponent ϕ is given by [62]

$$\phi = \frac{C_{p\mathrm{L}}}{C_{pg}} \frac{\widetilde{\mathrm{Sh}}}{\widetilde{\mathrm{Nu}}} \frac{1}{\mathrm{Le}}. \tag{2.48}$$

Here C_{pg} is the specific heat capacity of the gas, Le is the Lewis number, and $\widetilde{\mathrm{Nu}}$ is the modified Nusselt number, which accounts for convective droplet heating, and it is

given by [62]

$$\widetilde{\mathrm{Nu}} = 2 + \frac{\mathrm{Nu}}{(1 + B_T)^{-0.7}}. \tag{2.49}$$

The Nusselt number, Nu, defined as the ratio between convective heat transfer to conductive heat transfer and it is usually expressed in terms of the droplet Reynolds number, $\mathrm{Re_d}$, and Prandtl number, Pr, as

$$\mathrm{Nu} = 1 + (1 + \mathrm{Re_d\ Pr})^{1/3} f(\mathrm{Re_d}). \tag{2.50}$$

The Prandtl number, Pr, is defined as the ratio of momentum diffusion rate to the thermal diffusion rate, written as, $\mathrm{Pr} = C_{p\mathrm{Lf}}\mu_\mathrm{f}/k_\mathrm{f}$.

2.4.1.2 Bi-component Droplet

Many studies present the evaporation phenomena associated with pure and multi-component droplet, but there is a lack of a mathematical model, which can predict the evaporation and drying behavior of a droplet containing a polymer or sugar dissolved in water because of the unknown physical behavior, unavailability of experimental results and complexity of the problem. The available literature in the area of single bi-component droplet evaporation and drying is reviewed in the following paragraphs followed by the development of new mathematical model to compute the evaporation and solid layer formation of a bi-component droplet.

Charlesworth and Marshall [149] first investigated the process of single droplet evaporation and drying by measuring the change in droplet mass using the deflection of a thin, long glass filament. This study [149] also classifies different stages of droplet evaporation. Later, this experiment with some modifications is considered in many studies. The work of Sano and Keey [150] includes the drying behavior of colloidal material into a hollow sphere by considering the migration of solid matter towards the center of the droplet through the convection measurement inside the droplet, which is a challenge to experiment [151].

Most of the experiments concerning the droplet evaporation and drying available in literature are either related to salts [149, 152–154], milk powders [155, 156] or some other colloidal matter [150, 151, 157–159], but none deals with droplets of polymer or mannitol as a constituent. Previously developed models assume a uniform temperature gradient within the droplet [151, 152, 157], and neglect the effect of solid formation [152, 156, 157]. The study of Nesic and Vodnik [151] presents the kinetics of droplet evaporation to predict the drying characteristics of a colloidal silica droplet, where the crust formation on the surface occurring in this configuration is considered. The surface vapor concentration of the evaporating solvent is calculated using experimental material dependent factors, which are not available for every solution including

polymer and mannitol solutions in water. Moreover, in case of a polymer, molecular entanglement leads to solid layer formation. Nesic and Vodnik [151] use a more detailed description of various stages of droplet evaporation and drying. These stages, as described by Nesic and Vodnik [151], are that the droplet temperature initially rises to an equilibrium value and solvent evaporates continuously, which in turn increases the solute mass fraction within the droplet. When the solute mass fraction at the droplet surface rises to a critical value, then there starts a thin solid layer formation, and further drying leads to a dried particle.

Farid [156] shows that the droplet evaporation and drying are controlled by thermal-diffusion rather than mass-diffusion as assumed by most of the earlier studies [149, 150, 152]. In Farid's model [156], the time taken for the formation of crust on a colloidal silica droplet is calculated using the energy balance, which does not account for solvent and solute composition changes, and the evaporation rate is computed using a simple relation without accounting for the variation in film and liquid properties. For droplets with suspended solids inside, the population balance approach is recently developed [158] to model the nucleation and growth of suspended solids inside an ideal binary liquid droplet with an assumption that there exist some nuclei of suspended solids initially. But this method cannot be applied in the present case of droplet with polymer or sugar, as solute is completely dissolved in water. Golman *et al.* [160] presents a model for the evaporation and drying of slurry droplets, which is an improvement over the receding interface model of Cheong *et al* [161] for slurry droplets, and the bi-component liquid mixture is treated as ideal. A detailed review of all existing theoretical models of evaporation and drying of single droplet containing dissolved and insoluble solids is given by Mezhericher *et al.* [162], and a review of evaporation models in the area of combustion is given by Sazhin [147].

Adhikari *et al.* [163] and Vehring *et al.* [164] give a review of the experimental studies in the area of single droplet evaporation and drying. Tsapis *et al.* [159] and Sugiyama *et al.* [165] have levitated droplets using Leidenfrost phenomenon on a concave hot plate whereas Yarin *et al.* [166] levitated droplets using an acoustic levitator. This technique was successfully used to study shell buckling during particle formation [165]. A drawback of this approach is that the flow field and temperature field in the vicinity of the droplet are different from those of a free flowing droplet in a spray dryer. A chain of mono-disperse free falling droplets has been used by several experimental groups to study heat and mass transfer, drying, and particle formation processes. El Golli *et al.* [154] measured salt droplet evaporation and compared their results with a theoretical model. A similar technique to study the effect of drying rates on particle formation was used by Alexander and King [167] and El-Sayed *et al.* [168]. Wallack *et al.* [169] compared measured evaporation rates with a numerical

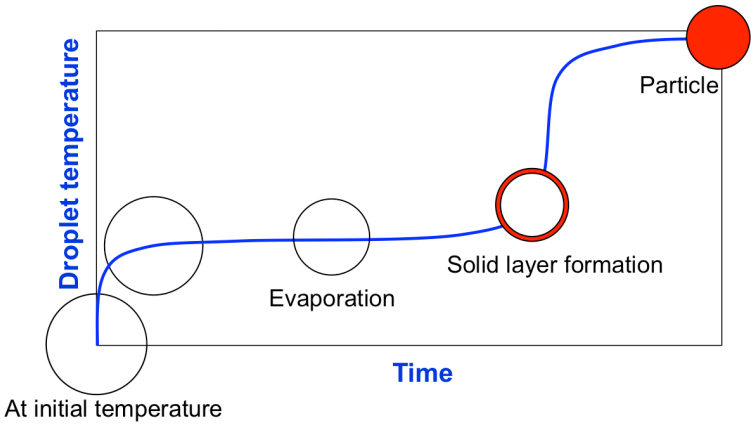

Fig. 2.5: Schematic diagram of stages in single droplet evaporation and drying.

model, achieving fairly good agreement. The droplet generators used in these studies produce a chain of closely spaced droplets, which leads to droplet–droplet interactions in processes that are limited by gas phase transport processes.

The aim of the present work is to develop a mathematical model, which can be applied to predict the evaporation and drying characteristics of droplets of the polymer PVP dissolved in water and mannitol dissolved in water solution. Prerequisites of the method are, (1) accounting for the solid layer resistance in mass evaporation rate and energy calculation, and (2) treatment of the liquid mixture as non-ideal by computing the activity coefficient of the evaporating component.

The problem under consideration is the evaporation and drying of an isolated single spherical droplet consisting of a binary mixture of a liquid and a dissolved solid material with low or zero vapor pressure.

During the evaporation and drying of the bi-component droplet, the droplet undergoes four stages as explained by Nesic and Vodnik [151], which are depicted in Fig. 2.5. In the initial stage, the droplet temperature quickly rises to an equilibrium temperature, which is most often near to the wet bulb temperature for surrounding gas and humidity, with some solvent evaporation.

In the second stage, the droplet starts to shrink as solvent evaporates causing the solute mass fraction to increase at the droplet surface; this leads to a slight raise in the droplet temperature (see Fig. 2.5). The increase in solute mass fraction at the droplet surface hinders further evaporation as the vapor pressure of the solvent at the surface drops. The third stage of drying starts when the solute mass fraction at the surface raises to a threshold value, which most often is equal to the saturation solubility of the solute in the solvent, whereupon the crust formation starts for salts, sugar and colloidal material. In the case of polymers, molecular entanglement and

gradual increase in concentration lead to solid layer formation at the droplet surface. In the latter case, the solid layer thickens and develops into the droplet interior as shown in Fig. 2.5, and a rapid fall in evaporation rate is observed. In this period, the heat penetrated into the liquid is used for heating the droplet, which causes the droplet temperature to rise rapidly. Further drying behavior of droplet depends on the vapor diffusivity through the solid layer. In the final stage of drying, boiling followed by particle drying, eventually leading to dried product formation, takes place.

The different assumptions in developing this mathematical model include the following:

1. The droplet remains spherical in shape throughout the evaporation with spherical symmetry.
2. Solubility of gas in liquid is negligible.
3. Gas phase is in a quasi-steady state.
4. No influence of chemical reactions occurs within and outside the droplet.
5. No heat transfer due to radiation.
6. No mass diffusion by temperature and pressure gradients.
7. No change in droplet radius once the solid layer formation starts.
8. Internal circulation of water and capillary effects are negligible.

The problem of evaporation and drying of a single droplet can be well defined using the species mass diffusion and heat conduction equations in spherical coordinates. The diffusion equation for the substance i in the droplet, formulated in terms of mass fraction Y_i, reads

$$\frac{\partial Y_i}{\partial t} = \frac{D_{12}}{r^2}\left[\frac{\partial}{\partial r}\left(r^2\frac{\partial Y_i}{\partial r}\right)\right], \tag{2.51}$$

where D_{12} is the binary diffusion coefficient in the liquid, r is the radial coordinate within the droplet radius, and t stands for time. In this equation $i = 1$ denotes the solvent (water) and $i = 2$ denotes solute (PVP or mannitol). Initially, the droplet is a homogenous mixture, $Y_i = Y_{i0}$ at $t = 0$ s. At the droplet center, $r = 0$ m, the regularity condition must be satisfied at any time, $\partial Y_i/\partial r = 0$. The boundary condition at the droplet surface must account for the change in droplet size,

$$-D_{12}\frac{\partial Y_i}{\partial r} - Y_i\frac{\partial R}{\partial t} = \frac{\dot{m}_i}{A\rho_\mathrm{l}} \tag{2.52}$$

at $r = R(t)$. Here $\dot{m}_i$ is the mass evaporation rate of substance i across the droplet surface, $R(t)$ and $A(t)$ are time dependent droplet radius and surface area, respectively,

and ρ_l is the liquid density. $\dot{m}_i$ is zero for non-evaporating solute (PVP or mannitol), $i = 2$. The diffusion process described through Eq. (2.51) provides the mass fraction profiles inside the droplet. In order to close this equation, the evaporation rate from the droplet surface, $\dot{m}_i$ is needed, which appears in Eq. (2.52). This rate of evaporation is determined based on Sherwood analogy of Abramzon and Sirignano's model [62], and in the present study, it is used in the extended form for a bi-component liquid mixture as modified by Brenn *et al.* [170],

$$\dot{m}_i = 2\pi R_i \rho_\mathrm{f} D_\mathrm{f} \widetilde{\mathrm{Sh}} \ln(1 + B_{M,i}), \tag{2.53}$$

where R_i is volume equivalent partial radius of component i, based on its corresponding volume fraction, computed as $R_i = R(V_i/V)^{1/3}$, $\widetilde{\mathrm{Sh}}$ is the modified Sherwood number defined by Eq. (2.42), which accounts for the effect of convective droplet evaporation [62], D_f is water vapor diffusivity in film, and ρ_f is the density in the film. $B_{M,i}$ is the Spalding mass transfer number for component i, and it is calculated as [62, 171],

$$B_{M,i} = \frac{Y_{i,\mathrm{s}} - Y_{i,\infty}}{1 - Y_{i,\mathrm{s}}}, \tag{2.54}$$

where $Y_{i,\mathrm{s}}$ and $Y_{i,\infty}$ are the mass fractions of evaporating component i at the droplet surface and in the bulk of the gas, respectively. Nesic and Vodnik [151] implemented a similar approach, but they do not account for the volume fraction based radius in the calculation of the evaporation rate, i.e., droplet radius R is used instead of R_i in computing $\dot{m}_i$. The evaporation rate retardation due to solid layer resistance may be considered through modification of Eq. (2.53) by extending the work of Nesic and Vodnik [151] to yield

$$\dot{m} = \frac{\sum_{i=1}^{N} 2\pi R_i \rho_\mathrm{f} D_\mathrm{f} \widetilde{\mathrm{Sh}} \ln(1 + B_{M,i})}{1 + \widetilde{\mathrm{Sh}} D_\mathrm{f} \delta / [2 D_\mathrm{s} (R - \delta)]}, \tag{2.55}$$

where $\dot{m}$ is the total evaporation rate, δ is the solid layer thickness at the droplet surface and D_s is the diffusivity of vapor in the solid layer. Since the solute vapor pressure is low or zero and the droplet's solute evaporation rate is zero or very small, negligence of the volume correction (using R in the place of R_i) may lead to an artificial increase in evaporation rate. In the present situation, the summation in Eq. (2.55) is only over component 1, because the solute (PVP or mannitol) does not evaporate, but for the sake of generality, the summation is kept.

During the initial and second stage, δ equals zero. But once the solute mass fraction at the droplet surface reaches a threshold value, which is most often near saturation solubility level, there is initiation of solid layer. This solid layer on the droplet surface offers significant resistance to evaporation and is evident from the second term in the denominator of Eq. (2.55) [172]. The effect of capillary force on water vapor diffusion

through solid layer due to pressure difference in pores is not considered, and it is the scope of the future study. Moreover, the influence of internal circulation within the droplet is neglected, which can be modeled by a correction for the diffusion coefficient rather than adding a convection term [151].

The heat conduction equation, describing the conductive heat transfer within the droplet, is written as

$$\frac{\partial T}{\partial t} = \frac{\alpha}{r^2}\left[\frac{\partial}{\partial r}\left(r^2\frac{\partial T}{\partial r}\right)\right], \tag{2.56}$$

where T is the liquid temperature and α denotes the thermal diffusivity. The above equation is solved with the following initial and boundary conditions: At $t = 0$ s, the droplet is at uniform temperature, $T = T_0$. At the droplet center, $r = 0$ m, zero gradient condition prevails at any time, $\partial T/\partial r = 0$. The energy balance at the droplet surface is given through the boundary condition,

$$k_\mathrm{l}\frac{\partial T}{\partial r} = h(T_\mathrm{g} - T_\mathrm{s}) + L_V(T_\mathrm{s})\rho_\mathrm{l}\frac{\partial R}{\partial t} \tag{2.57}$$

at $r = R$, where R is the droplet radius. In Eq. (2.57), T_s denotes droplet surface temperature, T_g stands for gas temperature in the bulk, k_l is the liquid thermal conductivity, h is the convective heat transfer coefficient, and $L_V(T_\mathrm{s})$ is the latent heat of vaporization at the surface temperature, T_s.

In this work, first Eq. (2.56) is solved numerically with initial and boundary condition as defined above using a finite difference method. It is observed that the gradient in droplet temperature from the center to the droplet surface is very small as the computed Biot number, which is a measure of heat transfer resistances within and outside the droplet, ($\mathrm{Bi} = h/k_\mathrm{s}R = k_\mathrm{g}/(2k_\mathrm{s})\mathrm{Nu}$), always remains below 0.5. Therefore, in the remaining simulations, uniform temperature within the droplet is assumed, which is a valid assumption as per the revelations made by Mezhericher *et al.* [173]. The droplet temperature continuously changes due to heat transfer from ambient gas to the binary liquid droplet, and it is computed using the energy balance across the droplet, which gives the net heat transferred into the droplet [62], as

$$mC_{p\mathrm{L}}\frac{dT_\mathrm{s}}{dt} = Q_\mathrm{L} = \dot{m}\left[\frac{C_{p\mathrm{Lf}}(T_\mathrm{g} - T_\mathrm{s})}{B_T} - L_V(T_\mathrm{s})\right], \tag{2.58}$$

where m is the total droplet mass, $m = \Sigma_{i=1}^{N} m_i$, $C_{p\mathrm{L}}$, $C_{p\mathrm{Lf}}$ are the specific heat capacity of liquid and in the film, respectively and B_T is the Spalding heat transfer number. This equation can be used to calculate the time evolution of droplet temperature. Here, the heat transfer number, B_T, is calculated in terms of mass transfer number defined by Eq. (2.47).

Equation (2.58) needs modification in order to account for the solid layer formation at droplet surface, and this is achieved through the equation written in terms of the

solid layer thickness, δ, as

$$mC_{p\mathrm{L}}\frac{dT_\mathrm{s}}{dt} = \frac{Q_\mathrm{L} + \dot{m}L_V(T_\mathrm{s})}{1 + \widetilde{\mathrm{Nu}}\, k_\mathrm{gf}\delta/[2k_\mathrm{s}(R-\delta)]} - \dot{m}L_V(T_\mathrm{s}), \tag{2.59}$$

where $\widetilde{\mathrm{Nu}}$ is the modified Nusselt number defined by Eq. (2.49), which accounts for the effect of convective droplet heating [62], k_s and k_gf are the thermal conductivity of the solid layer and in the film, respectively, and Q_L is the net heat transferred to the droplet [62], given by Eq. (2.58). Similar to Eq. (2.55), the second term in denominator inside the bracket of Eq. (2.59) denotes the resistance due to solid formation at the droplet surface, and its effect becomes significant only when the solid layer thickness, δ, is positive. The difference between heat transfer and mass transfer resistance is that the ratio of diffusion coefficients $D_\mathrm{f}/D_\mathrm{s}$ is larger than the ratio $k_\mathrm{g}/k_\mathrm{s}$ [151], which implies that resistance to mass transfer due to solid layer formation is higher than the heat transfer.

In the present study, simulations are also carried out with rapid mixing model (RMM) which is a simple model based on the assumption that the liquid mixture inside the droplet is always homogeneous (no spatial gradients of mass fraction within the droplet) and infinity conductivity within the droplet, thus the droplet is at uniform temperature at every time. In this work, the RMM is extended to account for solid layer resistance on the droplet evaporation rate and heating, thus the governing equations in the RMM are Eq. (2.55) and Eq. (2.59), and the time evolution of solute ($i = 2$) mass fraction is calculated based on the simple mass balance of solute and solvent mass fraction within droplet, given as

$$Y_{2,\mathrm{RMM}} = Y_{02} - \frac{m_{02}}{m - \dot{m}}, \tag{2.60}$$

where Y_{02} and m_{02} are the initial solute mass fraction and solute mass within the droplet, respectively.

2.4.2 Droplet Motion

The dynamics of liquid droplets in sprays is the basic physical process that needs to be computed for the coupling of gas–liquid phases due to its strong dependance on the flow of surrounding gas. The droplet velocity $\mathbf{v}$ at position $\mathbf{x}$ can be computed as following

$$\mathbf{v} = \frac{\mathrm{d}\mathbf{x}}{\mathrm{d}t}. \tag{2.61}$$

The acceleration of droplets due to different forces acting on droplets can be written as [174]

$$\frac{\mathrm{d}\mathbf{v}}{\mathrm{d}t} = \Sigma\mathbf{F} + \frac{\rho_\mathrm{g}}{2\rho_\mathrm{l}}\left(\frac{\mathrm{D}\mathbf{u}}{\mathrm{D}t} - \frac{\mathrm{d}\mathbf{v}}{\mathrm{d}t}\right), \tag{2.62}$$

where the first term in R.H.S includes all the forces such as aerodynamic drag, gravity, Basset, lift, and buoyancy etc. and the second term in R.H.S is the added mass force [174]. In Eq. (2.62), $\frac{\mathrm{D}}{\mathrm{D}t}$ is the substantial or material derivative.

The force experienced by the droplets due to difference in velocities of droplets and surrounding gas is known as drag force, $\mathbf{F}_d$. The droplet velocity evolution by interactive drag induced by the surrounding gas, and gravity per unit droplet mass is commuted using the following relation, which describes droplet motion [175]

$$\mathbf{F}_d = \frac{3}{8}\frac{1}{r}\frac{\rho_\mathrm{g}}{\rho_\mathrm{l}}(\mathbf{u}-\mathbf{v})|\mathbf{u}-\mathbf{v}|C_D + \mathbf{g}, \tag{2.63}$$

where ρ_g and $\mathbf{u}$ are the density and velocity of the surrounding gas, respectively, while ρ_l, C_D and $\mathbf{g}$ are liquid density, drag coefficient, and gravitational acceleration, respectively. The dependencies of the drag force are confined to the droplet radius, droplet shape, droplet density, ρ_l, relative velocity between gas and droplet, $\mathbf{u}-\mathbf{v}$, gas density, ρ_g, kinematic viscosity of the gas, η_g, and surface tension, σ_d.

The drag coefficient, C_D, is calculated as a function of the droplet Reynolds number, $\mathrm{Re_d} = 2r\rho_\mathrm{g}|\mathbf{u}-\mathbf{v}|/\mu_\mathrm{f}$, where μ_f is the mean dynamic viscosity in the film, as [176]

$$C_D = \begin{cases} \frac{24}{\mathrm{Re_d}}(1+\frac{1}{6}\mathrm{Re_d^{0.687}}) & \text{if } \mathrm{Re_d}<10^3 \\ 0.424 & \text{if } \mathrm{Re_d}\geq 10^3 \end{cases} \tag{2.64}$$

The Basset force describes the force due to the lagging boundary layer development with changing relative velocity or acceleration of the droplets/particles that are moving in a fluid [174]. The Basset force term accounts for viscous effects and the temporal delay in boundary layer, and it is also known as history term, given as [174]

$$\mathbf{F}_h = 6r^2\sqrt{\pi\mu_\mathrm{g}\rho_\mathrm{g}}\int_0^t \frac{\left[\frac{\partial \mathbf{u}}{\partial \tau} - \frac{\mathrm{d}\mathbf{v}}{\mathrm{d}\tau}\right]}{\sqrt{t-\tau}}\mathrm{d}\tau. \tag{2.65}$$

This force is however negligible for large ratios of droplet to gas density as well as low gas viscosity, and under steady state formulation, its contribution to total force on droplets is zero [174].

The lift force is due to the gas vorticity Ω_g, it is non-negligible for large droplets where the surrounding gas velocity gradient differs significantly from one side of the droplet to the other. It is written as,

$$\mathbf{F}_L = \frac{\rho_\mathrm{g}}{\rho_\mathrm{l}}(\mathbf{u}-\mathbf{v})\Omega_\mathrm{g}. \tag{2.66}$$

In the previous studies, it is shown that that contribution of lift force becomes negligible in case of large liquid to gas density ratios [174, 177].

The buoyancy force is an upward directed force exerted by the fluid that opposes the weight of the immersed object, and in this study, it is the force exerted by the

surrounding gas on the droplets. Buoyancy force is equal to the weight of the displaced gas due to droplet motion.

The added mass force, defined by second term in the right hand side of Eq. (2.62), accounts for the acceleration of the gas due to the droplet motion. When a droplet accelerates in gas, it implies an acceleration of the surrounding gas at the expense of the force exerted by the droplet. Since the added mass force depends on the fluid density, it is often neglected for droplets much denser than the gas [177]. In this work, the ratio between liquid density and gas density is about 10^3, so the effect of added mass can be neglected.

The unsteady behavior of the droplet, buoyancy effects, compressibility of the gas, rotation effects, the fluid motion within the droplet or other subtle forces are not considered. It can be shown [174] that terms originating from these phenomena are negligible for large ratios of droplet to gas densities, and for low droplet Mach numbers, $\mathrm{Ma} = |\mathbf{u} - \mathbf{v}|/c < 0.03$, where c is the speed of sound in the gas.

2.4.3 Droplet Breakup

Liquid drops generated from the primary breakup of the liquid sheet, moving in the surrounding gas may undergo further breakup or disintegration under certain conditions, leading to formation of smaller droplets. This phenomenon is called as droplet breakup or secondary atomization. The exact mechanisms of the droplet breakup is not yet completely understood as there are many uncertainties in the quantitative description of the process. The relative motion between a droplet and the surrounding gas causes a non-uniform distribution of pressure and shear stress on the droplet surface, which results in deformation of the droplet and cause it to disintegrate when they overcome the opposing force of surface tension. The newly formed droplets may still undergo further breakup until surface tension force of the newly formed droplet is higher than the external forces. The work of Pilch and Erdmann [178] explained the various regimes of breakup, which are depicted in Fig. 2.6. Faeth *et al.* [70] and Faeth [72] give an overview of existing mechanisms of droplet breakup.

According to Faeth *et al.* [70], the breakup regime transitions are mainly functions of the gas Weber number, $\mathrm{We_g}$, and the Ohnesorge number, Oh. The Weber number is defined as the ratio between the drag force to surface tension force, written as

$$\mathrm{We_g} = \frac{2r\rho_\mathrm{g}|\mathbf{u} - \mathbf{v}|^\mathbf{2}}{\sigma}, \tag{2.67}$$

where σ is the surface tension and r is the droplet radius. The Ohnesorge number, represents the ratio of viscous forces to inertial and surface tension forces, given as

$$\mathrm{Oh} = \frac{\mu_\mathrm{l}}{\sqrt{2\rho_\mathrm{l} r\sigma}}, \tag{2.68}$$

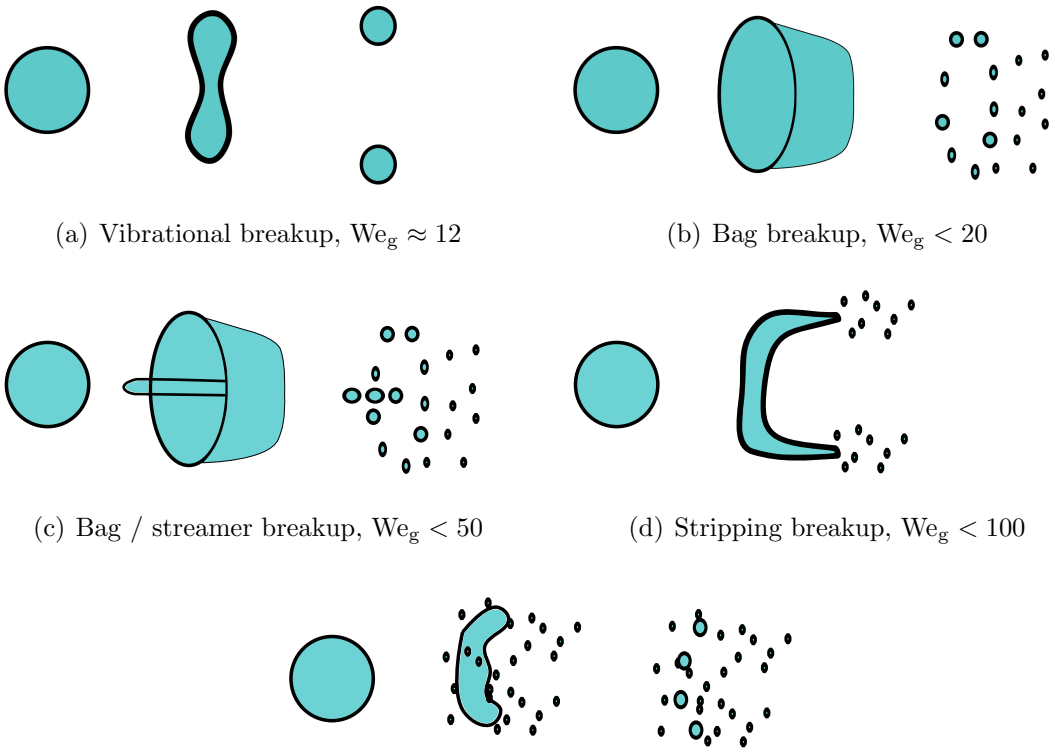

(a) Vibrational breakup, $We_g \approx 12$

(b) Bag breakup, $We_g < 20$

(c) Bag / streamer breakup, $We_g < 50$

(d) Stripping breakup, $We_g < 100$

(e) Catastrophic breakup, $We_g > 100$

Fig. 2.6: Droplet breakup mechanisms based on Weber number [69, 178].

where μ_l is the liquid viscosity. The existing breakup models developed based on the various mechanisms include, wave breakup (WB) model [179], Taylor analogy breakup (TAB) model [180], enhanced Taylor analogy breakup (ETAB) model [181], Rayleigh-Taylor instability (RTI) model [182], and droplet deformation and breakup (DDB) model [183]. Madsen [61] extended DQMOM to include droplet coalescence and breakup in spray flows by neglecting the effects of evaporation. In the present study, the focus is on the influence of droplet coalescence, evaporation and drag on droplet characteristics, and the study concerns the spray at a distance after the atomization, which may not breakup further, the droplet breakup is currently neglected.

2.4.4 Droplet Coalescence

The droplets in spray flows when come close enough, they interact with each other leading to collision of droplets. The collision dynamics of liquid droplets is important in the evolution of spray flows as they can significantly effect the spray characteristics such as droplet size and velocity distribution, and in turn influence the final powder characteristics in spray drying process.

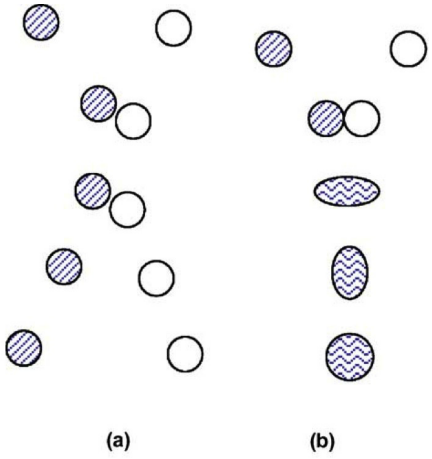

Fig. 2.7: Droplet collision regimes: (a) bouncing, (b) coalescence [184].

The outcome of the droplet collision is mostly dependent on the size, mass, surface tension, and velocity of colliding droplets. The collision outcome is classified into four different types: bounce, coalescence, reflexive separation and stretching separation. This classification is depicted in Figs. 2.7 and 2.8 [184]. Reflexive separation which occurs in head on and near-head on collision of droplets from miscible liquids does not exist for the immiscible liquids [185], and the collision mechanism in immiscible liquids is identified by Planchette and Brenn, and termed it as crossing separation [185].

The spray models developed to account for the droplet–droplet interactions mostly assume that there are only two possibilities of collision outcome: the droplets rebound without any change in droplet size or they coalesce to give a single droplet [186]. These models are only applicable to the study of two droplets colliding with each other but

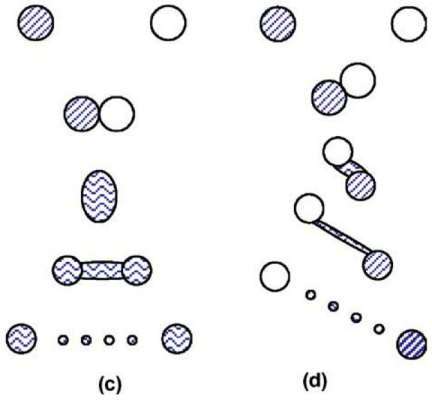

Fig. 2.8: Droplet collision regimes: (c) reflexive or crossing separation, (d) stretching separation [184].

not to the spray itself as the extension of these models to dense spray flows is much more complex [184], because of individual droplet tracking requirement. Implementation of droplet coalescence models needs tracking of individual droplets as done in Euler – Lagrangian simulations. In case of Euler – Euler models, droplet distribution is computed but the individual droplets are not tracked. Hylkema and Villedieu [187] developed a droplet collision model based on the droplet distribution, which can be implemented in Euler–Euler methods. In the current study, as the spray flow is modeled using Eulerian approach where the global droplet distribution is computed, so the droplet collisions are taken into account as described by Hylkema and Villedieu [187] and Laurent [46]. To emphasize upon coalescence only, standard assumptions [46] for droplet coalescence have been employed. These assumptions imply that each binary collision either leads to coalescence ($E_c = 1$) or rebound ($E_c = 0$), and conservation of mass and momentum before and after the collision [46] is assured. In addition, the mean collision time is assumed to be smaller than the inter-collision time. Thus, the coalescence function can be written in terms of the flux of newly formed droplet, Q_c^+ and flux of the vanishing droplets, Q_c^-, given by [187]

$$\Gamma_f = Q_c^+ + Q_c^-, \tag{2.69}$$

where Q_c^+ and Q_c^- are calculated as

$$Q_c^- = -\int_{-\infty}^{\infty}\int_{0}^{\infty} f(t,\mathbf{x};r,\mathbf{v})f(t,\mathbf{x};r_1,\mathbf{v}_1)\times B(|\mathbf{v}-\mathbf{v}_1|)\mathrm{d}r_1\mathrm{d}\mathbf{v}_1, \tag{2.70}$$

$$Q_c^+ = \int_{-\infty}^{\infty}\int_{0}^{\infty} \frac{1}{2} f(t,\mathbf{x};r_1,\mathbf{v}_1)f(t,\mathbf{x};r_2,\mathbf{v}_2)\times B(|\mathbf{v}_1-\mathbf{v}_2|)\mathrm{d}r_1\mathrm{d}\mathbf{v}_1, \tag{2.71}$$

where $B(|\mathbf{v}_1 - \mathbf{v}_2|)$ is given by,

$$B(|\mathbf{v}_1-\mathbf{v}_2|) = \pi(r_1+r_2)^2|\mathbf{v}_2-\mathbf{v}_1|E_c, \tag{2.72}$$

and $B(|\mathbf{v} - \mathbf{v}_1|)$ is defined accordingly. In the above equations, $(r, \mathbf{v})$ refer to post-collision properties, which are related to pre-collision properties $(r_1, \mathbf{v}_1)$ and $(r_2, \mathbf{v}_2)$ through the relations [46, 187]

$$\mathbf{v} = \frac{r_1^3\mathbf{v}_1 + r_2^3\mathbf{v}_2}{r_1^3 + r_2^3}, \tag{2.73}$$

$$r^3 = r_1^3 + r_2^3. \tag{2.74}$$

The collision efficiency is computed following the work of O'Rourke [186], which is written as

$$E_c = \frac{K^2}{(K+1/2)^2}, \tag{2.75}$$

where K is given as [186]

$$K = \frac{2}{9}\frac{\rho_l|\mathbf{v}_1 - \mathbf{v}_2|r_2^2}{\mu_g r_1}. \tag{2.76}$$

For DQMOM, substitution of all these sub-models defined in Subsection 2.4 into the Eq. (2.29) results in a linear system, which in turn is substituted into Eq. (2.30) to yield in a linear system of equations. The solution of this linear system gives the various source terms, i.e., a_n, b_n and $\mathbf{c}_n$ that appear in DQMOM transport Eqs. (2.26), (2.27) and (2.28), which then constitutes a closed system. The numerical solution procedure to solve these equations with initial and boundary conditions is explained in Chapter 3. Droplet–droplet interactions are currently neglected in DDM because of the computational complexity involved if Lagrangian models are used.

In summary, the new implementations of the present study include implementation of an advanced droplet evaporation model for water sprays in DQMOM, a new mathematical model development for the polymer or sugar dissolved in water droplets evaporation and solid layer formation at the droplet surface, and improvement of the evaporative flux calculation with maximum entropy formulation. Extension of DQMOM to simulate two-dimensional system, and implementation of developed bi-component evaporation model in DQMOM.

3. Numerical Methods

In the numerical simulation, the governing equations are discretized and solved by computer programs where appropriate numerical algorithms are required. An ideal numerical algorithm should

- be linearly stable for all cases of interest;
- ensure the positivity property when appropriate;
- be reasonably accurate;
- be computationally efficient.

There are several numerical methods available for the fluid mechanics. The methods ranging from the most discrete (or particulate) in nature to the most continuous (or global) include:

- particle methods
- characteristic methods
- Lagrangian finite difference/finite volume method
- Eulerian finite difference/finite volume method
- finite element methods
- spectral methods

Each method has advantages and disadvantages, consequently has the preferable applications. Usually, it is difficult or inefficient for a stand-alone method to simulate a complex system. Hybrid method, which is like a bootstrapping process, combines the advantages of the multiple methods and minimizes their disadvantages. The disadvantage of hybrid method is that the consistency problem is more serious. Special strategies are needed to keep consistency between the multiple methods.

In this chapter the numerical methods employed to solve the single droplet evaporation and drying equations, QMOM and DQMOM transport equations are explained. In this work, the DDM computations performed by Humza [68] are used to validate the DQMOM results for water spray in air in two-dimensional, axisymmetric configuration. Hence, the numerical details of the DDM simulations can be referred to Humza [68].

3.1 Finite Difference Method for Bi-component Droplet Evaporation and Solid Layer Formation

The partial differential equation, Eq. (2.51), with initial and boundary conditions is solved numerically at every time and spatial location within the droplet using second order explicit finite difference method, given as

$$\frac{Y_i^{j+1} - Y_i^j}{\Delta t} = D_{12} \frac{\left[r_{i+1}^2 (Y_{i+1}^j - Y_i^j) - r_{i-1}^2 (Y_i^j - Y_{i-1}^j)\right]}{r_i^2 \Delta r^2}, \tag{3.1}$$

where $r_{i+1} = r_i + \Delta r$, $r_{i-1} = r_i - \Delta r$, and i and j are the spatial location within the droplet and time step indices, respectively. Equation (3.1) can be simplified to yield the following equation

$$Y_i^{j+1} = Y_i^j + \frac{D_{12} \Delta t}{r_i^2 \Delta r^2} \left[r_{i+1}^2 (Y_{i+1}^j - Y_i^j) - r_{i-1}^2 (Y_i^j - Y_{i-1}^j)\right]. \tag{3.2}$$

The initial condition to compute Eq. (3.2) is provided as a Dirichlet condition, i.e., $Y = Y_{i0}$ at every location inside the droplet at $t = 0$. A Neumann boundary condition is applied at the center of the droplet, i.e., $\partial Y_i / \partial r = 0$ at $r = 0$, which implies the radial symmetry within the droplet. A Robin boundary condition is employed at the droplet surface, and it is given by Eq. (2.52).

The energy Eq. (2.59) is an ordinary differential equation, solved using Runge-Kutta 4^{th} order method. The droplet is discretized into equal distant grid points at any given time. As the droplet size decreases with time thereby the grid size changes because grid points are fixed, thus a moving grid problem is solved, and grid independency of the numerical method is tested using different grid sizes with the number of grid points varying from 10 to 100. The value of 50 grid nodes is found to perform well.

The numerical stability of the method is tested using various time steps following the Courant-Friedrichs-Lewy (CFL) condition [188]. The CFL condition defines the limiting criteria for the numerical grid size when the time step and fluid velocity are known, and it is defined as

$$C = \frac{u \Delta t}{\Delta x} \leq C_{\max}, \tag{3.3}$$

where C is the dimensionless number known as Courant number, u is the velocity, Δt and Δx are the time step and grid size, respectively. $C_{\max}$ is the maximum possible Courant number to get a stable numerical solution, and it is generally taken as any positive value lower than or equal to 0.5 [188]. The step-by-step procedure of Abramzon and Sirignano [62] is applied to calculate the mass evaporation rate given by Eq. (2.55). Numerical simulations of pure water, mannitol dissolved in water droplet evaporation

and solid layer formation is done to test the implementation of this algorithm and the numerical results are compared with experimental data. The results are presented in Chapter 4.

3.2 Spray Modeling

3.2.1 Finite Volume Method for QMOM

In the present study, QMOM is implemented with a three-node (three weights or number densities, three droplet radii, and three droplet velocities) closure approximation of the NDF, which requires a total of nine moments of the NDF to compute the initial data of droplet radii and velocities and corresponding weights. The transport equations are generated by selecting $k_1 \in \{0, 1, 2, 3\}$ and $k_2 \in \{0, 1\}$ in Eq. (2.24), which is equivalent to three-node closure. The choice of three-node closure with the mentioned values of k_1 and k_2 is proven to be accurate in previous studies [48, 49, 51]. The substitution of k_1 and k_2 values results in the following equations:

$$\frac{\partial M(0,0)}{\partial t} + \frac{\partial M(0,1)}{\partial \mathbf{x}} = \int_{-\infty}^{\infty}\int_{0}^{\infty}\left[-\frac{\partial\left(Rf\right)}{\partial r} - \frac{\partial(\mathbf{F}f)}{\partial \mathbf{v}} + Q_f + \Gamma_f\right] \mathrm{d}r\mathrm{d}\mathbf{v}, \tag{3.4}$$

$$\frac{\partial M(1,0)}{\partial t} + \frac{\partial M(1,1)}{\partial \mathbf{x}} = \int_{-\infty}^{\infty}\int_{0}^{\infty} r\left[-\frac{\partial\left(Rf\right)}{\partial r} - \frac{\partial(\mathbf{F}f)}{\partial \mathbf{v}} + Q_f + \Gamma_f\right] \mathrm{d}r\mathrm{d}\mathbf{v}, \tag{3.5}$$

$$\frac{\partial M(0,1)}{\partial t} + \frac{\partial M(0,2)}{\partial \mathbf{x}} = \int_{-\infty}^{\infty}\int_{0}^{\infty} v\left[-\frac{\partial\left(Rf\right)}{\partial r} - \frac{\partial(\mathbf{F}f)}{\partial \mathbf{v}} + Q_f + \Gamma_f\right] \mathrm{d}r\mathrm{d}\mathbf{v}, \tag{3.6}$$

$$\frac{\partial M(1,1)}{\partial t} + \frac{\partial M(1,2)}{\partial \mathbf{x}} = \int_{-\infty}^{\infty}\int_{0}^{\infty} rv\left[-\frac{\partial\left(Rf\right)}{\partial r} - \frac{\partial(\mathbf{F}f)}{\partial \mathbf{v}} + Q_f + \Gamma_f\right] \mathrm{d}r\mathrm{d}\mathbf{v}, \tag{3.7}$$

$$\frac{\partial M(2,1)}{\partial t} + \frac{\partial M(2,2)}{\partial \mathbf{x}} = \int_{-\infty}^{\infty}\int_{0}^{\infty} r^2 v\left[-\frac{\partial\left(Rf\right)}{\partial r} - \frac{\partial(\mathbf{F}f)}{\partial \mathbf{v}} + Q_f + \Gamma_f\right] \mathrm{d}r\mathrm{d}\mathbf{v} \tag{3.8}$$

$$\frac{\partial M(3,1)}{\partial t} + \frac{\partial M(3,2)}{\partial \mathbf{x}} = \int_{-\infty}^{\infty}\int_{0}^{\infty} r^3 v\left[-\frac{\partial\left(Rf\right)}{\partial r} - \frac{\partial(\mathbf{F}f)}{\partial \mathbf{v}} + Q_f + \Gamma_f\right] \mathrm{d}r\mathrm{d}\mathbf{v}. \tag{3.9}$$

The $M(0,2)$, $M(1,2)$, $M(2,2)$ and $M(3,2)$ fall away from the selected moment set defined by k_1 and k_2 values, and these four unclosed moments are computed in terms of the weights and abscissas:

$$M(0,2) = w_1 v_1^2 + w_2 v_2^2 + w_3 v_3^2, \tag{3.10}$$

$$M(1,2) = w_1 r_1 v_1^2 + w_2 r_2 v_2^2 + w_3 r_3 v_3^2, \tag{3.11}$$

$$M(2,2) = w_1 r_1^2 v_1^2 + w_2 r_2^2 v_2^2 + w_3 r_3^2 v_3^2, \tag{3.12}$$

$$M(3,2) = w_1 r_1^3 v_1^2 + w_2 r_2^3 v_2^2 + w_3 r_3^3 v_3^2. \tag{3.13}$$

These weights and abscissas are computed using the Wheeler algorithm (see Subsection 3.2.3). Similarly, if any of the terms on the right hand side of these Eqs. (3.4) – (3.9) contain unknown moments, they will be closed in the analogous manner.

To solve Eqs. (3.4) – (3.9) a numerical scheme based on a kinetic transport scheme to evaluate the spatial fluxes [96, 189] can be employed. A first-order, explicit, finite volume scheme for these equations can be written for the set of moments

$$M = \Big[M(0,0), M(1,0), M(0,1), M(1,1), M(2,1), M(3,1)\Big]^T \tag{3.14}$$

as

$$M_i^{n+1} = M_i^n - \frac{\Delta t}{\Delta x}\Big[G(M_i^n, M_{i+1}^n) - G(M_{i-1}^n, M_i^n)\Big] + \Delta t S_i^n \tag{3.15}$$

where n is the time step, i is the grid node, S is the right hand side estimate of Eqs. (3.4)– (3.9), and G is the flux function. Using the velocity abscissas, the movement of the quadrature node from left to right or right to left is determined. The flux function at any time step is expressed as [28]

$$G(M_i, M_{i+1}) = H^+(M_i) + H^-(M_{i+1}) \tag{3.16}$$

where

$$H^-(M) = w_1 \min(v_1, 0) \begin{pmatrix} 1 \\ r_1 \\ v_1 \\ r_1 v_1 \\ r_1^2 v_1 \\ r_1^3 v_1 \end{pmatrix} + w_2 \min(v_2, 0) \begin{pmatrix} 1 \\ r_2 \\ v_2 \\ r_2 v_2 \\ r_2^2 v_2 \\ r_2^3 v_2 \end{pmatrix} + w_3 \min(v_3, 0) \begin{pmatrix} 1 \\ r_3 \\ v_3 \\ r_3 v_3 \\ r_3^2 v_3 \\ r_3^3 v_3 \end{pmatrix}, \tag{3.17}$$

and

$$H^{+}(M) = w_1 \max(v_1, 0) \begin{pmatrix} 1 \\ r_1 \\ v_1 \\ r_1 v_1 \\ r_1^2 v_1 \\ r_1^3 v_1 \end{pmatrix} + w_2 \max(v_2, 0) \begin{pmatrix} 1 \\ r_2 \\ v_2 \\ r_2 v_2 \\ r_2^2 v_2 \\ r_2^3 v_2 \end{pmatrix} + w_3 \max(v_3, 0) \begin{pmatrix} 1 \\ r_3 \\ v_3 \\ r_3 v_3 \\ r_3^2 v_3 \\ r_3^3 v_3 \end{pmatrix}. \tag{3.18}$$

Higher-order flux schemes can also be developed to control numerical diffusion [190]. However, the key characteristics of the flux function is that the quadrature method provides a realizable set of weights and abscissas at every grid node that can be used to determine the node velocities. In the present study, only the steady state solution of Eqs. (3.4) – (3.9) is needed due to the fact that experimental data provides only the time averaged droplet properties. The steady form of Eqs. (3.4) – (3.9) is solved using Runge-Kutta 4^{th} order method. The QMOM simulations are carried out only for one-dimensional water spray in nitrogen in order to compare and validate DQMOM results, and the initial data for the QMOM simulations are generated from the experimental data by calculating the above moment set, and the initial data generation procedure is outlined in Chapter 4.

3.2.2 Finite Difference Scheme for DQMOM

A generalized model for three-dimensional physical space has been discussed for application to evaporating sprays [191]. At first, DQMOM is applied to study the steady spray flows in one physical dimension, i.e., in the axial direction x. Thus, inhomogeneous formulation also known as steady state form of DQMOM transport Eqs. (2.26) – (2.28) can be rewritten as below by neglecting the terms containing time, t,

$$\frac{\partial U_n}{\partial x} = S_n, \tag{3.19}$$

where

$$\begin{aligned} U_n &\in \{w_n v_n, w_n \rho_{\text{l}} r_n v_n, w_n \rho_{\text{l}} r_n v_n v_n\}, \\ S_n &\in \{a_n, \rho_{\text{l}} b_n, \rho_{\text{l}} c_n\}. \end{aligned}$$

Similarly, the homogeneous formulations of DQMOM transport Eqs. (2.26) – (2.28) can be rewritten as following by ignoring the spatial terms,

$$\frac{\partial U_n}{\partial t} = S_n, \tag{3.20}$$

where

$$\begin{aligned} U_n &\in \{w_n, w_n\rho_l r_n, w_n\rho_l r_n v_n\}, \\ S_n &\in \{a_n, \rho_l b_n, \rho_l c_n\}. \end{aligned}$$

To solve these equations, the choice of numerical scheme is important because this array of equations are strongly coupled. Different finite difference schemes with varying order of accuracy are tested. It has been shown [191] that Runge-Kutta 4^{th} order method can accurately solve the system of inhomogeneous equations represented by Eq. (3.19) and proven to be computationally efficient for DQMOM in one-dimensional physical space [191]. In the current study, the NDF is approximated by a three-node closure in DQMOM, which is proven to be accurate in previous studies [48, 49]. The three-node approximation of NDF implies that a total of nine coupled equations, which are generated by substituting $n = \{1, 2, 3\}$, in Eq. (3.19). These equations are solved to find the evolution of NDF, which is achieved by discretizing and estimating these equations with Runge-Kutta 4^{th} order method. At every spatial location within the geometry, the source terms are computed through the models proposed in Chapter 2. The flowchart shown in Fig. 3.1 outlines the step by step procedure of the computational code.

The previous studies concerning DQMOM in spray flows, transport equations are never solved in two-dimensional configuration but only in one dimension. In this study, the DQMOM transport equations are solved in two-dimensional (axial and radial direction) geometrical configuration for water and PVP/water sprays in air, by implementing a finite difference numerical scheme. At each axial and radial location, the coupled steady state transport equations of DQMOM are solved and the source terms such as droplet heating, evaporation rate, total forces acting on droplet and droplet coalescence are computed from the weights and abscissas available from the initial values at first iteration and from the last computed value in the next iterations. The steady form of the DQMOM transport Eqs. (2.26) – (2.28) in two dimensions can be written as

$$\frac{\partial U_n}{\partial x} + \frac{\partial E_n}{\partial z} = S_n, \tag{3.21}$$

where

$$\begin{aligned} U_n &\in \{w_n v_n, w_n\rho_l r_n v_n, w_n\rho_l r_n v_n u_n, w_n\rho_l r_n v_n v_n\}, \\ E_n &\in \{w_n u_n, w_n\rho_l r_n u_n, w_n\rho_l r_n u_n u_n, w_n\rho_l r_n u_n v_n\}. \end{aligned} \tag{3.22}$$

In Eq. (3.21), x is the axial direction, z is the radial direction, and the corresponding velocities are v and u, respectively. To keep the computational efficiency, ease of

application and numerical accuracy, a second order explicit finite difference scheme is applied to solve steady state form of Eqs. (2.26) – (2.28) [192], which are represented by Eq. (3.21). Thus the solution formula may be written as [193]

$$U_{n,i}^{j+1} = U_{n,i}^{j} - \frac{\Delta x}{\Delta z}\left[1.5E_i^j - 2E_{i-1}^j + 0.5E_{i-2}^j\right] + \Delta x S_i^j, \tag{3.23}$$

where i and j are grid nodes in radial and axial directions, respectively.

The above formulation is applied to an equidistant rectangular grid, where the size of each grid cell is 1.5×10^{-3} m in radial direction and 1.0×10^{-4} m in axial direction, resulting in a maximum of 80×1000 grid nodes. The initial data to start simulations in both the configurations, i.e, one and two-dimensional cases is generated from the experimental data provided by Dr. R. Wengeler, BASF Ludwigshafen (one-dimensional water spray in nitrogen) and Prof. G. Brenn, TU Graz (two-dimensional water and PVP/water spray in air) using Wheeler algorithm (see Subsection 3.2.3). The experimental data closest to the nozzle exit is taken for generating the initial data and the procedure for calculating this initial data from experiment is explained in Chapter 4 along with brief description about the experimental setup. The boundary conditions in solving DQMOM include (1) if droplets hit the axis of symmetry, they are reflected, and (2) Neumann boundary is applied for the lateral sides of the computational domain and exit plane. The experimental data available at other cross sections away from the nozzle exit is used to validate the simulation results. The flowchart of the computational code is illustrated in Fig. 3.1.

3.2.3 Wheeler Algorithm

The Wheeler algorithm developed by Sack and Donovan [136], requires $2N+1$ moments to compute N weights (number density) and N abscissas (droplet radii or velocities). The moment set is represented as $M = [M(0), M(1), ...M(2N+1)]^T$. This algorithm is used to generate the initial data in DQMOM whereas in QMOM it is used to compute the unknown moments. The first step in Wheeler algorithm is to compute the coefficients π_α based on these $2N+1$ moments of the distribution function $n(\xi)$, given as

$$\pi_{\alpha+1}(\xi) = \xi\pi_\alpha(\xi). \tag{3.24}$$

The above recursive relation has the properties of $\pi_{-1}(\xi) = 0$ and $\pi_0(\xi) = 1$. Here, α is a subset of number of moments $2N+1$, i.e., $\alpha \in 0, 1, 2..N-1$. From these coefficients $\pi_\alpha(\xi)$, a symmetric tridiagonal matrix is computed through some intermediate quantities:

$$\sigma_{\alpha,\beta} = \int n(\xi)\pi_\alpha(\xi)\pi_\beta(\xi)\mathrm{d}\xi, \tag{3.25}$$

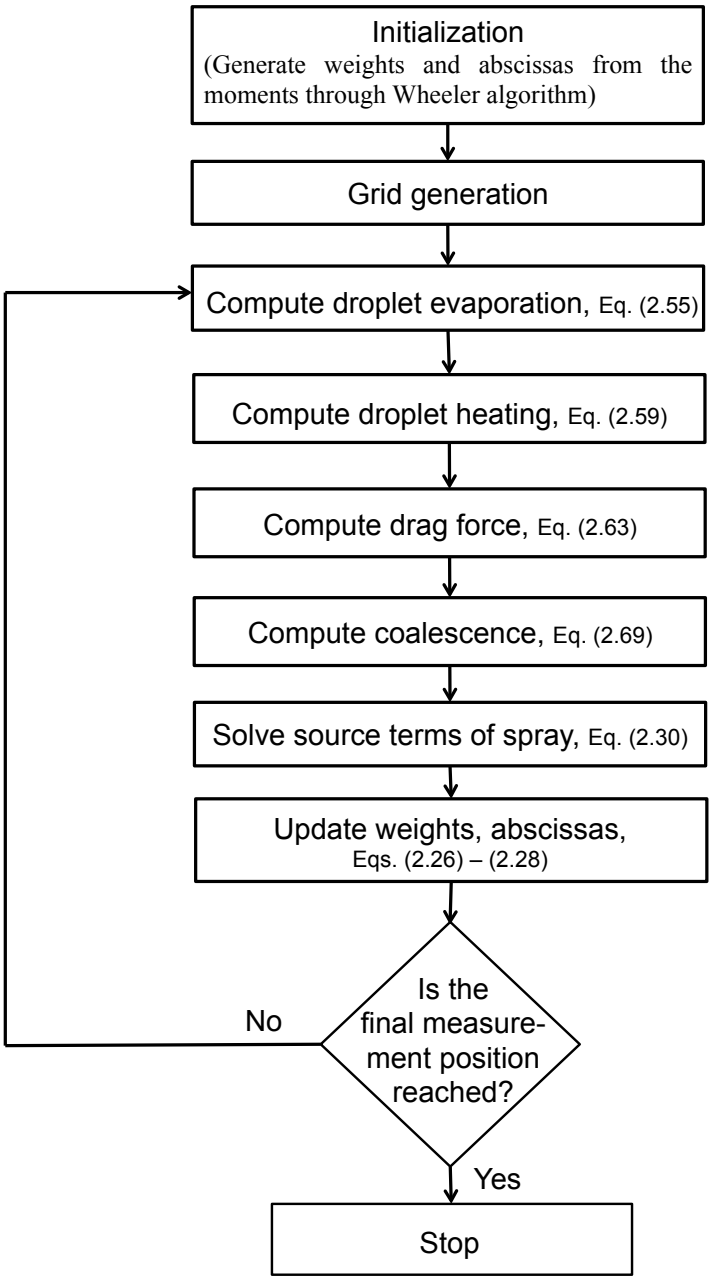

Fig. 3.1: Flowchart of the DQMOM computational code.

where $\beta \in \alpha, \alpha+1, ...2N-\alpha-1$. These quantities, $\sigma_{\alpha,\beta}$, are calculated by initializing

$$\sigma_{-1,\alpha} = 0, \tag{3.26}$$

$$\sigma_{0,\alpha} = M(\alpha), \tag{3.27}$$

and $a_0 = M(1)/M(0)$, $b_0 = 0$. The recurrence relation is

$$\sigma_{\alpha,\beta} = \sigma_{\alpha-1,\beta+1} - a_{\alpha-2}\sigma_{\alpha-1,\beta} - b_{\beta-1}\sigma_{\alpha-2,\beta}, \tag{3.28}$$

where the tridiagonal matrix components are given as

$$a_\alpha = \frac{\sigma_{\alpha,\alpha+1}}{\sigma_{\alpha,\alpha}} - \frac{\sigma_{\alpha-1,\alpha}}{\sigma_{\alpha-1,\alpha-1}}, \tag{3.29}$$

$$b_\alpha = \frac{\sigma_{\alpha,\alpha}}{\sigma_{\alpha-1,\alpha-1}}. \tag{3.30}$$

Here, the values of a_α are the diagonal elements and b_α are the upper and lower diagonal elements of the symmetric tridiagonal matrix. The eigenvalues of this matrix are the abscissas (droplet radii, velocities) where as the corresponding eigenvectors are the weights (number densities). More details about derivation of this algorithm is given by Gautschi [194], and example calculations are given by Marchisio and Fox [71].

3.3 Numerical Performance

For the DDM computations, which are carried out Humza [68], a hybrid finite volume method based on the SIMPLER (Semi-Implicit Method for Pressure-Linked Equations - Revised) algorithm [68, 195] is used to solve the mean conservation equation of the gas flow, and a Lagrangian stochastic droplet parcel method is used for the spray flow. The initial and boundary conditions are generated from the experimental data. A non-equidistant rectangular numerical grid is used, which is finer in the region near the nozzle exit with a total of 78 $\times$ 101 grid nodes. The numerical time step for the governing gas phase equations is controlled by applying the CFL condition [188]. The solution algorithm and numerical details of the DDM calculation are given by Humza [68].

The DQMOM simulations are carried out on a PC with two Intel dual core 2.2 GHz processors having 8 GB RAM. The DDM is simulated on a PC having an AMD quad Opteron 1.8 GHz processor with 64 GB RAM [68]. The latter PC had several jobs running simultaneously, so that the available RAM on both the PCs is about identical. All simulations are run on a single processor. The computations for DQMOM and DDM take about one hour and three days, respectively. Thus, the DQMOM computations show a much better performance with respect to the computational cost.

4. Results and Discussion

Results presented in this chapter are categorized into four sections based on the model development and implementation, which are discussed successively: At first, one-dimensional water spray in nitrogen results are given, followed by the results of two-dimensional evaporating water spray flows in air in axisymmetric configuration. Later, single bi-component droplet evaporation and solid layer formation results are discussed, and finally, results of PVP/water spray in air in an axisymmetric configuration are presented.

4.1 One-dimensional Evaporating Water Spray in Nitrogen

A spray can be generated by pumping the liquid through a nozzle that facilitates dispersion of liquid into a spray. Nozzles are mainly used to distribute a liquid over an area thereby liquid surface area is increased. There are three types of nozzles normally used, which include spinning disk nozzle, single-fluid or centrifugal pressure nozzle, twin-fluid nozzle [196]. The spinning disk nozzles are also known as rotary atomizers. The single-fluid nozzles include pressure-swirl nozzle, plain-orifice nozzle, hollow cone nozzle, etc., whereas the twin-fluid nozzles can be internal-mix or external-mix two-fluid atomizers [196]. The present study concerns the simulation of water spray generated using a hollow cone nozzle, which is single fluid nozzle. However, the model presented in this work is equally applicable to other type of nozzles as the current work focuses on the simulation of spray after the primary breakup.

Evaporating sprays are of special interest as those occur not only in many industrial applications but also constitute the defining physical phenomena in spray drying process. Therefore, having models validated for evaporating sprays motivate their application in simulations of spray drying. A water spray injected through a hollow cone Delavan SDX-SE-90 nozzle in a vertical spray chamber and carried by nitrogen is simulated by DQMOM and the results are compared with the QMOM, and validated with the experiment.

Fig. 4.1: Photograph of the water spray formation.

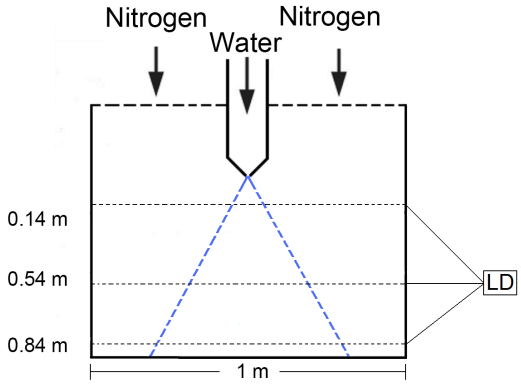

Fig. 4.2: Schematic diagram of spray with measurement positions.

4.1.1 Experimental Setup

Experiments have been carried out by Dr. R. Wengeler at BASF, Ludwigshafen, where a water spray is injected into a cylindrical spray chamber. The carrier gas is nitrogen at room temperature. Three different experiments are conducted by keeping the spray inflow rate at 80, 150 and 200 kg/h while the gas volumetric flow rate is fixed at 200 Nm^3/h. The droplet size distribution is recorded at sections of 0.14, 0.54, and 0.84 m distance from the nozzle exit using laser Doppler anemometry (LDA). Measurements at 0.14 m are taken as a starting point for initial data generation for computations. Figure 4.1 shows the photograph of water spray formation in experiment, and the schematic representation of spray with dimensions and measurement positions in experiment is shown in Fig. 4.2. The spray column has a diameter of 1 m. The present simulations concern the experimental data generated using the Delavan nozzle SDX-SE-90 with an internal diameter of 2 mm and an outer diameter of 12 mm at the nozzle throat and 16 mm at the top.

4.1.2 Initial Data Generation

The experimental data provide the cumulative volume frequency of different droplet sizes. These volume frequencies are converted into surface frequencies by dividing the individual volume frequency with the corresponding diameter. Figure 4.3 shows the surface frequencies at the distance of 0.14 m (left) and 0.54 m (right) from the nozzle exit, respectively, as obtained from the experimental data. At 0.14 m distance away from the nozzle, there is a higher number of small-sized droplets shown in the left side of Fig. 4.3, whereas at 0.54 m distance, an increased number of larger size droplets is found, see right part of Fig. 4.3. The droplet velocities are not measured in the

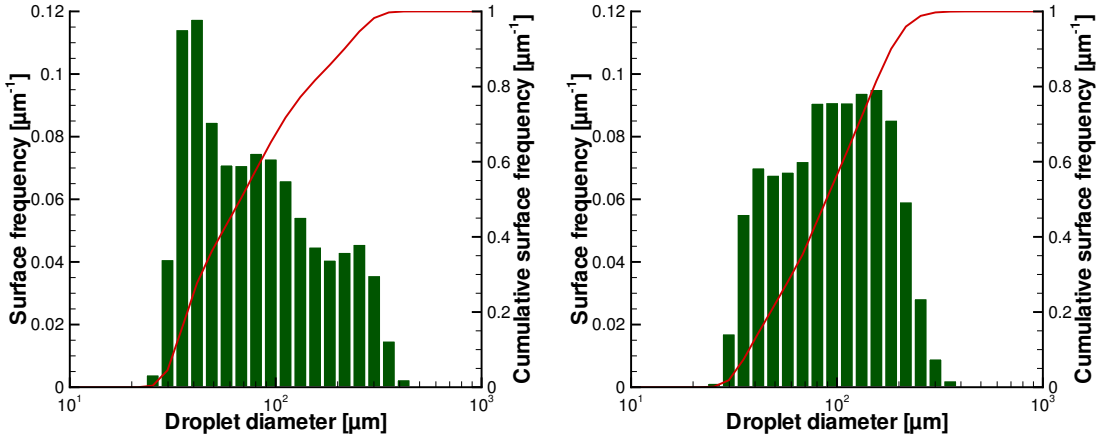

Fig. 4.3: Experimental surface frequency distribution at cross section 0.14 m (left) and 0.54 m (right) away from the nozzle exit.

experiments, and they are calculated using the relation

$$v = 1.74\sqrt{\frac{\rho_\mathrm{l} - \rho_\mathrm{g}}{\rho_\mathrm{g}} g d} \tag{4.1}$$

given by Stieß [197], where d is droplet diameter, ρ_l and ρ_g are the liquid and gas densities, respectively, and g is the acceleration due to gravity. This relation is the estimate of the terminal velocity of the droplets [197], and it is proven to give accurate value of the droplet velocity [191, 198]. The moment sets are calculated by means of these droplet radius, velocity and surface frequency, which are used as initial data for QMOM whereas for DQMOM these moments are in turn used to calculate the weights (representing surface frequencies), radii and velocities through the Wheeler algorithm [136] as explained in Chapter 3. These data (weights, radii and velocities) are then used as initial data to start the computations. Tab. 4.1 lists these initial values with three-node approximation for 80 kg/h and 150 kg/h water inflow rate.

Tab. 4.1: Initial weights and abscissas

Liquid flow rate [kg/h]	Weights [(µm)$^{-1}$]	Radii [µm]	Velocities [m/s]
80	0.638	24.424	1.09
	0.276	86.432	1.94
	0.086	143.29	2.76
150	0.733	21.739	1.03
	0.223	79.706	1.84
	0.044	128.350	2.72

4.1.3 Results and Discussion

In this subsection, the simulation results of DQMOM in one dimension are presented, and compared with experimental data and with the simpler model QMOM. Computations are carried out considering different ambient gas temperatures, i.e. 293 K, as in experiments, and 313 K, and different inflow rates of liquid as in experiments in order to investigate the effect of evaporation and drag force along with gravity on droplet characteristics and spray dynamics. The gas inflow rate remains fixed in accordance with experiments. Although the surrounding gas velocity is fixed as 0.078 m/s in experiments, the simulations are performed using different velocities of surrounding gas in order to analyze the effect of drag force on the droplet dynamics. Also, the cases of spray with and without coalescence are compared to analyze the influence of coalescence on droplet distribution.

First, the implementation of the droplet evaporation model is tested for a single pure water droplet. The numerical predictions and experimental results of water droplet mass and temperature are shown in Fig. 4.4. The experimental data are taken from Werner [199], and refer to a 6 µl water droplet evaporation in air at 40 °C, 3.75% relative humidity (R.H.) and flow velocity of 0.3 m/s. The droplet mass continuously decreases due to water evaporation, and initially there is no significant increase in droplet temperature. When the droplet mass reduces to a negligible value (less than 5% of its initial mass), temperature raises quickly to the gas temperature, and there is good agreement between the simulation and the experiment.

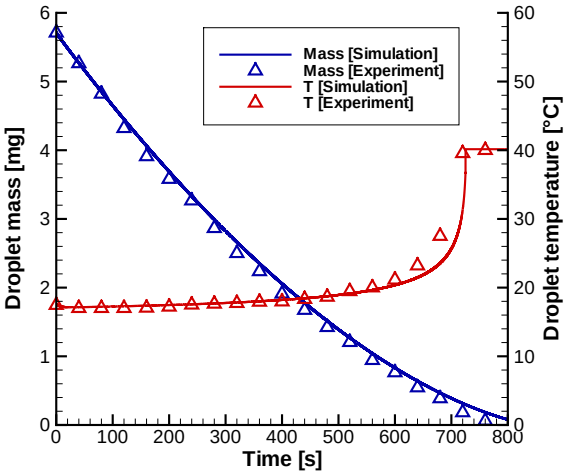

Fig. 4.4: Comparison of simulated and measured [199] droplet mass and temperature profiles for the evaporation of a pure water droplet.

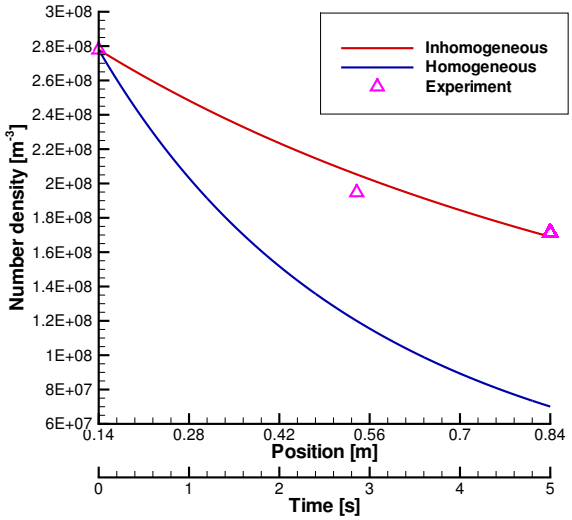

Fig. 4.5: Homogeneous and inhomogeneous calculations of DQMOM.

Before carrying out simulations with an inhomogeneous system of DQMOM transport Eq. (3.19), homogenous formulations of these equations, given by Eq. (3.20), are simulated and the results are compared with inhomogeneous computations. Fig. 4.5 shows the computed and experimental profiles of number density at different cross sections of the spray chamber with homogeneous and inhomogeneous system of DQMOM equations (see Eq. (3.19)) for 80 kg/h water spray in nitrogen flowing with 0.078 m/s velocity at 293 K. In the homogeneous results, the time axis of the model is matched to experimental position through the droplet velocity. The number density decreases along the spray axis due to droplet evaporation, and the predictions with inhomogeneous formulation captures the physics of the spray more accurately [198, 200]. Thus, the present work includes the numerical solutions of the inhomogeneous linear system, which are formed through application of DQMOM in one physical dimension (axial direction).

Figure 4.6 displays the results of Sauter mean diameter showing the comparison of QMOM and DQMOM, where DQMOM results are shown for both lower and higher Reynolds number. Here, the liquid flow rate is 80 kg/h. It can be seen that the QMOM results strongly deviate from the experiment whereas DQMOM improves the results of QMOM significantly even for lower droplet Reynolds numbers, and with higher Reynolds number, which is the case in this simulations, the agreement between DQMOM and experiment is very good [191]. A general intuitive question could be "why the Sauter mean diameter increases in spite of evaporation in simulations as well as the experiment?". The answer is elaborated with an example by considering the droplet size distribution of a water spray shown in Fig. 4.7, which displays the droplet

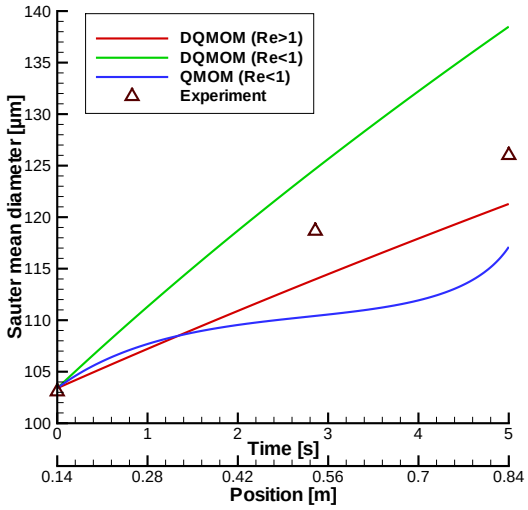

Fig. 4.6: Comparison of QMOM and DQMOM results with experiment.

diameter, d, and its corresponding number density, f. The same data is given in Tab. 4.2, see the first two columns. The Sauter mean diameter, d_{32}, of this distribution can be calculated using the Eq. (2.20), which is written in discrete form given as

$$d_{32} = \frac{\Sigma_{i=1}^{n} d_i^3 f_i}{\Sigma_{i=1}^{n} d_i^2 f_i}, \tag{4.2}$$

and the d_{32} at $t = 0$ s is, thus, computed 112.126 μm. This distribution is subjected to evaporation by considering d^2 law, i.e., $d^2(t) = d^2(t = 0) - kt$, where k is a constant.

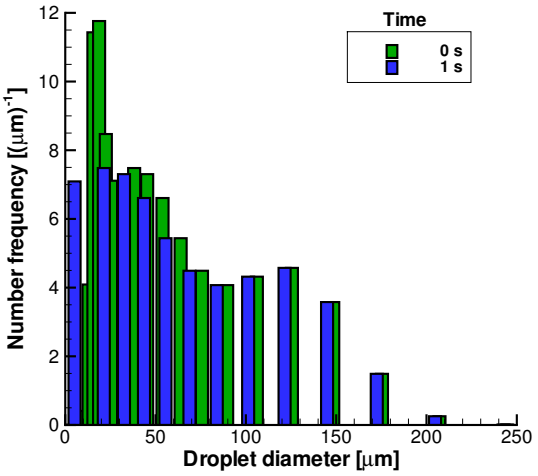

Fig. 4.7: Droplet size distribution of water spray and at $t = 0$ s, and at $t = 1$ s with d^2 law evaporation rate.

Tab. 4.2: Droplet size distribution of water spray

$d(t = 0$ s) [μm]	f [(μm)$^{-1}$]	d(t = 1 s) [μm]	$d(t = 50$ s) [μm]]
10.643	0.409	0.000	0.000
12.913	4.091	0.000	0.000
15.588	11.434	0.000	0.000
18.745	11.762	0.000	0.000
22.468	8.472	0.000	0.000
26.858	7.112	0.000	0.000
32.037	7.093	5.138	0.000
38.145	7.481	21.332	0.000
45.350	7.304	32.506	0.000
53.848	6.609	43.584	0.000
63.870	5.439	55.492	0.000
75.692	4.491	68.770	0.000
89.635	4.073	83.872	0.000
106.080	4.319	101.257	0.000
125.478	4.574	121.427	0.000
148.355	3.579	144.946	0.000
175.337	1.490	172.462	0.000
207.163	0.255	204.735	0.000
244.697	0.015	242.646	99.381

The k value is usually estimated from the material properties such as density, diffusivity, etc., and in general, it has a value in the range of 10^{-7} to 10^{-11}. Just for the sake of explanation, k is assumed to be 1.0E-09 m^2/s. The change in the droplet diameter is computed at $t = 1$ s using d^2 law is given in Tab. 4.2, see the third column. Comparing the values of droplet diameter at $t = 0$ s and $t = 1$ s, it shows that the droplet diameter decreases and lower size droplets vanish. Using these data, the computed d_{32} at $t =$ 1 s is 117.126 μm, which shows an increase from initial value. This increase continues till certain evaporation time (see last column in Tab. 4.2), whereupon the Sauter mean diameter starts to decrease because most of the smaller size droplets vanish and only few droplets have finite size. The Sauter mean diameter of this distribution decreases to 99.381 μm after 50 s of d^2 law evaporation rate (see the last column in Tab. 4.2).

Figure 4.8 shows the plots of droplet velocities subjected to only drag force (left), and drag force with gravity (right) for three different sized droplets, respectively. In case of only drag caused by the surrounding gas with initial velocity of 0.078 m/s (experimental value), the velocity decreases at first due to drag force and later the droplets

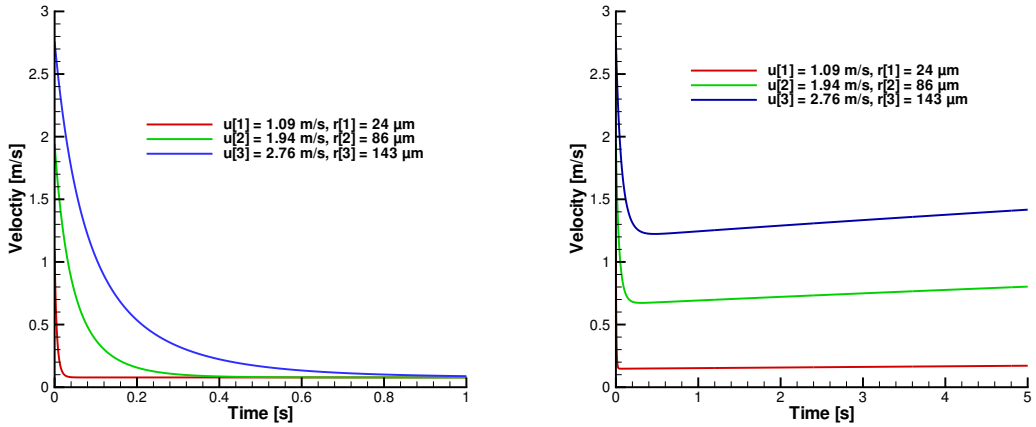

Fig. 4.8: Velocity profiles of three droplets with different initial radii and velocities under the influence of drag alone (left) and drag and gravity (right).

follow the streamlines of the gas after reaching a steady value, cf. left side of Fig. 4.8. On the other hand, when the droplets encounter gravity in addition to drag force applied by the surrounding gas, the droplet velocity initially decreases due to drag and then increases linearly due to gravity as seen in right part of Fig. 4.8. In a previous study [198, 200], it has been shown that the moderate droplet evaporation under the present conditions does not significantly influence droplet velocity.

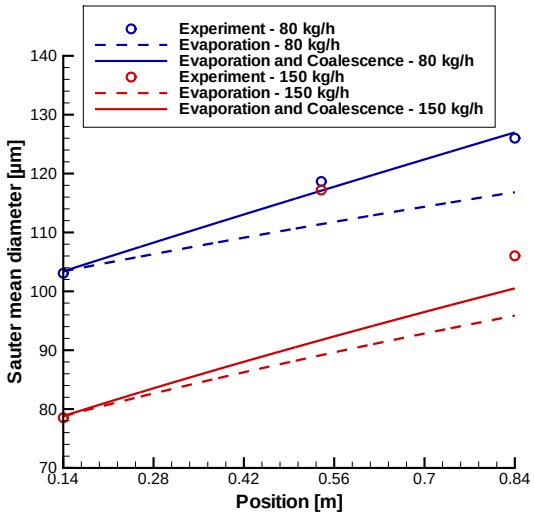

Fig. 4.9: Effect of liquid inflow rates on Sauter mean diameter computed with and without coalescence.

The variations in Sauter mean diameter with axial position of the spray for two different liquid inflow rates of 80 kg/h and 150 kg/h are shown in Fig. 4.9. The results for 80 kg/h show an increasing Sauter mean diameter with evaporation. Inclusion of coalescence in addition to evaporation leads to excellent agreement between computational and experimental results. On the contrary, the computational results for 150 kg/h at x = 0.54 m seem to be deviating far away from the experimental data. The observed deviation is due to inconsistency in experimental data, which is evident from the fact that the experimental flow rate does not match the prescribed value of 150 kg/h at 0.54 m. Therefore, the results from 80 kg/h will be discussed for the remaining part of this section.

Figure 4.10 displays the profiles of the Sauter mean diameter (left) and mean droplet diameter (right) of water spray subjected to evaporation at 293 K and 313 K temperatures of surrounding gas as well as with and without coalescence. As expected, Sauter mean diameter increases substantially with evaporation that causes the decrease and eventual loss of small size droplets. Higher temperature imposes a rise in evaporation, which considerably accelerates the rate of increase of Sauter mean diameter. A comparison with experimental data reveals the importance of modeling the droplet coalescence, which not only improves the simulation results but also has excellent agreement with experiment (see left side of Fig. 4.10).

Similar to Sauter mean diameter, the mean droplet diameter is an important physical quantity for several applications such as particle size analysis of powder sampling in food and pharmaceutical industries [201]. Mean droplet diameter of a number density based distribution can be computed using the Eq. (2.18). Since very small size

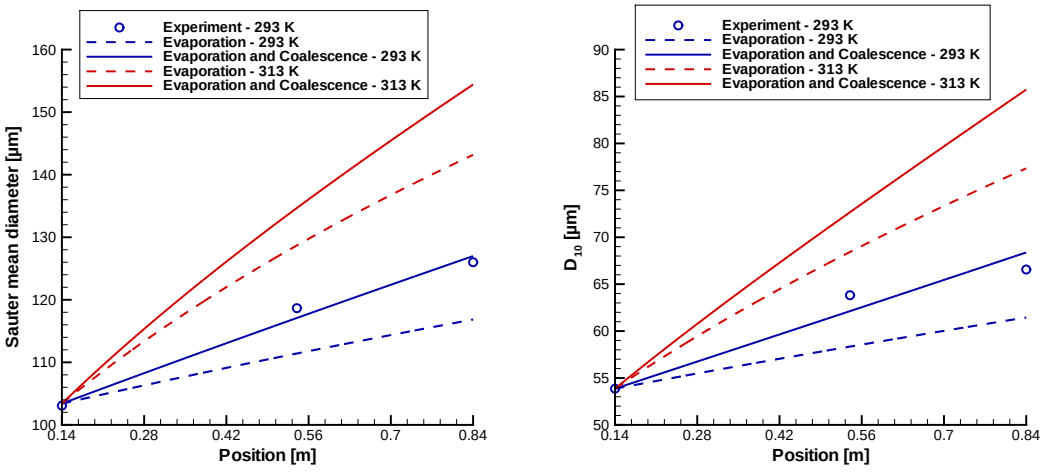

Fig. 4.10: Profiles of Sauter mean diameter (left) and mean droplet diameter (right) computed with and without coalescence at surrounding gas temperatures of 293 K and 313 K.

droplets may completely evaporate, leading to decreased total droplet number at any cross section, cf. Fig. 4.12, the mean value of droplet diameters increases. Therefore, as the droplets move and start to evaporate and vanish completely, the mean droplet diameter of the spray starts increasing at cross sections away from the nozzle although individual droplet diameters decrease (see right part of Fig. 4.10). This observation is in agreement with the behavior of the Sauter mean diameter shown in left side of Fig. 4.10. Coalescence causes an increase of droplet diameter as anticipated.

Figure 4.11 shows the results of the droplet specific surface area. The specific surface area is an important parameter, which is used particularly to characterize powder materials, and it is defined as the ratio of total surface area of the individual droplets/particles to the total volume [201]. It can be seen that the specific surface area decreases as a result of evaporation, which leads to decrease in number density of droplets. This is evident from the behavior of specific surface area at a higher temperature. A comparison with experimental data confirms the role of coalescence in improving the results as observed in case of the Sauter mean diameter and the mean droplet diameter displayed in Fig. 4.10.

Figure 4.12 shows the plots of total droplet number density in axial direction. Since the geometric configuration considered for the numerical solution is one-dimensional, the integral value of droplet number density over the corresponding cross sections is displayed. It can be seen that evaporation causes the droplet number density to decrease as the spray develops. This decrease is much pronounced at the higher temperature (313 K) due to enhanced evaporation. It is worthwhile to note that inclusion

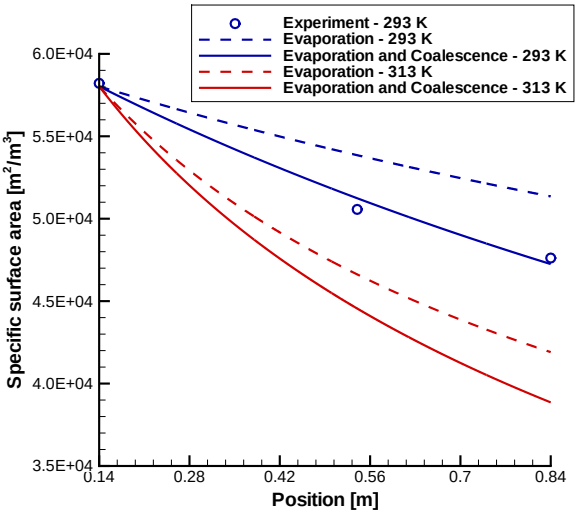

Fig. 4.11: Profiles of specific surface area computed with and without coalescence at surrounding gas temperatures of 293 K and 313 K.

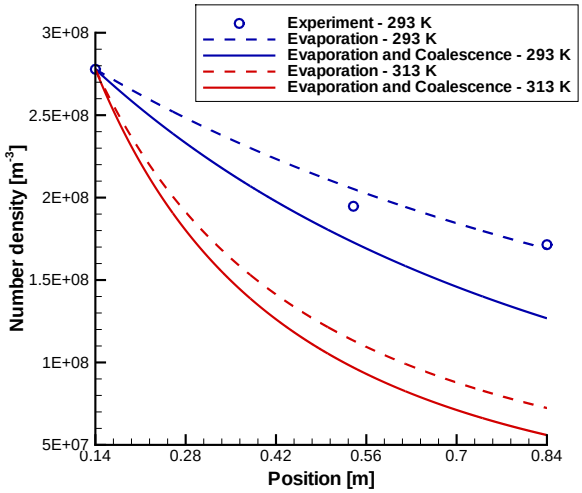

Fig. 4.12: Profiles of droplet number density computed with and without coalescence at surrounding gas temperatures of 293 K and 313 K.

of coalescence affects the calculation of droplet number density significantly as it can be inferred through comparison of the numerical results with experimental data. This may be understood by the fact that only coalescence is considered in the present work and processes of breakup, reflexive and stretching separation along with formation of satellite droplets is neglected in the present simulations, which leads to a lower droplet number density at any given position. This may be improved by including a more advanced droplet–droplet interaction model [184]. Moreover, in these computations the evaporating flux at zero droplet size is computed through the ratio constraints of weights, radii and velocities given by Eqs. (2.33)– (2.34), which are derived based on a smooth and continuous density function [60]. This approach is prone to errors and may be rectified by implementing an maximum entropy model [66] explained in Section 2.3.4, which is done in the case of two-dimensional water and PVP/water in air spray flows.

The successful implementation of DQMOM in studying the one-dimensional water spray flow in nitrogen and the good agreement with experimental data has led to the extension of DQMOM to two dimensions in order to model the evaporating water spray in air in two-dimensional configuration. The DQMOM extension is outlined in Section 2.3.4. The next section presents the results of two-dimensional water spray in air in axisymmetric configuration.

4.2 Two-dimensional Evaporating Water Spray in Air

A water spray injected into air through a hollow cone Delavan SDX-SE-90 nozzle in a vertical spray chamber, is modeled by DQMOM and DDM. The one-dimensional transport equations of DQMOM [191] are extended to two-dimensional to model the spray flow in axisymmetric configuration [202, 203]. The starting data for the simulations are taken from experimental data, where the experiments are conducted by the group of Prof. G. Brenn at TU Graz, Austria. The experimental setup is explained in the next section. The generation of initial data is discussed in the following section. The simulation results of DQMOM are compared with the results of DDM and both these model results are validated with the experiment [202, 203].

4.2.1 Experimental Setup

A series of experiments is carried out at TU Graz by the group of Prof. G. Brenn where a water spray in air is studied for different liquid mass inflow rates. The droplet sizes and velocities are recorded at various cross sections for different liquid inflow rates using phase Doppler anemometry (PDA) [204]. The present simulations concern the experimental data generated using a Delavan nozzle SDX-SE-90 having an internal diameter of 0.002 m, an outer diameter of 0.012 m at the nozzle throat and 0.016 m at the top, for liquid inflow rates of 80 kg/h and 120 kg/h. A water spray is injected into a cylindrical spray chamber of diameter 1 m. The carrier gas is air at room temperature and atmospheric pressure. Measurements are recorded at cross sections of 0.08 m, 0.12 m and 0.16 m. Figure 4.13 illustrates the schematic of the experimental

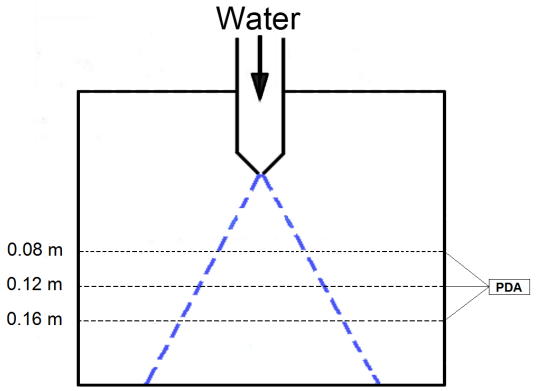

Fig. 4.13: Schematic diagram of the experimental setup.

setup. The data at 0.08 m are taken as starting point for initial data generation for computations, and results are compared at later cross sections [205].

4.2.2 Initial Data Generation

The experimental data at the closest position to the nozzle is used to generate initial data for the numerical computations of DQMOM. The nearest experimental position is 0.08 m from the nozzle, where the measurements are available at radial positions separated by 1.5×10^{-3} m distance. The PDA data at every radial position consists of droplet radius, velocities in axial and radial directions, and the time elapsed for each measurement, which gives the total time carried out over a period. These data are grouped into 100 droplet size classes [206]. The effective cross sectional area of the probe volume is computed, which is done to eliminate errors in measuring volume due to nonlinearity in phase/diameter relationship in large size droplets because of the nonuniform beam intensity [207]. The result of the calculation for a water flow rate of 80 kg/h, at a position of 0.066 m from the center is shown in Fig. 4.14. The trajectory length exhibits strong fluctuations, and fluctuations increase with the droplet size. Furthermore, the number of droplets in the size classes for the larger diameters is typically much lower than in the smaller size classes. Therefore, the properties such as droplet trajectory lengths through the probe volume are statistically unreliable for drops with sizes greater than a certain threshold value [206, 207]. In particular, the decrease of the effective probe volume size with increasing droplet size such as from

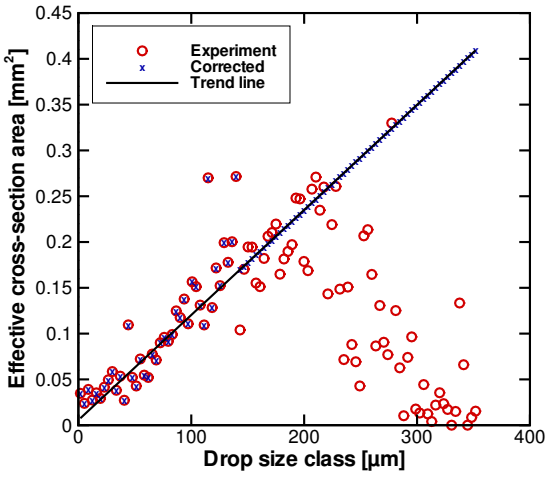

Fig. 4.14: Profile of effective cross-section area of the probe volume for measured droplet size.

200 µm as shown in Fig. 4.14 is invalid as the effective cross-sectional area should increase with droplet size [207]. The effective cross-section area is therefore calculated using a linear trend line from a threshold diameter. In the first step, the linear trend line is calculated using a linear regression scheme based on the data in the droplet size classes up to 60% of the maximum droplet size.

In the second step, for all droplet size classes larger than 40% of the maximum droplet size class for this experimental position, the values of the effective cross sectional area are obtained as values of the linear trend line. Therefore, there is an overlap of the size class ranges used for computing the trend line and those whose probe volume cross-section areas are calculated using the trend line. Once the effective cross-sectional area probe volume is corrected, the number density is corrected correspondingly. Then, the moment sets of droplet size and velocities are computed, which in turn are used to calculate the initial weights (number densities), radii and velocities using the Wheeler algorithm [136]. In the present study, the spray distribution is approximated by a three-node closure, which is proven to be accurate in previous studies [48, 49, 191, 202]. The three-node approximation of NDF implies that the required number of moments is 12 (3 each: weights, droplet radii, axial velocities, radial velocities). The same procedure is followed at every radial position for the cross-section of 0.08 m. Figure 4.15 shows the experimental distribution of droplets and DQMOM approximation at 0.066 m from the center of the spray for 80 kg/h water flow rate. The problem of negative moments is handled by employing the adaptive Wheeler algorithm [208].

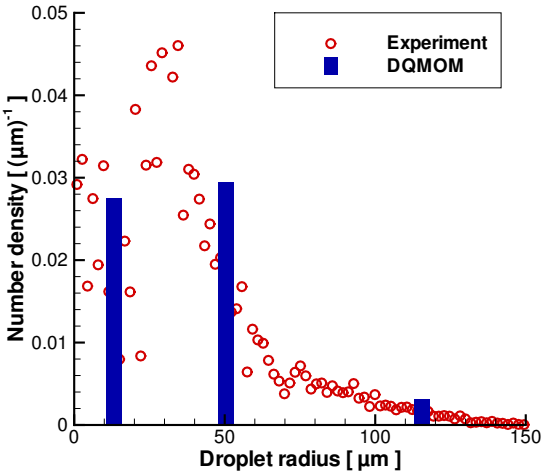

Fig. 4.15: Experimental and DQMOM approximation of droplet number density for a water spray.

The DDM simulation are carried out only for water spray in two-dimensional configuration by Humza [68]. In his work, the same experimental data is used to generate a system of parcels for DDM, where the properties of the k^{th} parcel are denoted by $(x_k, r_k, u_k, v_k, m_k)$ for the present two-dimensional configuration. The liquid mass of k^{th} parcel is computed assuming the spherical symmetry of the droplets, i.e.,

$$m_k = \sum_{i=1}^{N} \frac{4}{3}\pi\rho_l r_i^3, \tag{4.3}$$

where N refers to the number of droplets in the parcel. The number of parcels for the inflow rate of 80 kg/h is 3,704 and for 120 kg/h, it is 3,464. A non-equidistant rectangular grid with 7,878 grid points (78 in radial and 101 in axial direction, respectively) is used [68].

4.2.3 Results and Discussion

At first the implementation of maximum entropy (ME) method for the calculation of evaporative flux is studied. Fig. 4.16 shows the computed NDF at radial distance of 64.5 mm from the center and 0.08 m axial distance from nozzle for 80 kg/h liquid flow rate using ME method and its comparison with experiment, where a good agreement between the ME approximated NDF and experiment can be found. The evaporative flux computed using the weight ratio constraints, which are defined by Eqs. (2.33)–(2.34), for this position is found to be 0.39, where as with ME method it is 0.022 and

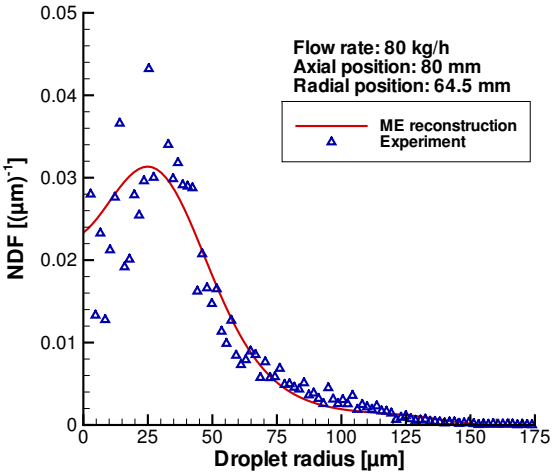

Fig. 4.16: Experimental and reconstructed NDF of 80 kg/h water spray at 64.5 mm from the center of the spray axis.

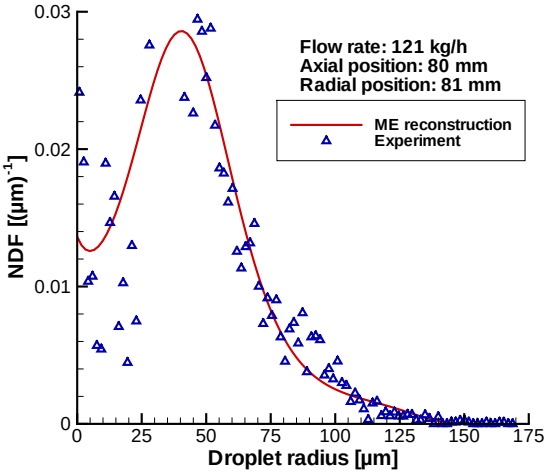

Fig. 4.17: Experimental and reconstructed NDF of 121 kg/h water spray at 81 mm from the center of the spray axis.

in experiment the same is about 0.03 (see Fig. 4.16). Similar observation is made with higher liquid flow rate as well, Fig. 4.17 shows the experimental and reconstructed NDF for water spray of 121 kg/h at 81 mm radial position from the center and 0.08 m away from the nozzle. Thus, the ME approach improves the DQMOM evaporative flux calculation procedure and it has excellent agreement with the experiment. Therefore, in the current study, the ME method is used for the ψ calculation in two-dimensional evaporating water and PVP/water spray flows.

In numerical simulation of water spray in two-dimensional configuration, average droplet properties such as mean droplet diameter, Sauter mean diameter and mean droplet velocity are computed using both the methods, i.e., DQMOM and DDM, and the simulation results are compared with the experiment at the cross sections of 0.12 m and 0.16 m away from the nozzle exit. Figure 4.18 shows the computed and experimental profiles of the Sauter mean diameter at cross sections of 0.12 m (left) and 0.16 m (right) downstream to the nozzle orifice for 80 kg/h. The DDM simulation results match quite well with the experiment at the center of the spray at 0.12 m away from the nozzle exit, but slightly underpredicts towards the periphery of the spray whereas good agreement is observed at 0.16 m cross section between DDM and experiment.

The DQMOM simulation results are in good agreement with experiment at 0.12 m downstream the nozzle exit, and it is closer to the experimental data at higher radial distance as well. Further downstream, at 0.16 m from the nozzle orifice (see right part of the Fig. 4.18), the DQMOM simulations reveal some scattering near the centerline,

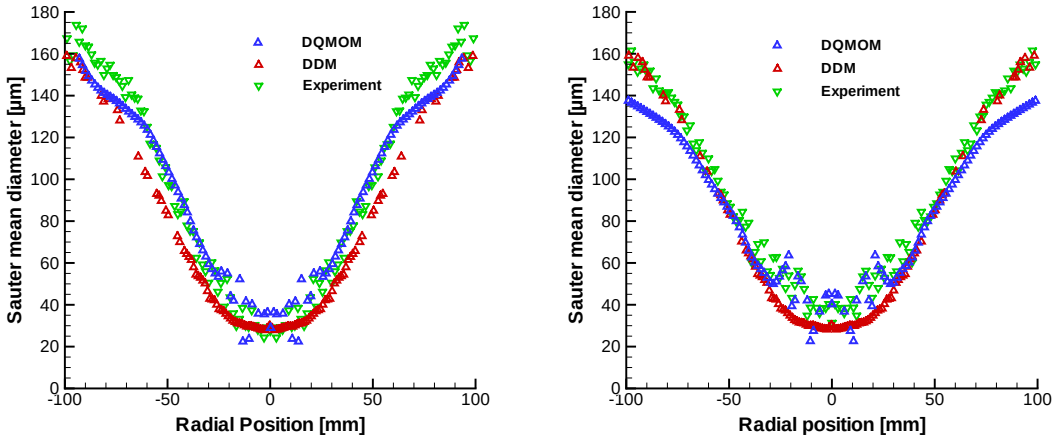

Fig. 4.18: Experimental and numerical profiles of the Sauter mean diameter of water spray with 80 kg/h liquid flow rate at the cross section of 0.12 m (left) and 0.16 m (right) distance from the nozzle exit.

while at higher radial distances, they underpredict the experimental results. This discrepancy may be the result of numerical scheme, which employs an explicit finite difference method to solve the transport equations of DQMOM; the results can be improved by implementing an implicit method. The post-processing of experimental data, which is explained in Subsection 4.2.2, may be the reason of the deviation, too.

For an elevated liquid inflow rate of 120 kg/h, the computed and experimental

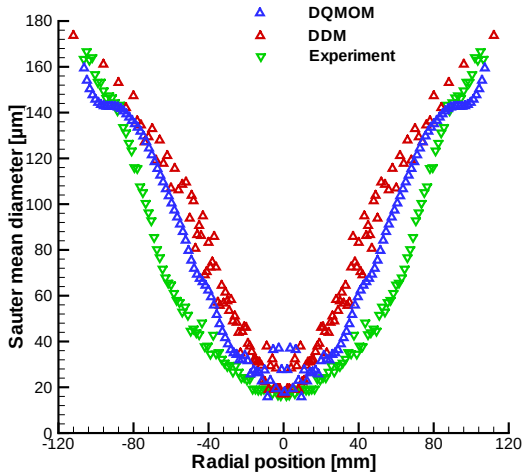

Fig. 4.19: Experimental and numerical profiles of the Sauter mean diameter at the cross section of 0.12 m distance from the nozzle exit for 120 kg/h.

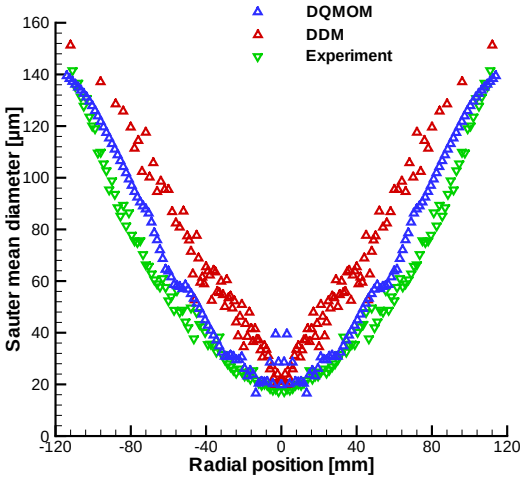

Fig. 4.20: Experimental and numerical profiles of the Sauter mean diameter at the cross section of 0.16 m distance from the nozzle exit for 120 kg/h.

profiles of Sauter mean diameter at cross sections of 0.12 m and 0.16 m away from the nozzle exit are shown in Figs. 4.19 and 4.20. An increased liquid flow rate causes a somewhat decreased droplet size: For a given liquid, increased mass flow rate leads to higher pressure drop in the atomizer, which decreases liquid sheet size and breakup length to yield smaller particles as can be seen when compared with Fig. 4.18.

At the cross section of 0.12 m, it can be seen that DQMOM performs better than the DDM results as DDM overpredicts the experimental values. The scattering behavior of DQMOM simulation results near the centerline is observed in this case, too. As the droplets move to the next cross section, a decrease in large size droplets is evident, which is predicted by both DQMOM and DDM. The results show that the DQMOM shows better agreement with experiment, while DDM predicts somewhat higher values than the experiment at corresponding radial positions [205].

The overall shape of a hollow cone spray is captured quite nicely by both methods, although some deviations are observed, particularly in DQMOM as compared to experimental profile. This is possibly due to the post-processing of the experimental data as explained in Subsection 4.2.2, which is done to correct the number frequency at every measuring position to rule out the fluctuations in the effective cross sectional area of the measuring volume for the larger droplet sizes [207]. This correction of experimental data is position dependent, whereas DQMOM and DDM results account for these corrections for the initial condition but not at positions further downstream. Another reason for the discrepancies in the DQMOM results may be due to the fact that the spray equations are not yet fully coupled to the gas phase.

Comparing the maximum values of the Sauter mean diameter at the two cross sections displayed in Figs. 4.18, 4.19 and 4.20, a decrease in large size droplets is observed as the droplets move away from the nozzle. Even though the process of evaporation is considered in the present models, the major reason for the decrease in droplet size may be attributed to the influence of drag force applied by the surrounding gas, because significant evaporation may not occur at the present room temperature condition. This decrease is more evident in the large droplet size region, where the dynamic interaction of droplet with surrounding gas dominates, as observed in profiles of mean droplet velocity (see Figs. 4.23 and 4.24).

Besides the Sauter mean diameter, in many technical applications such as particle size analysis of powder sampling in food and pharmaceutical industries, the mean droplet diameter is an important physical quantity [201]. Radial profiles of the mean droplet diameter compared with experiment are shown in Fig. 4.21 for 80 kg/h at 0.12 m (left) and 0.16 m (right) distance away from nozzle. DDM results are in very good agreement with the experiment. A slight decrease in the mean droplet diameter is observed as the droplets move away from nozzle indicating some mass transfer from liquid to gas, which is attributable to gas–liquid interactions. The DQMOM results are in excellent agreement with experiment at the cross section of 0.12 m near the centerline, and DQMOM results show better agreement than DDM results (see left part of Fig. 4.21). At 75 mm radial position, the DQMOM results are below experimental values, which may stem from the explicit finite difference technique. At the cross section of 0.16 m, a good agreement is observed between DQMOM and experiment near the axis of symmetry, even though some scattering behavior is found (see right

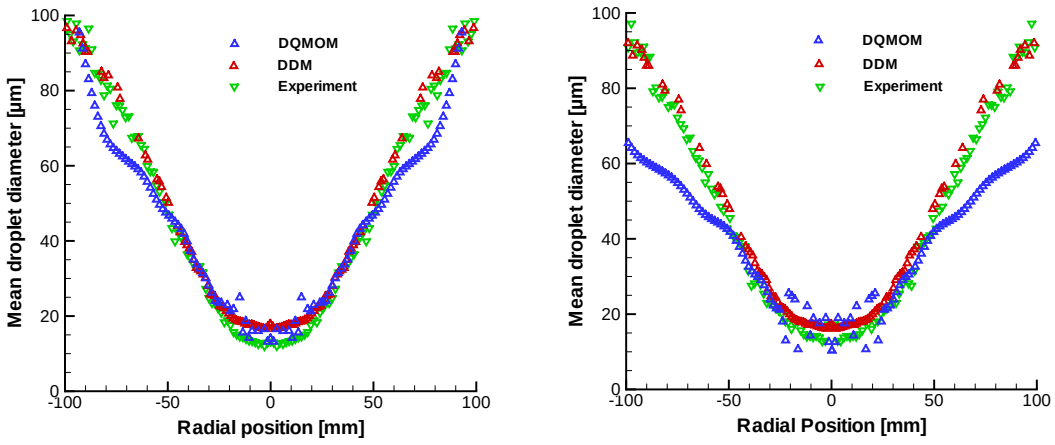

Fig. 4.21: Experimental and numerical profiles of the mean droplet diameter of water spray with 80 kg/h liquid flow rate at the cross section of 0.12 m (left) and 0.16 m (right) distance from the nozzle exit.

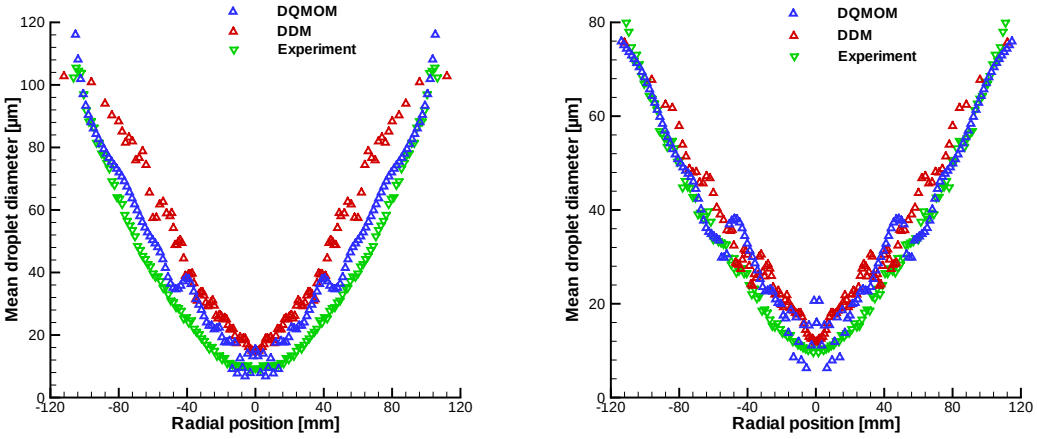

Fig. 4.22: Experimental and numerical profiles of the mean droplet diameter of water spray with 120 kg/h liquid flow rate at the cross section of 0.12 m (left) and 0.16 m (right) distance from the nozzle exit.

side of Fig. 4.21).

In Fig. 4.21, deviations from the experiment occur in the large droplet size region, which is due to the fact that the numerical technique captures the distribution function globally, and there could be some local discrepancies as well. This may be improved by solving the gas phase equations for DQMOM, which is not yet done in the present study, where the inlet gas flow properties are used to calculate the source terms for transport equations for DQMOM [209].

Figure 4.22 shows the computed and experimental profiles of the mean droplet diameter at cross sections of 0.12 m (left) and 0.16 m (right) away from the nozzle exit for liquid inflow rate of 120 kg/h. Similar to Sauter mean diameter, elevated liquid flow rate leads to somewhat decreased droplet size (compare Fig. 4.22 with 4.21) . At 0.12 m away from the nozzle exit, both DDM and DQMOM agree well with each other near the centerline, where they show relatively higher values than the experiment. At the radial positions away from the centerline, DQMOM is in good agreement with the experiment, and it is better than the DDM results. As the droplets move away from the nozzle exit, a decrease in size can be observed at the cross section of 0.16 m away from the the nozzle exit (see right part of the Fig. 4.22), which is similar to the case of liquid flow rate of 80 kg/h. Near the centerline at 0.16 m away from the nozzle exit, both DQMOM and DDM show the same behavior and predict slightly higher values than experiment. At higher radial positions, DDM values are higher compared to DQMOM and experiment, whereas DQMOM coincides with the experimental data.

In Figs. 4.23 and 4.24, the radial profiles of mean droplet velocity are displayed at different cross sections. It can be seen that the droplet velocity is higher for larger

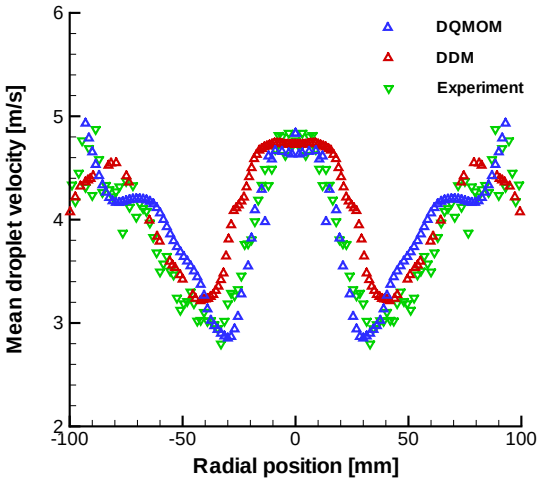

Fig. 4.23: Experimental and numerical profiles of the mean droplet velocity at the cross section of 0.12 m distance from the nozzle exit.

droplets as anticipated. Interestingly, the small size droplets near the axis of symmetry also move at a higher velocity as observed in the experiment and thus causing the velocity profile bimodal, which is predicted quite nicely by both models.

A closer look reveals that the width of the jet is captured by the DQMOM, whereas the DDM predicts somewhat broader profiles with a lower maximum value at the centerline. At the spray edge, a judgement of the numerical methods is difficult, since the

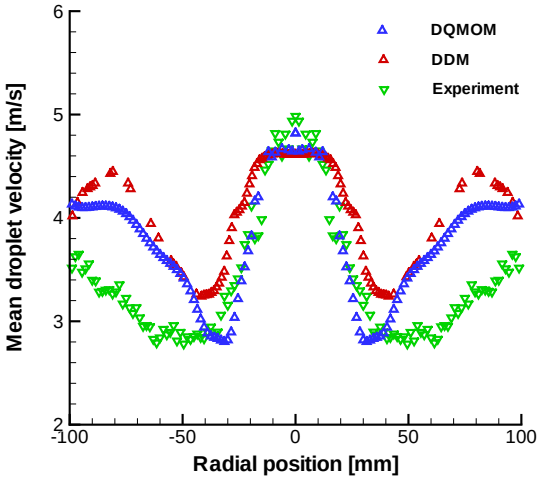

Fig. 4.24: Experimental and numerical profiles of the mean droplet velocity at the cross section of 0.16 m distance from the nozzle exit.

experimental data are somewhat spread at 0.12 m from the nozzle exit. At 0.16 m, the slopes of the numerical results deviate from the experimental data, particularly in large size droplets region where the effective cross sectional area shows strong fluctuations in experiment as shown in Fig. 4.14. This implies that the post-processing of experimental data plays an important role in the corrections of number density and thereby the droplet properties [207]. Comparing the velocity profiles at the two different cross sections, it is seen that the velocity decreases as droplets move away from the nozzle. This is because the droplets are strongly decelerated by the dynamic interaction with the surrounding gas. The gas around the spray stagnates and is driven into motion only due to the spray entrainment. The gas motion driven by the spray arises at the expense that the droplet loses momentum.

The droplet properties are predicted quite well by the present simulations, which confirms their applicability for spray flows. There are some deviations between simulation and experimental results, which are attributable to the post-processing of the experimental data as mentioned before. In case of DDM, neglecting droplet–droplet interactions may need reconsideration. For DQMOM, the improved numerical scheme and the simultaneous solution of the gas phase equations may improve the simulation results.

Based on these simulation results and comparison with the experiment, it can be concluded that the DQMOM is a robust method, which can predict the spray flows accurately. This led to the implementation of DQMOM to study bi-component evaporating spray, i.e., PVP/water spray flow in two dimensions. In order to perform simulations of PVP/water spray flows, the predictability and efficiency of developed bi-component droplet evaporation and solid layer formation model (see Subsection 2.4.1.2) needs to be verified under different drying conditions. The next section presents the numerical simulation of single bi-component droplet evaporation and solid layer development, and comparison of simulation results with experiment.

4.3 Single Bi-component Droplet Evaporation and Solid Layer Formation

The model presented in Subsection 2.4.1.2 to predict the evaporation and solid layer formation for PVP/water droplet and mannitol/water droplet is simulated with different conditions such as initial solute mass fraction, gas temperature and velocity, relative humidity, initial droplet size etc. In the next subsections, the vapor-liquid equilibrium calculation followed by non-ideality effect caused by the solute (PVP or mannitol) presence on the droplet heating and evaporation rate is explained. Finally, the single droplet evaporation and solid layer development results are presented.

4.3.1 Vapor-Liquid Equilibrium

The vapor-liquid equilibrium for the evaporating component i is needed for the calculation of Spalding's mass transfer number, $B_{M,1}$, cf. Eq. (2.54), for both PVP/water and mannitol/water droplet evaporation and solid layer development cases, in which the mass fraction, $Y_{1,\mathrm{s}}$, of the evaporating component appears; this mass fraction is calculated through the mole fraction, X_i, $i = 1$, of the evaporating component water, in terms of the activity coefficient

$$X_i = \frac{p_{\mathrm{vap},i}}{p_{\mathrm{m}}} \gamma_i X_{\mathrm{L},i}, \tag{4.4}$$

where $p_{\mathrm{vap},1}$ is the vapor pressure of pure water and p_{m} is the total mixture pressure, which is equal to the ambient gas pressure, and in the present study it equals the atmospheric pressure. Here, $X_{\mathrm{L},i}$ is the mole fraction of evaporating component i in liquid phase, and γ_i is the activity coefficient of evaporating component i, which is calculated through equation given as,

$$\gamma_i = \frac{a_{\mathrm{w}} Y_{\mathrm{L},i}}{X_{\mathrm{L},i}}. \tag{4.5}$$

Here a_{w} is the water activity, $Y_{\mathrm{L},i}$ with $i = 1$, is the water mass fraction within the droplet. The calculation of water activity coefficient is described in next subsection.

4.3.2 Non-ideal Liquid Mixture

The presence of polymer or mannitol with water leads to non-ideal liquid behavior, which must be accounted for in calculating the mole fraction of water vapor at the droplet surface. In this work, the liquid mixture is treated as non-ideal by determining the influence of individual components on each other through their activity coefficients. The universal functional activity coefficient (UNIFAC) method is the accurate and most extensively used procedure [210], which estimates the activity coefficient as a sum of combinatorial and residual terms. This method, however, cannot be applied for polymer solutions as they have significant difference in accessible volume for a molecule in the solution [211].

The work of Oishi and Prausnitz [211] extended UNIFAC method to account for such differences in accessible volume by introducing a free-volume term, which enabled the UNIFAC approach to be applied to polymer solution systems. However, it is proven that their model fails for aqueous polymer systems because of the inadequacy of its free-volume term [212]. In the current study, the activity coefficient of water in PVP/water solution is computed using the UNIFAC-van der Waals-Free Volume method known as UNIFAC-vdW-FV method [212], which accounts for the free-volume

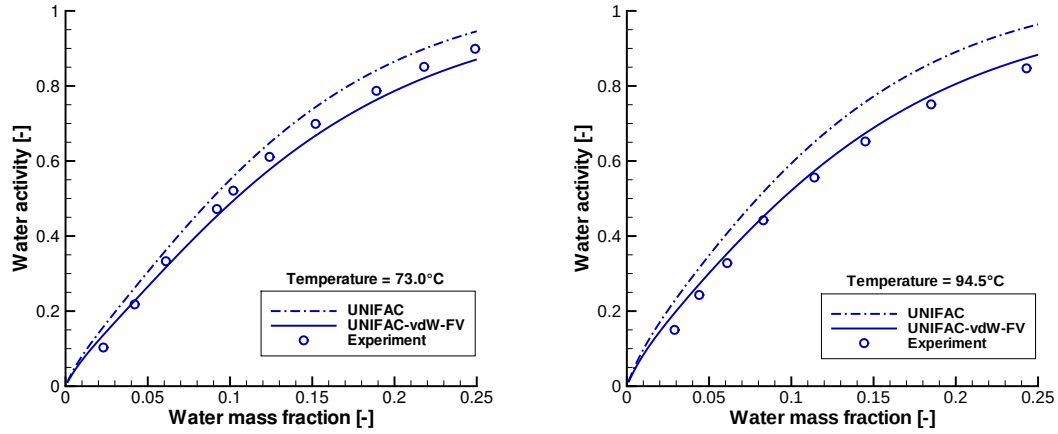

Fig. 4.25: Numerical and experimental [214] results of water activity (a_w) in PVP/water solution at 73.0 °C (left) and 94.5 °C (right).

effect in aqueous polymer solutions. In case of mannitol/water droplet evaporation study, the activity coefficient of water is calculated using the analytical solution of groups (ASOG) contribution method [213], as it is proven to perform better than the UNIFAC method [213].

Before implementation of the UNIFAC-vdW-FV method into the current PVP/water droplet code, it has been verified by comparing the water activity (a_w) computed using the UNIFAC method [210]. Results from these two methods are compared with

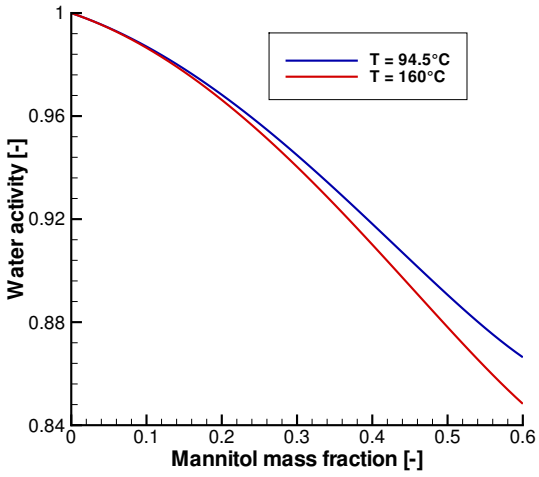

Fig. 4.26: Numerical results of water activity (a_w) in mannitol/water solution at 94.5 °C and 160 °C.

experimental results [214]. Molecular properties data such as van der Waals volume and radii for PVP are taken from Bondi [215], Danner and High [216], and the interaction parameters of individual molecules required in the UNIFAC-vdW-FV method are taken from Daubert and Danner [217]. In Fig. 4.25, variation of the weight based water activity with water mass fraction in PVP/water solution is exemplarily shown at a temperature of 73.0 °C (left) and 94.5 °C (right), respectively.

The results reveal that the UNIFAC-vdW-FV method improves the UNIFAC method results, and the UNIFAC-vdW-FV predictions are in excellent agreement with the experimental data. Therefore, in the current study, the UNIFAC-vdW-FV method is implemented to compute water activity in PVP/water solution.

The change in water activity with mannitol mass fraction in mannitol/water solutions at a temperature of 94.5 °C and at 160 °C computed using ASOG method is displayed in Fig. 4.26. The results show that the water activity in mannitol/water solution decreases not only with increased mannitol mass fraction but also with increased liquid temperature.

The effect of non-ideality through activity coefficient on the reduction of vapor pressure of water in PVP/water solution for different mass fractions of PVP dissolved in water at different temperatures is shown in Fig. 4.27. For the sake of comparison, ideal condition is also shown where the activity coefficient always remains at unity so that the vapor pressure is independent of solute mass fraction. It can be clearly observed that the liquid mixture strongly deviates from ideal behavior and the deviation increases with the increasing PVP mass fraction in water.

Figure 4.28 shows the effect of non-ideality through PVP presence in PVP/water

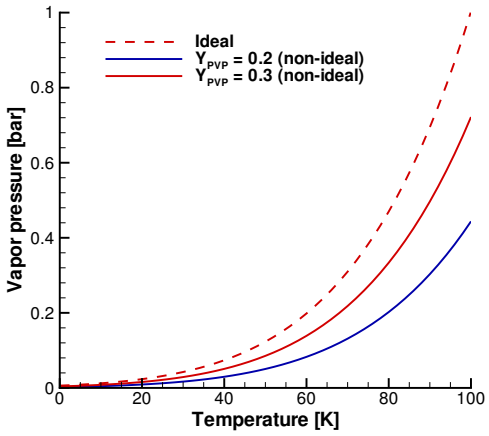

Fig. 4.27: Effect of non-ideality on the vapor pressure of water at different temperatures.

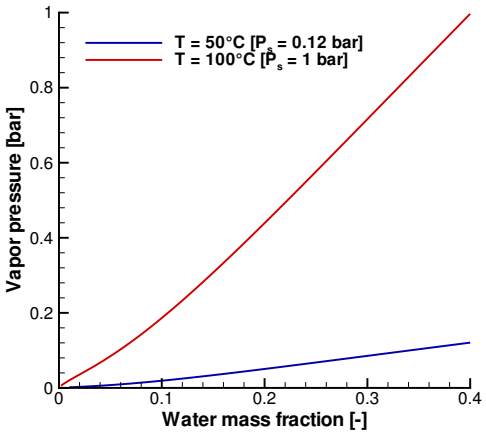

Fig. 4.28: Variation of vapor pressure of water with water mass fraction in PVP/water solution.

solution on the water vapor pressure at 50 °C and 100 °C of liquid temperature. The vapor pressure of pure water at 50 °C is about 0.12 bar whereas at 100 °C it is 1 bar. An increase in water mass fraction increases the vapor pressure and it equals the pure water pressure when the water mass fraction is above 0.4. Thus, it infers that the role of water activity coefficient is important when the water mass fraction within the droplet falls below 0.4 at 50 °C and 100 °C, which occurs in the present simulations.

4.3.3 Results and Discussion

The simulation of evaporation and solid layer development of single droplet containing PVP or mannitol in water is carried out under various drying conditions such as surrounding gas temperature, gas velocity, and relative humidity to investigate their effect on drying characteristics. The effect of the initial solute (PVP or mannitol) mass fraction on the final particle characteristics is also studied. The droplet is assumed to be spherical during the entire evaporation and drying process. The simulations are also carried out with rapid mixing model (RMM), which is a simple model based on the assumptions that the liquid mixture inside the droplet is always homogeneous and infinity conductivity within the droplet thus the droplet is at uniform temperature at every time. The governing equations of RMM are presented in Subsection 2.4.1.2.

The thermal properties of PVP and mannitol are taken from Dakroury *et al.* [220], and mass diffusivity of PVP in water is obtained from Metaxiotou and Nychas [221], whereas the mass diffusivity of mannitol in water is taken from Grigoriev and Mey-

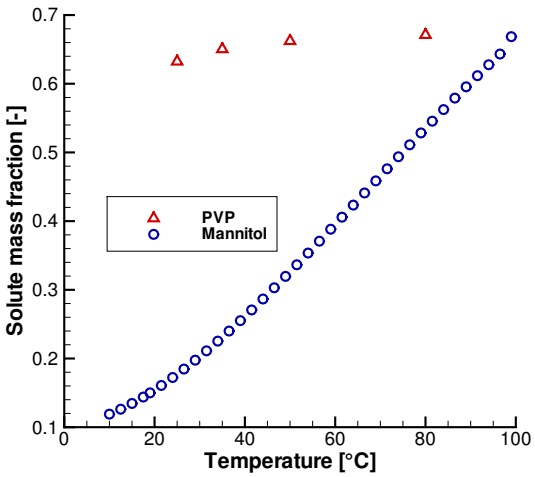

Fig. 4.29: Experimental data of PVP [218] and mannitol [219] saturation solubility in water.

Tab. 4.3: Experimental drying conditions

Drying condition	Values
Initial solute mass fraction	0.075, 0.05 and 0.15
Initial droplet radius	70 μm
Initial droplet temperature	20 and 70 °C
Gas temperature	60, 67, 95, 100, 160 and 210 °C
Gas velocity	0.05, 0.65 and 10 m/s
Relative humidity (R.H.)	0.5 1.0, 2.0 and 30%

likhov [222]. The critical temperature and pressure of PVP and mannitol are taken from Daubert and Danner [217]. The vapor diffusion coefficient through the solid layer of PVP or mannitol, D_s, and solid thermal conductivity, k_s are not available in literature, therefore, they are computed similar to the work of Nesic and Vodnik [151]. The physical and thermal properties in the film are estimated at the reference composition using the 1/3 rule [223]. The PVP/water and mannitol/water solution physical and thermal properties are computed with the standard rules of mixing. The variation of saturation solubility of PVP in water and mannitol in water with temperature is taken from measurements [218, 219], and it is shown in Fig. 4.29. The solid layer at the droplet surface is presumed to develop when the PVP mass fraction at the droplet surface reaches 20% above its saturation solubility limit, and in the case of mannitol, it is assumed that the crust and solid layer formation begins when the mannitol mass fraction reaches 0.9, which is much higher than the saturation solubility, in order to avoid re-dissolution of solid layer with increased temperature as it shows large variation of solubility with temperature, see Fig. 4.29.

The numerical results presented refer to a droplet of initial radius 70 μm at 20 °C containing 0.15 PVP or mannitol initial mass fraction subjected to air with 0.5% relative humidity (R.H.) flowing at 0.65 m/s with 100 °C initial gas temperature [172]. The various drying conditions for numerical simulations taken from the experimental study of Littringer *et al.* [21] and Sedelmayer *et al.* [224], are listed in Tab. 4.3 and numerical results are compared with available experimental data [21, 224].

Figure 4.30 shows the change in mannitol/water droplet mass and temperature with time for the above conditions and for increased initial gas velocity ($U_g = 10$ m/s). Initially, there is no significant increase in droplet temperature, and droplet mass reduces due to continuous water evaporation. After an initial heating period, the droplet temperature rises very quickly indicating the formation of solid layer whereupon the rate of evaporation is reduced due to added resistance coming from solid layer, which is reflected in the droplet mass profile. The higher gas flow rate increases convection and

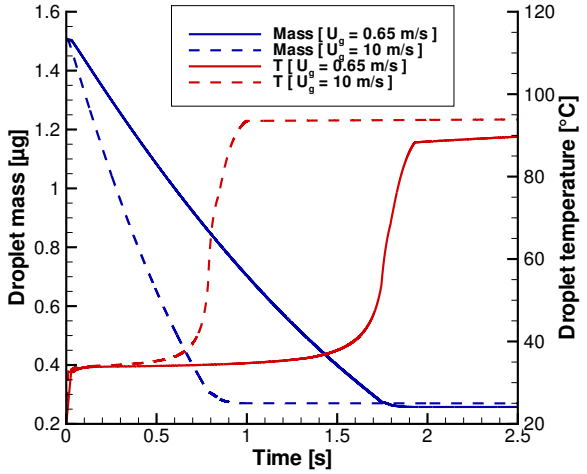

Fig. 4.30: Effect of gas velocity on the evolution of mass and temperature of a mannitol/water droplet.

thereby the water evaporation, hence there is quicker development of the solid layer. The solid layer forms in about 1.7 s with $U_g = 0.65$ m/s, whereas with $U_g = 10$ m/s, the solid layer forms in about 0.75 s. A closer look reveals that there is higher droplet mass at any given time after solid layer formation when compared with lower gas velocity situation, which means that increased gas velocity would lead to larger particle and the porosity, defined as the ratio of the volume occupied by water at the instance of

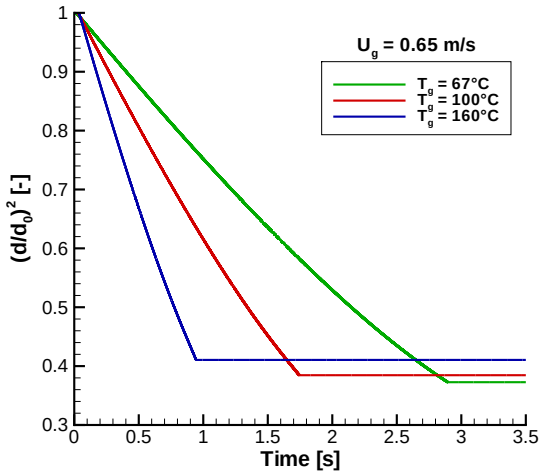

Fig. 4.31: Effect of elevated gas temperature on the surface area of a mannitol/water droplet.

solid layer formation over that of the whole particle volume, would be higher in case of increased gas velocity (see Fig. 4.33).

Figure 4.31 shows the effect of initial gas temperature on the temporal change of the dimensionless surface area of a mannitol/water droplet. Elevated gas temperature leads to higher energy transfer from the gas to the droplet, and thereby, an increase in the rate of droplet evaporation and drying. The surface area continuously decreases due to water evaporation until the beginning of solid layer formation whereupon particle size remains constant, which is reflected in Fig. 4.31.

The higher the gas temperature the quicker the time taken for the solid layer formation: In case of 67 °C the solid layer develops in about 2.9 s and with 100 °C the solid layer forms in 1.7 s, whereas with 160 °C, the same is observed in about 0.9 s. There is larger surface area at the time of solid layer formation with higher gas temperature, which means that elevated gas temperature would give larger particles towards the end of the drying process (see Fig. 4.33).

The effect of gas temperature on the development of mannitol mass fraction profiles inside the droplet of initial radius 70 µm subjected to dry air with 0.5% R.H., flowing at 0.65 m/s with temperatures of 67, 100 and 160 °C is shown in Fig. 4.32 at 0.5 s (left) and at 0.9 s (right), respectively. Initially, the droplet interior has a homogenous mannitol mass fraction distribution of 0.15 (not shown here) and with time, there is development of mannitol mass fraction gradients inside the droplet, and the droplet size reduces due to continuous water evaporation. For 100 °C initial gas temperature, the droplet radius is 62 µm at 0.5 s whereas at 0.9 s it reduces to 56 µm, which is seen in Fig. 4.32, respectively. The increased initial gas temperature yields higher mass fraction gradients inside the droplet mainly due to the decreased activity coefficient of

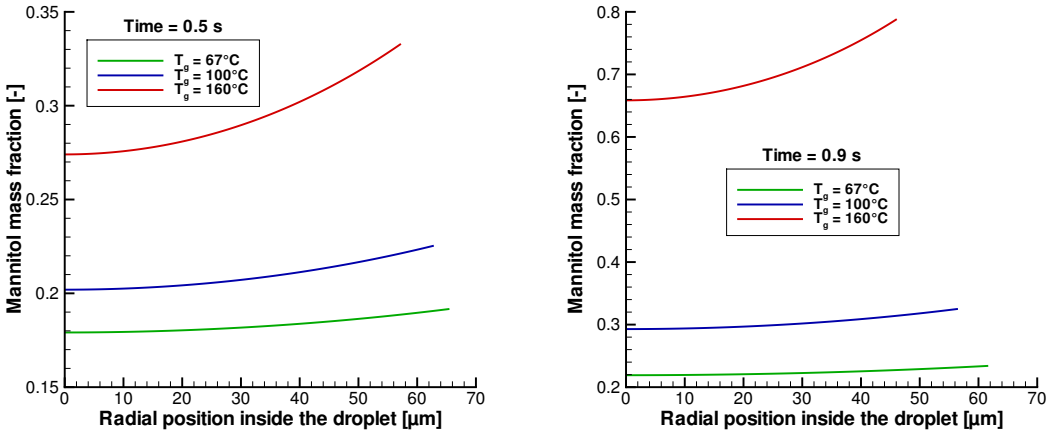

Fig. 4.32: Effect of gas temperature on the temporal development of mannitol mass fraction inside the droplet at 0.5 s (left) and 0.9 s (right).

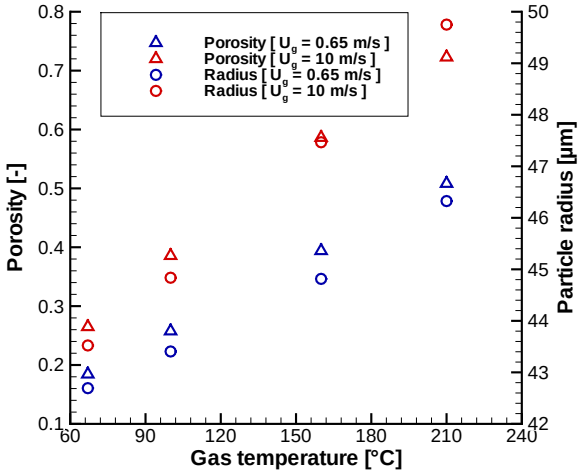

Fig. 4.33: Effect of gas velocity and temperature on porosity and final particle size of mannitol/water droplet.

water in mannitol (see Fig. 4.26) and enhanced heat transfer. The activity coefficient decreases not only with increase in temperature but also with mannitol mass fraction, which is quite clearly seen at later times, i.e., 0.9 s shown in right part of Fig. 4.32.

The effect of elevated gas velocity and temperature on the final particle porosity and particle radius is shown in Fig. 4.33. The porosity increases with higher gas temperature and velocity because of quicker solid layer formation, thereby yielding larger particles. The computed porosity of mannitol particle with 160 °C gas temperature and 0.65 m/s gas velocity is 0.39 and the corresponding value in experiment is found to be 0.41 [21]. The final particle radius is reported as 42 µm in experiments [21], which can be compared to the corresponding computed value of 44.8 µm, showing a very good agreement.

In experiments [21], it is reported that increased gas temperature leads to less porous particle with shriveled or non-spherical shape as seen in Fig. 4.34, which shows the the scanning electron microscope (SEM) images of the mannitol samples spray dried under different drying temperatures. For the outlet temperature of 70 °C, a spherical mannitol particle is obtained, see Fig. 4.34(a). For the higher outlet temperature of 100 °C the particle shape changes from spherical to a 'raisin like' structure, cf. Fig. 4.34(b), that may occur due to inflation of a drying shell and this transition is observed at 90 °C, see Fig. 4.34(c). Higher temperatures lead to faster evaporation of the water, leading to less time to form a stable structure on the droplets surface. From the high porosity in combination with cuts of spray dried mannitol particles in previous studies [21], the formation of a particle with an outer shell is evident [225].

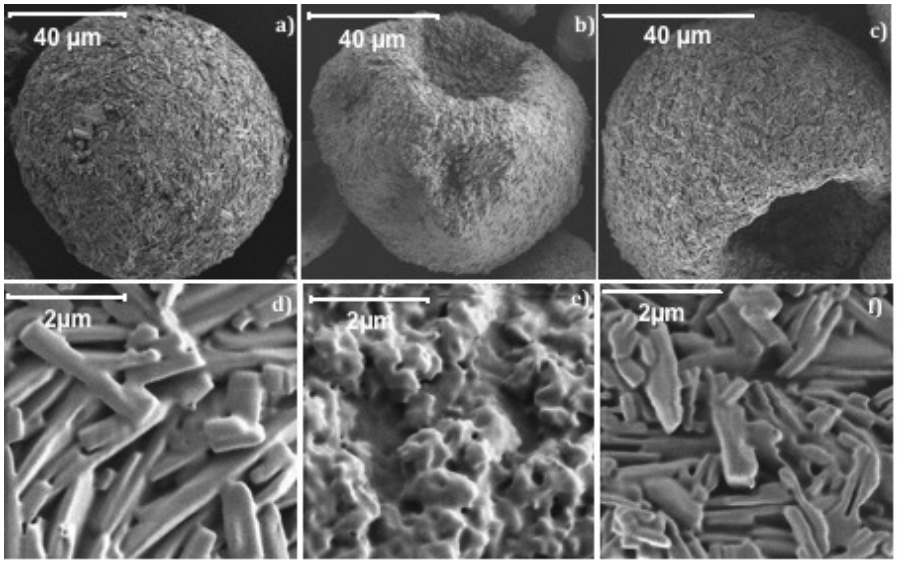

Fig. 4.34: SEM images of mannitol samples spray dried at 70 °C (a), 100 °C (b) and 90 °C (c). Zoomed images of the surface structures of these particles at 70 °C (d), 100 °C (e) and 90 °C (f) [225].

This shell formation is in good accordance with the simulations performed so far.

The particle surface consists of small, needle shaped structures in case of low drying temperatures as shown in Fig. 4.34(d), and smaller, non-needle shaped structures for higher drying temperatures, cf. Fig. 4.34(e), and the shift from needle shape to non-needle structures is seen in Fig. 4.34(f). The increased gas temperature not only effects the final particle shape but also internal structure [225]. In computations, the change in particle shape is not accounted for, and it is assumed to be spherical throughout the evaporation and drying period, therefore, the present numerical results show increase in porosity with temperature as anticipated, see Fig. 4.33. This behavior will change when the final drying step is added to the present model, and if non-spherical particle formation will be considered.

Figure 4.35 shows the effect of gas temperatures of 60 °C and 95 °C and relative humidity of 1% R.H. (left) and 30% R.H. (right), respectively, on the droplet surface area and comparison with experimental data. The experiments are carried out by Sedelmayer *et al.* [224] at the University of Hamburg in an acoustic levitator. The simulation results show excellent agreement with the experiment. The droplet surface area continuously decreases due to water evaporation until a critical value where the solid layer formation starts, which is quite nicely predicted by the simulation. Increased temperature increases the evaporation rate and thereby quicker solid layer formation as seen in left part of Fig. 4.35, whereas increased humidity increases the solid layer formation time, i.e., at 60 °C at 1% R.H. the solid layer forms in about 65 s and with

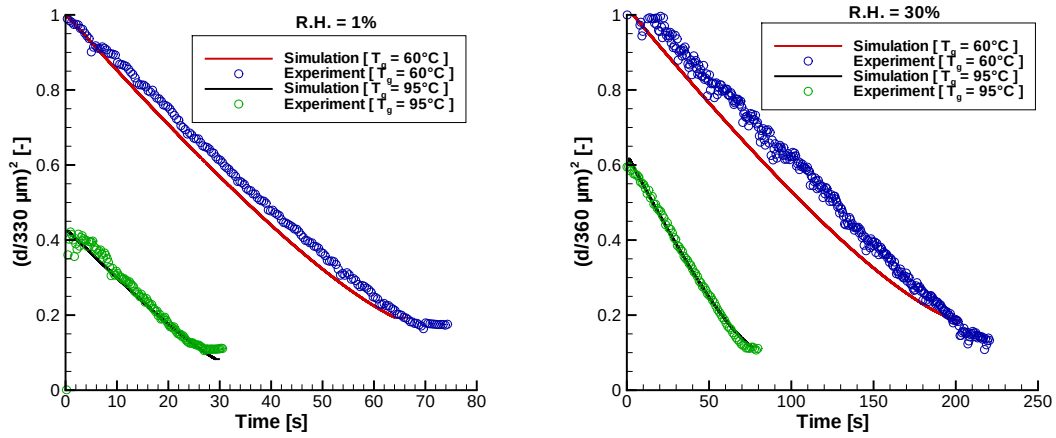

Fig. 4.35: Effect of gas temperatures of 60 °C and 95 °C and relative humidity of 1% R.H. (left) and 30% R.H. (right) on the droplet surface area.

30% R.H. the same observed in about 205 s, see right part of Fig. 4.35. The profiles of the normalized droplet surface, $(d/d_0)^2$, shown in the Fig. 4.35, reveal that the droplet evaporation rate prior to solid layer formation in the present case deviates from the linear decrease with time as would be expected from the classical d^2 law, where a constant evaporation constant is assumed.

These experiments are carried out with different initial droplet radius for every experiment, and Tab. 4.4 gives the initial droplet radii (R_0) and particle size at the time of solid layer formation (t_s) in every experiment and its corresponding computed value from simulation.

The comparison between rapid mixing model (RMM) and the present model is given in Fig. 4.36, which shows the time evolution of mannitol/water droplet surface area for initial droplet radius of 70 µm at 20 °C temperature and subjected to hot air of 160 °C with 0.5% R.H. and flowing at 0.65 m/s. Even though there is little difference between RMM and the present approach during the initial time period, however, in the later

Tab. 4.4: Experiment vs simulation

T_g [°C]	R.H. [%]	R_0 [µm]	Particle radius at t_s [µm]	
			Simulation	Experiment
60	1.0	330	145.1	147.9
	30.0	360	155.2	155.1
95	1.0	215	95.0	109.4
	30.0	280	122.5	121.4

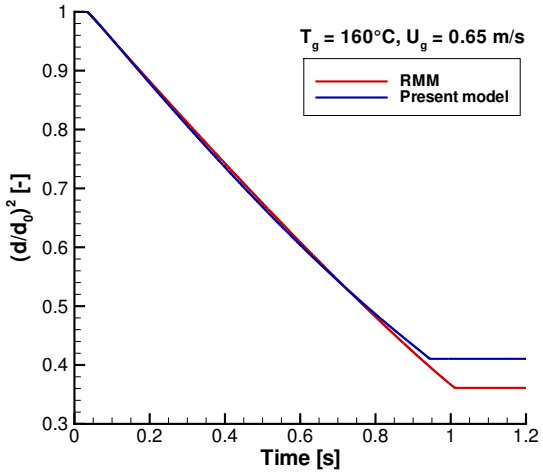

Fig. 4.36: Time evolution of mannitol/water droplet surface area computed by present model and RMM.

time period RMM overpredicts the decrease in droplet surface and thereby the time of the solid layer formation caused by the fact that the assumption of homogeneous liquid mixture within the droplet. This assumption leads to more water to be evaporated, which increases the solute mass fraction to the critical value so that the formation of solid layer begins.

The effect of initial droplet temperatures of 20 °C and 70 °C on the evaporation

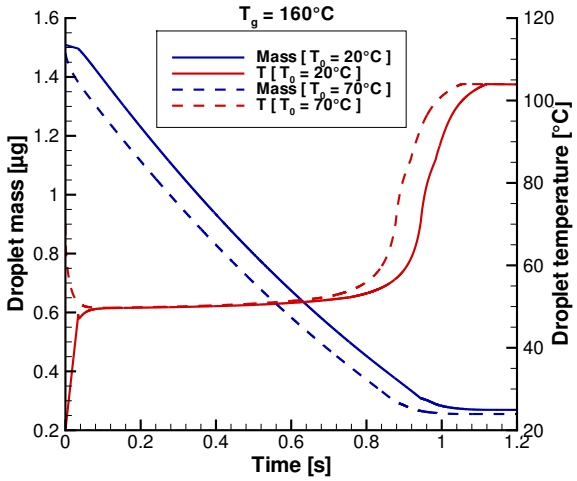

Fig. 4.37: Effect of initial droplet temperature on the evaporation rate of mannitol/water droplet.

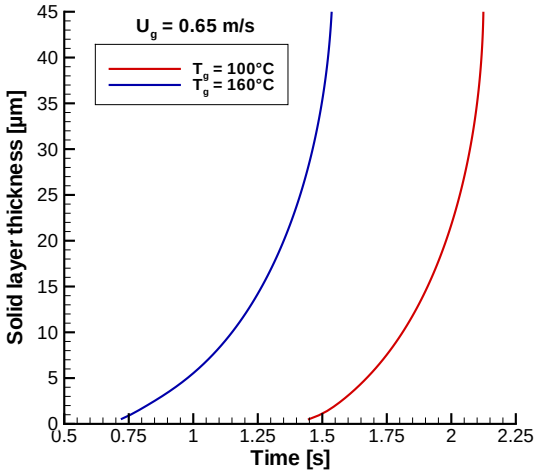

Fig. 4.38: Effect of gas temperature on solid layer thickness inside the PVP/water droplet.

rate is shown in Fig. 4.37. In both the cases, the initial droplet radius is 70 µm, and it is subjected to hot air flowing at 0.65 m/s with 160 °C. The droplet with 20 °C initial temperature quickly raises to an equilibrium temperature, which is most often equal to the wet bulb temperature, whereupon no significant rise in temperature is found. Whereas with 70 °C, the wet bulb temperature for the gas temperature of 160 °C and 0.5% R.H., is lower than the initial droplet temperature (70 °C), so the droplet temperature decreases until it equals the wet bulb temperature, and remains almost constant in further development. Similarly the droplet evaporation rate is higher in this initial period, and it is reflected in the reduction of droplet mass as seen in Fig. 4.37. In the later time period, the final particle temperature is same, and it is equal to 105 °C.

Similar trends are observed for PVP/water evaporation and solid layer formation. The effect of elevated gas temperature on the temporal development of solid layer thickness in PVP/water droplet is shown in Fig. 4.38 for the same conditions that are studied for mannitol/water. Increased gas temperature of $T_g = 160$ °C leads to higher energy transfer and earlier molecular entanglements of PVP and solid layer formation, with 100 °C the solid layer forms in about 1.4 s whereas with 160 °C, the same is observed in 0.7 s, see Fig. 4.38.

Comparison of PVP/water droplet evaporation and solid layer formation with that of mannitol/water under the same drying conditions reveals that the solid layer forms quicker in case of PVP/water (in about 1.5 s with 100 °C, see Fig. 4.38) than mannitol/water (about 1.7 s with 100 °C, see Fig. 4.30). This is due to the fact that the

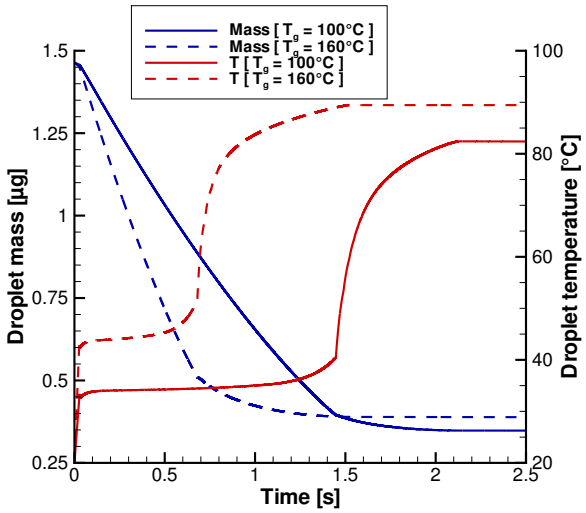

Fig. 4.39: Effect of gas temperature on the droplet mass and temperature.

required solute mass fraction for initiation of the solid layer formation is less in case of PVP (about 0.78 at 100 °C, see Fig. 4.29) compared to mannitol, which is fixed to 0.9.

Figure 4.39 shows the effect of gas temperature on the temporal evolution of PVP/water droplet mass and temperature when the droplet is subjected to 100 °C and 160 °C gas temperatures. Elevated temperature leads to higher energy transfer from the gas to the droplet, and thereby, an increase in the rate of droplet evaporation and drying, which is reflected in Fig. 4.39. The higher the gas temperature the quicker the time taken to see molecular entanglement leading to solid layer formation: in case of 160 °C, the solid layer develops in about 0.7 s whereas with 100 °C , the same is observed in about 1.5 s, which is in agreement with Fig. 4.38. This means that an increase in gas temperature would give larger particles towards the end of the drying process.

Figure 4.40 shows the temporal development of PVP mass fraction profiles inside the PVP/water droplet of initial radius 70 µm subjected to hot air flowing at 0.65 m/s with 100 °C temperature and no humidity, i.e., dry air (left) and with 5% R.H. (right), respectively. Initially, the droplet has a homogenous PVP mass fraction of 0.15 and with time the droplet size decreases, and there is development of PVP mass fraction gradients inside the droplet due to continuous water evaporation, which can be seen at later times in both the figures. The PVP mass fraction at the droplet surface reaches the value of 0.78 in about 1.4 s with dry air, as seen left side of Fig. 4.40, which is equivalent to 20% above the saturation solubility whereas the same is achieved after 1.8 s with 5% R.H., see right part of Fig. 4.40. This indicates that the increase in humidity prolongs the drying period because of the reduced driving force for water

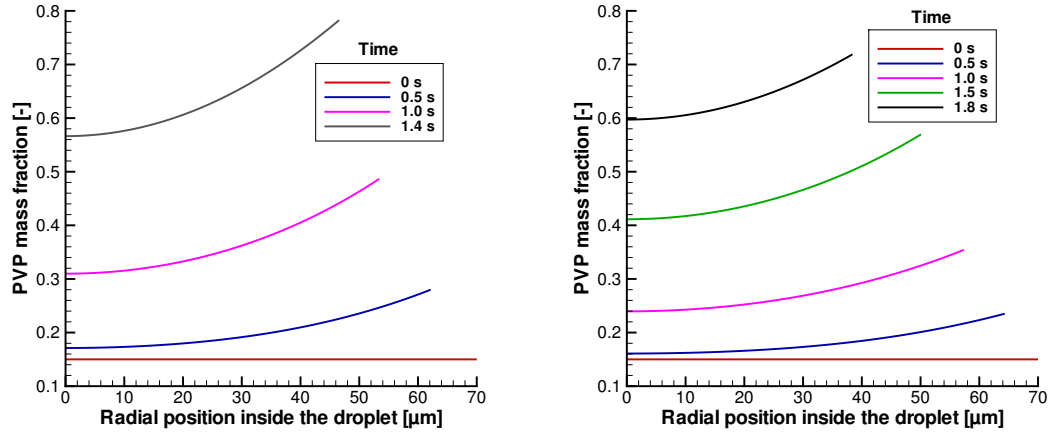

Fig. 4.40: Temporal development of PVP mass fraction profiles inside the droplet subjected to dry air (left) and hot air with 5% R.H (right).

evaporation, cf. Eq. (2.54). It is also observed that there is a lower PVP mass fraction gradient within the droplet for 5% R.H., cf. Fig. 4.40, when compared with dry air before solid layer develops, implying that humidity leads to smaller size particles with less porosity. Thus, it appears that the relative humidity plays a major role in the mass fraction gradients development within the droplet.

Figure 4.41 shows the comparison of present model predictions of PVP/water droplet surface and that of RMM. The behavior is similar to the revelations made in

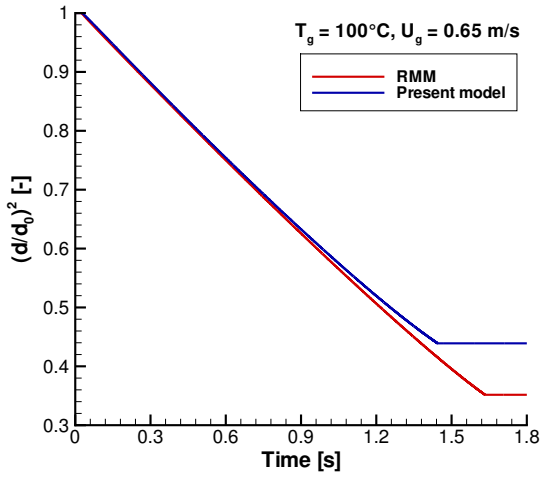

Fig. 4.41: Time evolution of PVP/water droplet surface area predicted by present model and RMM.

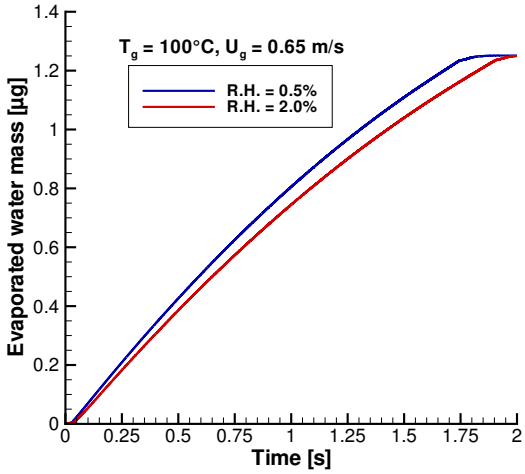

Fig. 4.42: Effect of relative humidity on the water evaporation rate from the mannitol/water droplet.

mannitol/water droplet case, i.e., the RMM overpredicts the decrease in droplet surface area, and thereby the time required for solid layer formation due to the assumption of homogeneous liquid mixture within the droplet, which delays the formation of the solid layer.

Figure 4.42 shows the effect of relative humidity on the water evaporation rate from a mannitol/water droplet subjected to air with 0.5% and 2.0% R.H. For low relative humidity, the mass fraction of water vapor in the bulk of the air, $Y_{1,\infty}$, cf. Eq. (2.54), is decreased, leading to a higher driving mass transfer rate, and this would eventually cause faster water evaporation, and thereby somewhat quicker solid layer formation. With 0.5% R.H. the solid layer develops in about 1.7 s whereas with 2% R.H., the same is observed in 1.9 s.

Figure 4.43 shows the effect of modification of initial PVP mass fraction on the evolution of droplet radius and temperature for 0.075 and 0.15 PVP initial mass fractions. All other conditions remain fixed. Less initial PVP mass fraction implies that there is more water to evaporate leading to smaller size particle with longer drying time. With an initial PVP mass fraction of 0.15, the droplet radius reduces to 46.4 µm in about 1.4 s whereas with 0.075 PVP initial mass fraction, the droplet radius decreases to 38.5 µm in about 1.7 s before the solid layer formation begins, which is indicated by the quick rise in droplet temperature reaching the same value in both cases as seen in Fig. 4.43, showing that initial mass fraction of PVP does not affect the final temperature of the particle.

Though the final drying step is not yet added to this model, the results presented

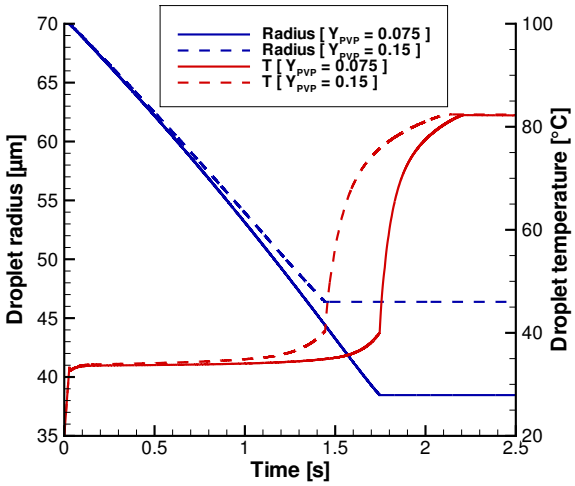

Fig. 4.43: Effect of initial PVP mass fraction on the profiles of droplet radius and temperature.

here for PVP/water and mannitol/water single droplet evaporation and solid layer formation is very promising. The first three stages of bi-component droplet evaporation and drying, i.e., till the solid layer development on the droplet surface is effectively predicted by present model and the comparison of the numerical results with the experiment exhibits very good agreement. Thus, this model is included in DQMOM mathematical formulation in order to simulate bi-component PVP/water spray flows in an axisymmetric, two-dimensional configuration and the results of this system are presented in the next section.

4.4 Two-dimensional Evaporating PVP/Water Spray in Air

This section presents the numerical and experimental results of bi-component evaporating spray flows. Though the developed model can be applied to simulate PVP/water and mannitol/water spray flows, but here only the results of PVP/water spray flows are presented as the initial data with respect to mannitol/water spray is not available. The experimental setup and initial data generation to start numerical simulations are presented in the next subsection followed by the results and discussion.

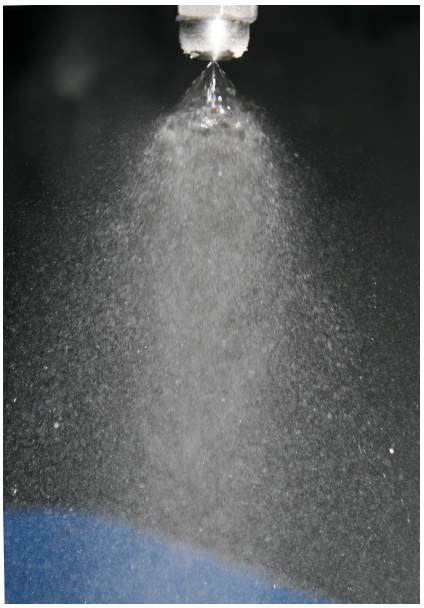

Fig. 4.44: Photograph of the PVP/water spray formation with 112 kg/h liquid inflow rate in experiment [206].

4.4.1 Experiment and Initial Data Generation

The PVP/water spray in air experiments have been carried out by the group of Prof. G. Brenn by spraying a solution of 20% PVP and 80% water (by mass) through the Delavan nozzle SDX-SE-90 at room temperature. The droplet sizes and velocities are recorded at the cross sections of 0.08, 0.12 and 0.16 m away from nozzle orifice using PDA, which provides both droplet size and velocity distributions, similar to the water spray in air measurements. The liquid mass flow rate of these experiments is 112 kg/h and other conditions of the experiment such as gas velocity, gas temperature and pressure are same as the water spray in air. Figure 4.44 displays the PVP/water spray formation in experiment [206]. To generate the initial data for simulating the PVP/water spray in air, the same procedure as outlined in two-dimensional water spray in air is followed here. Figure 4.45 shows the experimental droplet size distribution and the corresponding DQMOM approximation at the radial position 0.036 m from the spray axis and 0.08 m downstream of the nozzle orifice.

4.4.2 Results and Discussion

PVP/water spray flow in air is modeled using the DQMOM where the bi-component droplet evaporation of PVP/water droplets [172, 225, 226] are accounted through the single droplet evaporation and solid formation model presented in Chapter 2 and the results are discussed in Subsection 4.3.3. For droplet motion, droplet coalescence, the

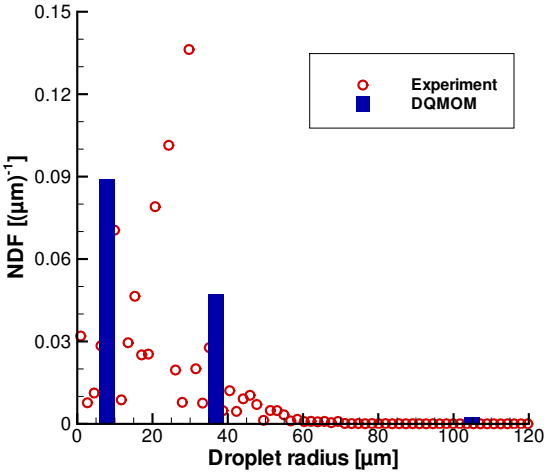

Fig. 4.45: Experimental and DQMOM approximation of droplet number density for PVP/water spray.

same sub-models as employed in water spray are applied here, see Subsection 2.4.

In Fig. 4.46, computed and experimental profiles of Sauter mean diameter (left) and mean droplet diameter (right) of PVP/water spray for a mass inflow rate of 112 kg/h at 0.12 m away from the nozzle exit are shown. Similar to the water spray, the spray distribution assumes a hollow-cone shape, and it is nicely predicted by DQMOM. In both the figures, a closer look reveals that across all the radial positions, the DQMOM

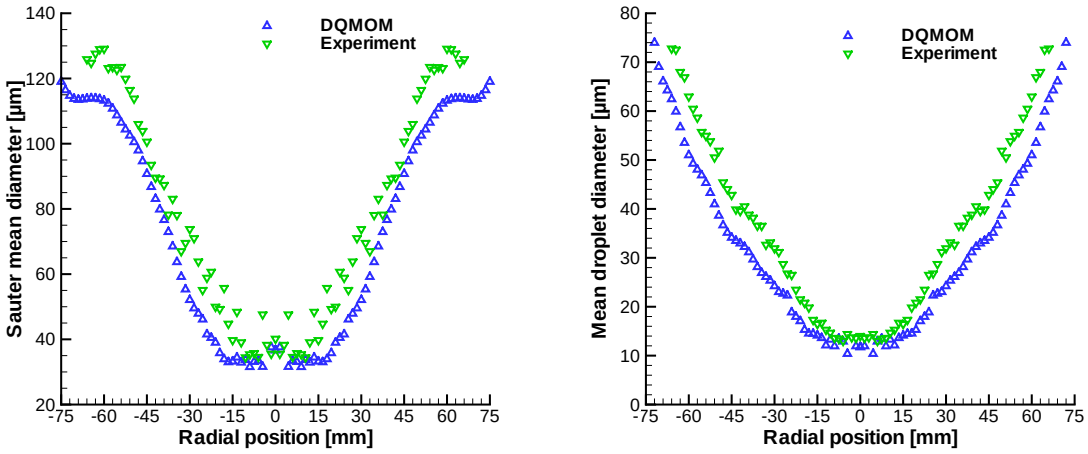

Fig. 4.46: Experimental and numerical profiles of the Sauter mean diameter (left) and mean droplet diameter (right) of PVP/water spray in air at the cross section of 0.12 m distance from the nozzle exit.

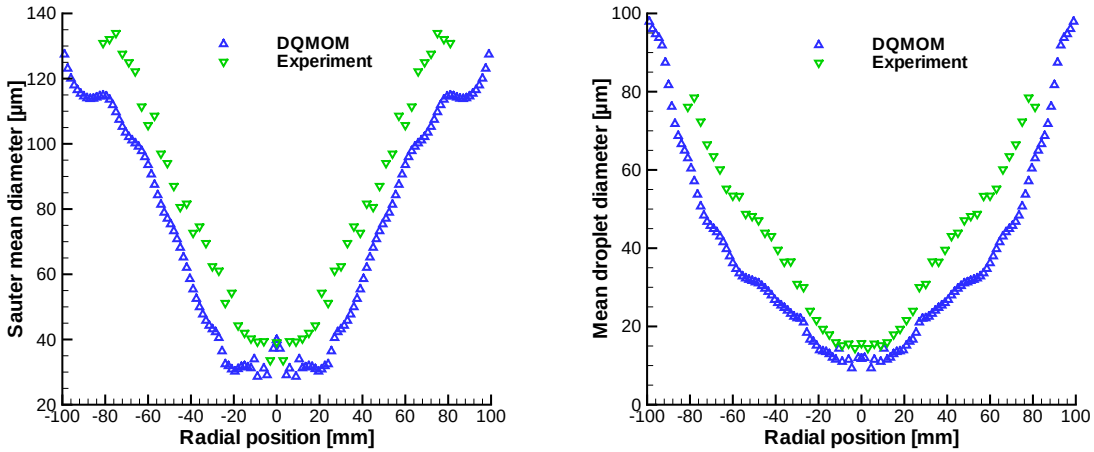

Fig. 4.47: Experimental and numerical profiles of the Sauter mean diameter (left) and mean droplet diameter (right) of PVP/water spray in air at the cross section of 0.16 m distance from the nozzle exit.

underpredicts the experimental results and towards the periphery of the spray some deviation is observed particularly in profiles of Sauter mean diameter as compared to the experiment. This can possibly be explained by the fact that the DQMOM predicts the global droplet distribution, but there could be local discrepancies induced by the gas phase, which is not resolved in the present study. Coupling of DQMOM with the gas phase would eventually improve the simulation results.

Figure 4.47 displays the Sauter mean diameter (left) and mean droplet diameter (right) at further downstream the nozzle exit, i.e., at the cross section 0.16 m. Comparing the maxima in Fig. 4.46 and 4.47 reveals that there is an increase in the Sauter mean diameter and mean droplet diameter, which is converse to the the water spray where decrease in droplet size is found. At a given temperature, the evaporation rate of water from pure water droplets is higher than from the droplets containing PVP dissolved in water due to the non-ideality effect (see Fig. 4.25). An analysis of droplet coalescence reveals that it occurs 1.5 times more often in PVP/water spray compared to water spray, which also contributes to an increased droplet size in the PVP/water spray. The elevated viscosity of PVP leading to higher viscous PVP/water droplets compared to pure water droplets influences the droplet coalescence. The present model is suitable to capture these effects, and a good agreement between the experiment and simulation is found [209].

The mean droplet velocity of PVP/water spray with 112 kg/h liquid inflow rate at 0.12 m away from the nozzle is shown in Fig. 4.48. Increased liquid flow rate leads to higher droplet velocity (compare Figs. 4.23 and 4.48), which increases the chances of

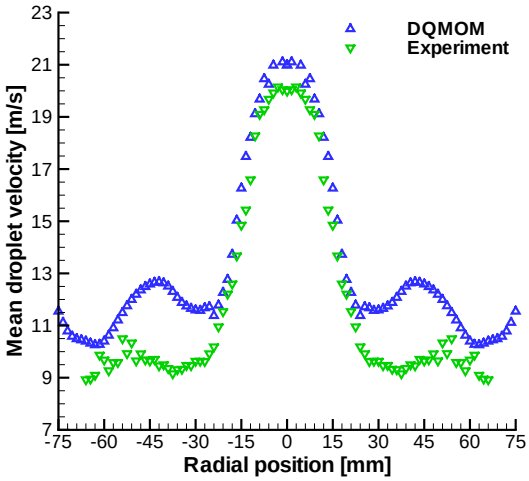

Fig. 4.48: Experimental and numerical profiles of the mean droplet velocity of PVP/water spray in air at the cross section of 0.12 m distance from the nozzle exit.

collision. The smaller size droplets that lie closer to centerline of the spray are moving at higher velocity than the larger size droplets, which is in quite contrast with that of water spray (see Fig. 4.23) where both the larger and smaller size droplets move with higher velocity. This may be because initially the gas around the spray is stagnant and the droplets decelerate by aerodynamic drag. The surrounding gas acquires the momentum lost by the droplets, and this creates a flow field in which gas is continually entrained into the spray. As the entrained gas enters the spray, it drags small liquid drops at the outer regions of the spray inward, and the momentum lost by the droplets at the periphery of the spray is larger than the ones that lie closer to the axis of symmetry, which explains the smaller velocity of larger droplets [227, 228].

Further downstream of the nozzle exit, i.e., at the cross section of 0.16 m away from the nozzle exit, the retardation of the droplet velocity in large size droplet region is observed (see Fig. 4.49) similar to water spray as this effect is dependent on initial liquid flow rate, where low liquid flow rate leads to larger droplets, which take more time to follow the streamlines of the gas than the smaller size droplets [209, 225]. The simulation results are in good agreement with the experiment, particularly in smaller size droplets region whereas towards spray edge there is deviation, which can be attributed to the post-processing of the experimental data and the non-resolved gas phase.

Concerning the differences in evaporation characteristics for water and PVP/water droplet evaporation in air, it is found that for a given liquid flow rate and axial po-

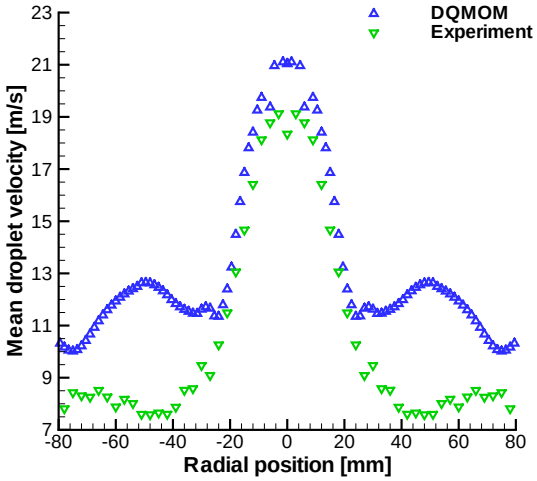

Fig. 4.49: Experimental and numerical profiles of the mean droplet velocity of PVP/water spray in air at the cross section of 0.16 m distance from the nozzle exit.

sition from the nozzle exit, droplet size is larger in water spray (120 kg/h) than the PVP/water spray (112 kg/h), compare Fig. 4.19 with left side of Fig. 4.46, which is because of the high viscosity of PVP/water solution. Moreover, at a given temperature, the evaporation rate from pure water droplet is higher than from PVP/water droplet due to the non-ideality effect caused by polymer presence.

5. Conclusions and Future Work

The objective of the present work is modeling and simulation of polymer or sugar solution spray drying until the solid layer formation at the droplet surface, and dispersion in bi-component evaporating spray flows in an Eulerian framework.

In order to understand the behavior of droplet distribution under various drying conditions, the direct quadrature method of moments (DQMOM) is implemented, for the first time, in two dimensions to study the bi-component evaporating spray flows. In DQMOM, the droplet size and velocity distribution of the spray is modeled by approximating the number density function in terms of joint radius and velocity. The DQMOM has been extended to accommodate gas–liquid interactions such as convective droplet evaporation, drag force and gravity as well as droplet–droplet interactions by including coalescence. The effect of these physical processes on the evolution of droplet size distribution and kinetic properties is analyzed and validated with the experiments. The DQMOM simulation results are also compared with the quadrature method of moments (QMOM) in one-dimensional configuration whereas in two-dimensional axisymmetric configuration DQMOM is compared with discrete droplet model (DDM), which is a well known Euler – Lagrangian approach.

First, evaporating water spray in nitrogen is modeled using DQMOM in one physical dimension, and the simulation results are compared with QMOM. The water evaporation is accounted through convective evaporation model of Abramzon and Sirignano, which accounts for variable liquid and film properties. The drag and droplet coalescence are included through appropriate sub-models. The gas phase is not yet fully coupled with DQMOM but its inlet flow properties are used to compute droplet evaporation and drag. The initial data to start simulations is generated from the experimental data, which were provided by Dr. R. Wengeler, BASF Ludwigshafen. The simulation results are validated with experiment at various cross sections. The influence of individual physical processes is analyzed. It is demonstrated that the model reflects the evaporation to have a pronounced effect on the parameters pertaining to droplet size. More importantly, when evaporation is considered in combination with droplet coalescence, the numerical results are improved significantly and show excellent agreement with experiments. The droplet velocity is largely influenced by the drag force and gravity.

Based on the successful of implementation of DQMOM, it is then extended to model evaporating water in air in two-dimensional, axisymmetric configuration. The same

system is also modeled using DDM. In DQMOM, the source terms are computed same as done in the one-dimensional case, and the evolution of droplet size and velocity distributions are analyzed with both DDM and DQMOM. Droplet collisions are included in DQMOM by modeling the droplet coalescence. The DDM does not include droplet collisions due to computational complexity such as redistribution of droplet classes and increased computational effort. For initialization and validation of the simulation results, experimental data is used, which was provided by Prof. G. Brenn TU Graz, measured using PDA. The experimental data contains droplet size and velocity in axial and radial direction and this data is post-processed in order to eliminate errors in the large size droplets region. The experimental data at the cross section closest to the nozzle exit are used for the generation of initial conditions for the simulations, and the numerical results of DQMOM are compared with experimental data at the later cross sections, and with DDM.

Overall, both the methods i.e., DQMOM and DDM show good agreement with the experiment. Some deviations between DQMOM and experiment are observed that might result from the present DQMOM formulation, which is not yet fully coupled with the gas phase equations. Concerning the experimental data, a post-processing of the raw data has been performed in order to correct the number density of large size droplets with respect to the effective cross section area, leading to different correction factors for different axial positions in experimental data away from the nozzle exit, which may also lead to discrepancy between numerical and experimental results. The DDM performs somewhat better in the periphery of the spray and DQMOM near the centerline. However, DQMOM shows an excellent numerical performance, and droplet coalescence is included with relative ease compared to DDM. Therefore, the DQMOM is further extended to simulate PVP/water sprays in air.

Before simulating the PVP/water spray in air using DQMOM, a model to describe the bi-component droplet evaporation and solid layer formation is developed. The system under consideration is governed by the continuity (diffusion) and energy equations. Brenn's model is modified to include the resistance from the solid layer, and this extended formulation is used to compute the evaporation rate of water from the bi-component droplet. The temperature inside the droplet appears to be uniform, and the change in droplet temperature due to heat exchange between the droplet surface and the surrounding gas is calculated with similar modifications used for mass evaporation rate to account for the resistance from the solid layer. The variable physical and thermal properties and the volume fraction based radius are introduced based on Brenn's model. The predictability and efficiency of the developed single droplet model is first verified by simulating PVP/water and mannitol/water droplets. The liquid mixture is treated as non-ideal with the activity coefficient calculation using the im-

proved UNIFAC-vdW-FV method for PVP in water and ASOG contribution method for mannitol/water solution.

The effect of various drying conditions on the evolution of single droplet characteristics is analyzed and the results are compared with experimental data. These drying conditions include the effect of gas temperature, gas velocity, initial solute (PVP or mannitol) mass fraction and relative humidity, which are found to have significant effect on the evaporation and drying characteristics of PVP/water as well as mannitol/water droplet. The study reveals that an increase in gas velocity and temperature cause earlier formation of the solid layer and faster drying, leading to larger particles with higher porosity. Humidity in air leads to smaller size particles with less porosity. The lower initial solute (PVP or mannitol) mass fraction implies that there is more water to evaporate resulting in smaller size particle with longer drying time. The variation of the activity coefficient of water with PVP mass fraction is much higher than that of mannitol, causing a stronger retardation of water evaporation rate from the PVP/water droplet compared to mannitol/water, which results in a faster solid layer formation for mannitol/water droplets. The present model successfully predicts the first three stages of droplet evaporation and drying, i.e., until solid layer formation at the droplet surface, which can readily be incorporated into an overall model of spray drying.

The developed bi-component single droplet evaporation and drying model is then included in the DQMOM to simulate evaporating PVP/water spray flows in air in two-dimensional, axisymmetric configuration. Even though the developed spray model is equally applicable to simulate PVP/water and mannitol/water spray flows but only computations of PVP/water spray flows are performed as mannitol/water spray flow experimental data is not available. The physical processes of the spray such as drag and coalescence are included through the appropriate sub-models. Numerical results are compared with experimental data at different cross sections, and results are found to be in good agreement with experiment. Some deviations between DQMOM and experiment in case of mean droplet diameter are observed that might have originated from the present DQMOM formulation, which is not yet fully coupled with the gas phase equations. Moreover, the employed numerical technique uses an explicit finite difference method to solve the DQMOM transport equations – an implicit scheme may lead to considerable improvement. Additionally, the Schiller–Naumann correlation for drag coefficient may need revision. In conclusion, mono- and bi-component evaporating spray flows and preliminary stages of spray drying are successfully modeled and simulated using DQMOM.

During spray drying, elevated gas temperature enhances droplet heating and evaporation thus advanced formulation of DQMOM is required in order to model spray

drying. Even though the current DQMOM method includes the droplet radius and velocity as internal variables, inclusion of droplet temperature and analogous terms in the Williams' spray equation will enable modeling of spray drying. The gas phase equations should be resolved and coupled to the DQMOM transport equations, which would eventually enable the model to predict the spray drying process, i.e., from the atomized liquid droplets to the dried end product.

Concerning the bi-component single droplet evaporation and drying, the developed model needs further extension to account for the capillary force, internal circulation, shriveling effect or disorientation of particle shape towards the final stages of drying as observed in experiment. This would further improve the model predictability of solid layer formation, porosity within the solid layer and final particle size.

Appendix

A. Nomenclature

Symbol	Unit	Description
a_{w}	-	Water activity
a_α, b_α	-	Variables in Wheeler algorithm
a_n		Source term in DQMOM
$A(t)$	m^2	Time dependent droplet surface area
B_M	-	Spalding mass transfer number
$\mathrm{B}_{M,i}$	-	Spalding mass transfer number of coefficient i
B_T	-	Spalding heat transfer number
Bi	-	Biot number
b_n		Source term in DQMOM
c	m/s	Speed of the sound in gas medium
C_D	-	Drag coefficient in spray model
$C_{p\mathrm{g}}$	J/(kg K)	Specific heat capacity of gas
$C_{p\mathrm{L}}$	J/(kg K)	Specific heat capacity of liquid
$C_{p\mathrm{Lf}}$	J/(kg K)	Specific heat capacity in the film
$\mathbf{c}_n$		Source term in DQMOM
$c_{1,n}, c_{2,n}, c_{3,n}$		Source terms in DQMOM
d	m	Droplet diameter
D_{12}	m^2/s	Binary diffusion coefficient of liquid mixture
$d_{1,0}$, d_{10}	m	Mean droplet diameter
$d_{3,2}$, d_{32}	m	Sauter mean diameter
$d_{k+1,k}$	m	General definition of mean diameter
D_{f}	m^2/s	Mass diffusion coefficient in the film
D_{s}	m^2/s	Mass diffusion coefficient of vapor in solid layer
E_c	-	Efficiency of the droplet coalescence
$\mathbf{F}$	m/s^2	Total force per unit mass on droplets
$\mathbf{F}_h$	m/s^2	History term or Basset force per unit mass
$\mathbf{F}_L$	m/s^2	Lift force per unit mass
f		Droplet distribution function
f	m^{-3}	Number density function
$f_M^{ME}(x)$	m^{-3}	Maximum entropy method approximation of number density function
$\mathbf{g}$	m/s^2	Acceleration due to gravity
G		Moment flux term defined in finite volume method
h	$\mathrm{W}/(\mathrm{m}^2\ \mathrm{K})$	Convective heat transfer coefficient
h	J/kg	Total specific enthalpy
H	-	Hessian matrix
$\mathcal{H}[f]$		Shannon entropy

$\mathbf{J}_q^c$	J/(m^2 s)	Heat flux due to thermal conductivity
$\mathbf{J}_q^d$	J/(m^2 s)	Heat flux due to molecular mass diffusion
k	m^2/s^2	Turbulent kinetic energy
k	m^2/s	Evaporation constant in d^2 law
k_{gf}	W/(m K)	Thermal conductivity in the film
k_{l}	W/(m K)	Thermal conductivity of the liquid
k_{s}	W/(m K)	Thermal conductivity of the solid layer
$L_V(T_{\mathrm{s}})$	J/kg	Latent heat of vaporization at T_{s}
Le	-	Lewis number
m	kg	Droplet mass
$m_{p,k}$	m	Droplet mass in k$^{\mathrm{th}}$ parcel
$\dot{m}$	kg/s	Total evaporation rate
M		Moment set defined in QMOM
Ma	-	Mach number
M_k		k^{th} moment
M_{w}	kg/mol	Water molecular weight
$\bar{M}$	kg/mol	Mean molecular weight in film
$n_d(d)$	m^{-3}	Number density function based on the droplet diameter d
N	m^{-3}	Total number density
N	-	Number of nodes in DQMOM
$\widetilde{\mathrm{Nu}}$	-	Modified Nusselt number
Nu	-	Nusselt number
Oh	-	Ohnesorge number
p	Pa	Pressure
$P_{k,l}$		Phase-space transform defined in DQMOM
p_{m}	Pa	Total pressure in the film
$p_{\mathrm{vap},i}$	Pa	Vapor pressure of component i
Pr	-	Prandtl number
Q_{L}	J/s	Net heat transferred to the droplet
Q_f		Rate of change in f due to droplet coalescence
r	m	Radial coordinate
r_n	m	Approximated droplet radius of n^{th} node in DQMOM
$r_{p,k}$	m	Droplet radius in k$^{\mathrm{th}}$ parcel
Re	-	Reynolds number
$\mathrm{Re_d}$	-	Droplet Reynolds number
R_0	m	Initial droplet radius
R_i	m	Volume fraction based droplet radius
R	m	Droplet radius
$R = \frac{\mathrm{d}r}{\mathrm{d}t}$	m/s	Rate of change in droplet radius due to evaporation

$\mathbf{S}_n$		Vector of source terms
S_g		Source term due to gas phase
S_l		Source term due to liquid phase
S_α	kg/s	Chemical production rate of species α in mass
Sc	-	Schmidt number
$\widetilde{\mathrm{Sh}}$	-	Modified Sherwood number
Sh	-	Sherwood number
T	K	Droplet temperature
T_g	K	Gas temperature
T_s	K	Droplet surface temperature
T_∞	K	Temperature in the bulk of the gas
$T_{p,k}$	K	Droplet temperature in k^{th} parcel
t	s	Time
t_s	s	Time taken for initiation of solid layer
$\mathbf{u}$	m/s	Gas velocity in physical space
$\mathbf{V}$	m/s	Gas velocity in sample space
$\mathbf{v}$	m/s	Droplet velocity in physical space
U_g	m/s	Gas velocity
u_x	m/s	Axial component of gas velocity
u_r	m/s	Radial component of gas velocity
v_x	m/s	Axial component of droplet velocity
v_r	m/s	Radial component of droplet velocity
V	m^3	Droplet volume
V_i	m^3	Volume of component i within the droplet
We_g	-	Gas Weber number
$\langle x^k \rangle$		Approximated k^{th} moment
X_i	-	Mole fraction of species i
$X_{\mathrm{L},i}$	-	Mole fraction of species i in the liquid
$\mathbf{x}$	m	Geometrical coordinates
Y_i	-	Mass fraction of component i inside the droplet
Y_s	-	Mass fraction of vapor at the droplet surface
Y_∞		Mass fraction of vapor in the bulk of the gas
$Y_{i,\mathrm{s}}$	-	Mass fraction of species i at the droplet surface
$Y_{i,\infty}$	-	Mass fraction of species i in the bulk of the gas
γ_i	-	Activity coefficient of component i
Γ_f		Droplet coalescence function
Γ_h	kg/(m s)	Thermal diffusion coefficient
$\Gamma_{h,\mathrm{eff}}$	kg/(m s)	Effective thermal diffusion coefficient
$\Gamma_{k,\mathrm{eff}}$	kg/(m s)	Effective exchange coefficient for k

$\Gamma_{\epsilon,\text{eff}}$	kg/(m s)	Effective exchange coefficient for ϵ
$\Gamma_{M,\text{eff}}$	kg/(m s)	Effective mean mass diffusion coefficient of the mixture
Δt	s	Time step
Δx	m	Spatial step
δ_{k0}	-	Kronecker delta
ϵ	m^2/s^3	Dissipation rate of turbulent kinetic energy
λ	W/(m K)	Thermal conductivity
μ	kg/(m s)	Dynamic viscosity
μ_{eff}	kg/(m s)	Effective viscosity coefficient
μ_{f}	kg/(m s)	Dynamic viscosity in the film
μ_l	kg/(m s)	Laminar viscosity coefficient
μ_t	kg/(m s)	Turbulent viscosity coefficient
ξ	-	Set of internal coordinate
π_α	-	Variable in Wheeler algorithm
ρ	kg/m^3	Mass density
ρ_{g}	kg/m^3	Gas density
ρ_{l}	kg/m^3	Liquid density
$\sigma_{\alpha,\beta}$		Variable defined in Wheeler algorithm
σ_ϵ	-	Effective Schmidt number for ϵ
ϕ	-	Relates the Spalding mass and heat transfer coefficients
χ	s^{-1}	Dissipation rate of mixture fraction
ψ	-	Evaporative flux
Ω_{g}	s^{-1}	Gas vorticity

Subscripts and Superscripts

Symbol	Quantity
d	Droplet
f	Film
g	Gas
l	Liquid
m	Mixture
n	Index for the number of node
p	Parcel
s	Surface
w	Water
$\langle\ \rangle$	Moment

List of Abbreviations

Abbreviation	Meaning
CDM	continuous droplet model
CFD	computational fluid dynamics
CFL	Courant-Friedrichs-Lewy condition
CFM	continuous formulation model
CM	method of classes
CQMOM	conditional quadrature method of moments
DDB	droplet deformation and breakup
DDM	discrete droplet model
DNS	direct numerical simulation
DQMOM	direct quadrature method of moments
DSD	droplet size distribution
ETAB	enhanced Taylor analogy breakup model
LB	lattice-Boltzmann method
LDA	laser Doppler anemometry
LES	large eddy simulation
LHF	local homogeneous flow model
ME	maximum entropy method
MOM	method of moments
NDF	number density function
PBE	population balance equation
PD	product-difference algorithm
PDA	phase Doppler anemometry
PSIC	particle-source-in-cell method
PVP	polyvinylpyrrolidone
QBSM	quadrature based sectional method
QMOM	quadrature method of moments
RANS	Reynolds-average Navier – Stokes equations
RMM	rapid mixing model
RTI	Rayleigh-Taylor instability
SF	separated flow model
TAB	Taylor analogy breakup model
VOF	volume of fluid method
WB	wave breakup model

B. Acknowledgements

The research work was carried out at Interdisciplinary Center for Scientific Computing (IWR), University of Heidelberg, and this study is funded by German Science Foundation (DFG) through the priority program "SPP1423".

First and foremost I would to like to express my deep sense of gratitude to my supervisor, Prof. E. Gutheil, who constantly motivated, taught, encouraged, supported and patiently guided me throughout this work. She offered me this work while I was about to finish my Master studies, and I thank her for bestowing enormous confidence on me. She perseveringly corrected the research abstracts, papers, this thesis, and her style of correction given me an opportunity to be familiar with scientific writing. She helped me a lot in day to day activities as well. Her endless kindness and incomparable support cannot be thanked adequately here.

I am thankful to my co-supervisor, PD Dr. N. Dahmen, for his guidance and support in my research, and for correcting this thesis.

I would like to thank E. Wimmer, Prof. G. Brenn (TU Graz), Dr. R. Wengeler (BASF Ludwigshafen) for providing the experimental data. Special thanks to Prof. G. Brenn for extending his support and comments in understanding and correction of experimental data. Special thanks to Prof. N. Urbanetz for the fruitful discussions on mannitol/water system. I would like thank all the members of the DFG "SPP 1423" for their support.

I express my sincere thanks to all my colleagues, L. Cao, H. Großhans, R. M. Humza, Y. Hu, H. Olguin, M. Trunk, X. G. Cui, D. Urzica and E. Vogel. Thanks to N. Wenzel for his help in experimental data handling. Special thanks to H. Großhans for proof reading this thesis and translating the abstract in German. I sincerely thank E. Vogel for her kind help in all administrative matters, which made my life easier in Germany, and thanks to her also for the corrections of German abstract.

I thank my family members, especially, my mother (Sulochana), beloved brother (Surender), and sister (Swarupa) for their constant support and endless love. I wish to express special thanks to my wife (Tanuja), who encouraged me in every hard hour, and corrected this thesis with humongous patience.

Last but not least, the financial support of DFG through "SPP1423" and HGS-MathComp is gratefully acknowledged.

Bibliography

[1] K. Masters: *Spray drying handbook*: Longman Scientific & Technical, Harlow, England (1991)

[2] R. Vehring: Pharmaceutical particle engineering via spray drying. *Pharmaceutical Research*, **25**, 999–1022 (2008)

[3] A. Mescher, E. M. Littringer, R. Paus, N. A. Urbanetz, P. Walzel: Homogene Produkteigenschaften in der Sprühtrocknung durch laminare Rotationszerstäubung. *Chemie Ingenieur Technik*, **84**, 154–159 (2012)

[4] F. G. Kieviet: *Modelling quality in spray drying.* PhD Thesis, Department of Chemical Engineering, Eindhoven University of Technology, (1997)

[5] T. A. G. Langrish, D. F. Fletcher: Prospects for the modeling and design of spray dryers in the 21st century. *Drying Technology*, **21(2)**, 197–215 (2003)

[6] R. Vieweg, M. Reiher, H. Scheurlen: *Kunststoff-Handbuch XI*: Carl-Hanser-Verlag, München (1971)

[7] F. Ullmanns: *Ullmanns Encyklopädie der technischen Chemie, 4. Auflage*: Urban & Schwarzenberg (1980)

[8] V. Bühler: *Polyvinylpyrrolidone excipients for pharmaceuticals: Povidone, crospovidone and copovidone*: Springer (2005)

[9] F. Fischer, S. Bauer: Polyvinylpyrrolidon. Ein Tausendsassa in der Chemie. *Chemie in unserer Zeit*, **43**, 376–383 (2009)

[10] A. Göthlich, S. Koltzenburg, G. Schornick: Funktionale Polymere im Alltag: Vielseitig. *Chemie in unserer Zeit*, **39**, 262–273 (2005)

[11] A. Mescher, J. Kamplade, P. Walzel: Personal communication (2012)

[12] Mannitol: http://en.wikipedia.org/wiki/Mannitol

[13] M. W. Kearsley, R. C. Deis: *Sorbitol and manntiol,* in *Sweeteners and sugar alternatives in food technology*: Blackwell Publishing Ltd, Oxford (2006)

[14] A. J. Hickey: Lung deposition and clearance of pharmaceutical aerosols: What can be learned from inhalation toxicology and industrial hygiene?. *Aerosol Science and Technology*, **18(3)**, 290–304 (1993)

[15] K. Bechtold-Peters, H. Luessen: *Pulmonary Drug Delivery: Basics, Applications and Opportunities for Small Molecules and Biopharmaceutics*: ECV Editio-Cantor-Verlag (2007)

[16] S. K. Tee, C. Marriott, X. M. Zeng, G. P. Martin: The use of different sugars as fine and coarse carriers for aerosolised salbutamol sulphate. *International Journal of Pharmaceutics*, **208**, 111–123 (2000)

[17] S. G. Maas, G. Schaldach, P. Walzel, N. A. Urbanetz: Tailoring dry powder inhaler performance by modifying carrier surface topography by spray drying. *Atomization and Sprays*, **20(9)**, 763–774 (2010)

[18] W. Kaialy, M. N. Momin, M. D. Ticehurst, J. Murphy, A. Nokhodchi: Engineered mannitol as an alternative carrier to enhance deep lung penetration of salbutamol sulphate from dry powder inhaler. *Colloids and Surfaces B: Biointerfaces*, **79**, 345–356 (2010)

[19] G. Pilcer, K. Amighi: Formulation strategy and use of excipients in pulmonary drug delivery. *International Journal of Pharmaceutics*, **392**, 1–19 (2010)

[20] D. E. Braun, S. G. Maas, N. Zencirci, C. Langes, N. A. Urbanetz, U. J. Griesser: Simultaneous quantitative analysis of ternary mixtures of d-mannitol polymorphs by FT-Raman spectroscopy and multivariate calibration models. *International Journal of Pharmaceutics*, **385**, 29–36 (2010)

[21] E. Littringer, A. Meshcer, S. Eckhard, H. Schröttner, C. Langes, M. Fries, U. Griesser, P. Walzel, N. Urbanetz: Spray drying of Mannitol as a drug carrier–the impact of process parameters on product properties. *Drying Technology*, **30**, 114–124 (2012)

[22] S. G. Maas, G. Schaldach, E. M. Littringer, A. Mescher, U. J. Griesser, D. E. Braun, P. Walzel, N. A. Urbanetz: The impact of spray drying outlet temperature on the particle morphology of mannitol. *Powder Technology*, **213**, 27–35 (2011)

[23] S. Sundaram, L. R. Collins: Collision statistics in an isotropic particle-laden turbulent suspension. Part 1: direct numerical simulations. *Journal of Fluid Mechanics*, **335**, 75–109 (1997)

[24] K. D. Squires, J. K. Eaton: Measurements of particle dispersion obtained from direct numerical simulations of isotropic turbulence. *Journal of Fluid Mechanics*, **226**, 1–35 (1991)

[25] T. Baritaud, T. Poinsot, Baum, M.: *Direct numerical simulation for turbulent reacting flows*: Paris: Editions Technip (1996)

[26] K. Luo, H. Pitsch, M. G. Pai, O. Desjardins: Direct numerical simulations and analysis of three dimensional n-heptane spray flames in a model swirl combustor. *Proceedings of the Combustion Institute*, **33**, 2143–2152 (2011)

[27] P. Moin, K. Mahesh: DNS: a tool for turbulence research. *Annual Review of Fluid Mechanics*, **30**, 539–578 (1998)

[28] D. L. Marchisio, R. O. Fox: *Multiphase reacting flows: Modelling and simulation* CISM International Centre for Mechanical Sciences, No. 492: Springer London, Limited (2007)

[29] M. Boivin, O. Simonin, K. D. Squires: On the prediction of gas-solid flows with two-way coupling using large eddy simulation. *Physics of Fluids*, **12**, 2080–2090 (2000)

[30] P. Givi: Quality assessment of the filtered density function for large eddy simulation. *1st workshop on Quality Assessment of Unsteady Methods for Turbulent Combustion Prediction and Validation*, June 16-17, Darmstadt (Seeheim-Jugenheim), Germany (2005)

[31] J. Janicka, A. Sadiki: Large eddy simulation of turbulent combustion systems. *Proceedings of the Combustion Institute*, **30**, 537–547 (2005)

[32] J. A. Langford, R. D. Moser: Optimal LES formulations for isotropic turbulence. *Journal of Fluid Mechanics*, **398**, 321–346 (1999)

[33] J. Meyers, B. Geurts, P. Sagaut: *Quality and reliability of large-eddy simulations.* Vol. 12: ERCOFTAC series, Springer (2008)

[34] Q. Z. Wang, K. D. Squires: Large eddy simulation of particle-laden turbulent channel flow. *Physics of Fluids*, **8(5)**, 1207–1223 (1996)

[35] J. K. Duckowicz: A particle-fluid numerical model for liquid sprays. *Journal of Computational Physics*, **35(2)**, 229–253 (1980)

[36] M. A. Pakhomov: RANS simulation of effect of evaporating droplets on a turbulent heat transfer in a mist flow in a sudden pipe expansion. *Computational Thermal Sciences*, **2(4)**, 311–321 (2010)

[37] S. B. Pope: *Turbulent flows*: Cambridge University Press (2000)

[38] C. W. Hirt, B. D. Nichols: Volume of fluid method for the dynamics of free boundaries. *Journal of Computational Physics*, **39(1)**, 201–225 (1981)

[39] S. Succi: *The lattice Boltzmann equation: For fluid dynamics and beyond,* Numerical Mathematics and Scientific Computation: Clarendon Press, Oxford (2001)

[40] S. E. Elgobashi, T. W. Abou-Arab: A two-equation turbulence model for two-phase flows. *Physics of Fluids*, **26**, 931–938 (1983)

[41] D. Ramakrishna: *Population balances: Theory and applications to particulate systems in engineering*: Academic Press, London (2000)

[42] F. A. Williams: Spray combustion and atomization. *Physics of Fluids*, **1**, 541–545 (1958)

[43] S. K. Freidlander: *Smoke, dust, and haze*: Oxford University Press, Oxford (2000)

[44] F. Gelbard, J. H. Seinfeld: Numerical solution of the dynamic equation for particulate systems. *Journal of Computational Physics*, **28**, 357–375 (1978)

[45] F. Laurent, M. Massot: Multi-fluid modeling of laminar poly-dispersed spray flames: origin, assumptions and comparison of sectional and sampling methods. *Combustion Theory and Modelling*, **5(4)**, 537–572 (2001)

[46] F. Laurent, M. Massot, P. Villedieu: Eulerian multi-fluid modeling for the numerical simulation of coalescence in polydisperse dense liquid sprays. *Journal of Computational Physics*, **194(2)**, 505–543 (2004)

[47] M. Massot, S. de Chaisemartin, L. Freret, D. Kah, F. Laurent: Modeling and computations of nanoparticles in fluid flows. *Eulerian Multi-Fluid Models: Modeling and Numerical Methods, RTO - Lecture Series du von Karman Institute*, 1–86, (2009)

[48] D. L. Marchisio, R. D. Vigil, R. O. Fox: Quadrature method of moments for aggregation–breakage processes. *Journal of Colloid and Interface Science*, **258**, 322–334 (2003)

[49] D. L. Marchisio, J. T. Pikturna, R. O. Fox, R. D. Vigil, A. A. Barresi: Quadrature method of moments for population-balance equations. *AIChE Journal*, **49(5)**, 1266–1276 (2003)

[50] D. L. Marchisio, R. D. Vigil, R. O. Fox: Implementation of the quadrature method of moments in CFD codes for aggregation–breakage problems. *Chemical Engineering Science*, **58**, 3337–3351 (2003)

[51] R. McGraw: Description of aerosol dynamics by the quadrature method of moments. *Aerosol Science and Technology*, **27(2)**, 255–265 (1997)

[52] A. Passalacqua, R. O. Fox, R. Garg, S. Subramaniam: A fully coupled quadrature-based moment method for dilute to moderately dilute fluid–particle flows. *Chemical Engineering Science*, **65**, 2267–2283 (2010)

[53] D. L. Marchisio, R. O. Fox: Solution of population balance equations using the direct quadrature method of moments. *Journal of Aerosol Science*, **36**, 43–73 (2005)

[54] R. O. Fox: Bivariate direct quadrature method of moments for coagulation and sintering of particle populations. *Journal of Aerosol Science*, **37**, 1562–1580 (2010)

[55] G. Dufour, P. Villedieu: A second-order multi-fluid model for evaporating sprays. *ESAIM: Mathematical Modelling and Numerical Analysis (M2AN)*, **39(5)**, 931–963 (2005)

[56] J. Gimbun, Z. K. Nagy, C. D. Rielly: Simultaneous quadrature method of moments for the solution of population balance equations, using a differential algebraic equation framework. *Industrial and Engineering Chemistry Research*, **48**, 7798–7812 (2009)

[57] R. Grosch, H. Briesen, W. Marquardt, M. Wulkow: Generalization and numerical investigation of QMOM. *AIChE Journal*, **53(1)**, 207–227 (2007)

[58] C. Laurent, G. Lavergne, P. Villedieu: Quadrature method of moments for modeling multi-component spray vaporization. *International Journal of Multiphase Flow*, **36**, 51–59 (2010)

[59] J. Akroyd, A. J. Smith, L. R. McGlashan, M. Kraft: Comparison of the stochastic fields method and DQMoM-IEM as turbulent reaction closures. *Chemical Engineering Science*, **65**, 5429–5441 (2010)

[60] R. O. Fox, L. Laurent, M. Massot: Numerical simulation of polydisperse, dense liquid spray in an Eulerian framework: Direct quadrature method of moments and multi-fluid method. *Journal of Computational Physics*, **227(6)**, 3058–3088 (2008)

[61] J. Madsen: *Computational and experimental study of sprays from the breakup of water sheets.* PhD Thesis, The Faculty of Engineering and Science, Aalborg University, Denmark, (2006)

[62] B. Abramzon, W. A. Sirignano: Droplet vaporization model for spray combustion calculations. *International Journal of Heat and Mass Transfer*, **32**, 1605–1618 (1989)

[63] M. Friedrich, B. Weigand: Eulerian multi-fluid simulation of polydisperse dense liquid sprays by the direct quadrature method of moments. *10th Triennial International Conference on Liquid Atomization and Spray Systems (ICLASS)*, Kyoto, Japan (2006)

[64] L. Schneider: *A concise moment method for unsteady polydisperse sprays.* PhD Thesis, Fachbereich Maschinenbau, Technischen Universität Darmstadt, (2009)

[65] D. Kah, F. Laurent, M. Massot, S. Jay: A high order moment method simulating evaporation and advection of a polydisperse liquid spray. *Journal of Computational Physics*, **231**, 394–422 (2012)

[66] L. R. Mead, N. Papanicolaou: Maximum entropy in the problem of moments. *Journal of Mathematical Physics*, **25(8)**, 2404–2417 (1984)

[67] M. R. Archambault: *A maximum entropy moment closure approach to modeling the evolution of spray flows.* PhD Thesis, Stanford University, USA, (1999)

[68] R. M. Humza: *Numerical investigation of non-reactive and reactive turbulent spray flows.* PhD Thesis, University of Heidelberg, Germany, (2013)

[69] H. Großhans: *Large eddy simulation of atomizing sprays.* PhD Thesis, Lund University, Sweden, (2013)

[70] G. M. Faeth, L.-P. Hsiang, P.-K. Wu: Structure and breakup properties of sprays. *International Journal of Multiphase Flow*, **21**, 99–127 (1995)

[71] D. L. Marchisio, R. O. Fox: *Computational models for polydisperse particulate and multiphase systems*: Cambridge University Press, Cambridge (2013)

[72] G. M. Faeth: Evaporation and combustion of sprays. *Progress in Energy and Combustion Science*, **9**, 1–76 (1983)

[73] M. W. Thring, M. P. Newby: *In: Fourth Symposium (International) on Combustion: Combustion and Detonation Waves*: Williams & Wilkens Comp. (1953)

[74] Khalil, Whitelaw: *In: Sixteenth Symposium (International) on Combustion*: The Combustion Institute, Pittsburg (1977)

[75] C.-P. Mao, G. A. Szekely, G. M. Faeth: Evaluation of a locally homogeneous flow model of spray combustion *Journal of Energy*, **4(2)**, 78–87 (1980)

[76] C. T. Crowe, M. P. Sharma, D. E. Stock: The particle-source-in cell (PSI-Cell) model for gas-droplet flows. *Journal of Fluids Engineering*, **99**, 325–332 (1977)

[77] J. T. Jurewicz, D. T. Stock, C. T. Crowe: The effect of turbulent diffusion on gas particle flow in an electric Field. *First Symposium on Turbulent Shear Flows*, 12.27–12.33, April 18–20, University Park, PA (1977)

[78] C. T. Crowe: A numerical model for the gas droplet flow field near an atomizer. *First International Conference on Liquid Atomization and Spray Systems*, August 27–31, Tokyo, Japan (1978)

[79] F. A. Williams: *Combustion theory,* Addison-Wesley series in engineering science: Addison-Wesley Pub. Co. (1965)

[80] A. D. Gosman, R. J. R. Johns: Computer analysis of fuel-air mixing in direct-injection engines. *SAE paper*, 800091 (1980)

[81] F. H. Harlow, A. A. Amsden: Numerical calculation of multiphase fluid flow. *Journal of Computational Physics*, **17(1)**, 19–52 (1975)

[82] F. H. Harlow, A. A. Amsden: Flow of interpenetrating material phases. *Journal of Computational Physics*, **18(4)**, 440–464 (1975)

[83] Z. Han, R. D. Reitz, P. J. Claybaker, C. J. Rutland, J. Yang, R. W. Anderson: Modeling the effects of intake flow structures on fuel/air mixing in a direct-injected spark-ignition engine. *SAE paper*, 961192 (1996)

[84] S. Subramaniam, P. J. O'rourke: Numerical convergence of the KIVA-3 code for sprays and its implications for modeling. *Atomization and Sprays*, **8(4)**, 453–469 (1998)

[85] M. Garcia, Y. Sommerer, T. Schonfeld, T. Poinsot: Assessment of Euler-Euler and Euler-Lagrange strategies for reactive large-eddy simulations. *In 1st Workshop INCA–2005*, 65–74, SNECMA Villaroche, France (2005)

[86] E. Riber, M. Garcia, V. Moureau, H. Pitsch, O. Simonin, T. Poinsot: Evaluation of numerical strategies for LES of two-phase reacting flows. *Proceedings of the Summer Program–2006*, 197–211, Center for Turbulence Research, NASA Ames/Stanford Univ. (2006)

[87] L. Huang, K. Kumar, A. S. Mujumdar: Simulation of a spray dryer fitted with a rotary disk atomizer using a three-dimensional computational fluid dynamic model. *Drying Technology*, **22**, 1489–1515 (2004)

[88] D. I. Kolaitis, M. A. Founti: A comparative study of numerical models for Eulerian-Lagrangian simulations of turbulent evaporating sprays. *International Journal of Heat and Fluid Flow*, **27(3)**, 424–435 (2006)

[89] R. Kuriakose, C. Anandharamakrishnan: Computational fluid dynamics (CFD) applications in spray drying of food products. *Trends in Food Science & Technology*, **21**, 383–398 (2010)

[90] J. J. Nijdam, B. Guo, D. F. Fletcher, T. A. G. Langrish: Lagrangian and Eulerian models for simulating turbulent dispersion and coalescence of droplets within a spray. *Applied Mathematical Modelling*, **30**, 1196–1211 (2006)

[91] A. A. Mostafa, H. C. Mongia: On the modeling of turbulent evaporating sprays - Eulerian versus Lagrangian approach. *International Journal of Heat and Mass Transfer*, **30**, 2583–2593 (1987)

[92] M. Mezhericher, A. Levy, I. Borde: Probabilistic hard-sphere model of binary particle–particle interactions in multiphase flow of spray dryers. *International Journal of Multiphase Flow*, **43**, 22–38 (2012)

[93] M. Sommerfeld, G. Kohnen, H. H. Qiu: Spray evaporation in turbulent flow: Numerical calculations and detailed experiments by phase-Doppler anemometry. *Oil & Gas Science and Technology-revue De L Institut Francais Du Petrole*, **48(6)**, 677–695 (1993)

[94] L. Boltzmann: Weitere Studien über das Wärmegleichgewicht unter Gasmolekülen. *Sitzungsberichte der Akademie der Wissenschaften, Wien*, **66**, 275–370 (1872)

[95] C. Cercignani, R. Illner, M. Pulvirenti: *The mathematical theory of dilute gases*: Springer, Berlin (1994)

[96] F. Bouchet: *Advances in kinetic theory and computing: Selected papers*: World Scientific, Singapore (1994)

[97] L. Fréret, S. de Chaisemartin, J. Reveillon, F. Laurent, M. Massot: Eulerian models and three-dimensional numerical simulation of polydisperse sprays. *7th International Conference on Multiphase Flow (ICMF)*, 1–7, May 30–June 4, Tampa, Florida (2010)

[98] M. Massot, F. Laurent, D. Kah, S. de Chaisemartin: A robust moment method for evaluation of the disappearance rate of evaporating sprays. *SIAM Journal on Applied Mathematics*, **70(8)**, 3203–3234 (2010)

[99] S. Kumar, D. Ramakrishna: On the solution of population balance equations by discretization I. A fixed pivot technique. *Chemical Engineering Science*, **51(8)**, 1311–1332 (1996)

[100] S. Kumar, D. Ramakrishna: On the solution of population balance equations by discretization II. A moving pivot technique. *Chemical Engineering Science*, **51(8)**, 1333–1342 (1996)

[101] S. Kumar, D. Ramakrishna: On the solution of population balance equations by discretization III. Nucleation, growth and aggregation of particles. *Chemical Engineering Science*, **52(24)**, 4659–4679 (1997)

[102] M. J. Hounslow, R. L. Ryall, V. R. Marshall: A discretized population balance for nucleation, growth, and aggregation. *AIChE Journal*, **34**, 1821–1832 (1988)

[103] M. Vanni: Approximate population balance equations for aggregation-breakage processes. *Journal of Colloid and Interface Science*, **221**, 143–160 (2000)

[104] Y. Tambour: A sectional model for evaporation and combustion of sprays of liquid fuels. *Israel Journal of Technology*, **18**, 47–56 (1980)

[105] F. Laurent: Analyse numérique d'une méthode multi-fluide Eulérienne pour la description de sprays qui s'évaporent. *C. R. Acad. Sci. Paris Ser. I*, **334**, 417–422 (2002)

[106] R. G. Gordon: Error bounds in equilibrium statistical mechanics. *Journal of Mathematical Physics*, **9**, 655–663 (1968)

[107] H. M. Hulbert, S. Katz: Some problems in particle technology: A statistical mechanical formulation. *Chemical Engineering Science*, **19**, 555–574 (1964)

[108] R. B. Diemer, J. H. Olson: A moment methodology for coagulation and breakage problems: Part 1 – analytical solution of the steady-state population balance. *Chemical Engineering Science*, **57**, 2193–2209 (2002)

[109] R. B. Diemer, J. H. Olson: A moment methodology for coagulation and breakage problems: Part 2 – moment models and distribution reconstruction. *Chemical Engineering Science*, **57**, 2211–2228 (2002)

[110] R. B. Diemer, J. H. Olson: A moment methodology for coagulation and breakage problems: Part 3 – generalized daughter distribution functions. *Chemical Engineering Science*, **57**, 4187–4198 (2002)

[111] R. A. LaViolette, R. A. Berry, R. McGraw: Homogeneous nucleation of metals in a plasma-quench reactor. *Plasma Chemistry and Plasma Processing*, **16**, 249–264 (1996)

[112] R. McGraw, J. H. Sanders: A condensation feedback mechanism for oscillatory nucleation and growth. *Aerosol Science and Technology*, **3**, 367–380 (1984)

[113] S. E. Pratsinis: Simultaneous nucleation, condensation, and coagulation in aerosol reactors. *Journal of Colloid and Interface Science*, **124**, 416–427 (1988)

[114] B. J. Jurcik, J. R. Brock: Numerical simulation of particle formation and growth in rapidly expanding axisymmetric flows. *Journal of Physical Chemistry*, **97**, 323–331 (1993)

[115] R. O. Fox: A quadrature-based third-order moment method for dilute gas-particle flows. *Journal of Computational Physics*, **227**, 6313–6350 (2008)

[116] C. Yoon, R. McGraw: Representation of generally mixed multivariate aerosols by the quadrature method of moments: I. Statistical foundation. *Journal of Aerosol Science*, **35**, 561–576 (2004)

[117] C. Yoon, R. McGraw: Representation of generally mixed multivariate aerosols by the quadrature method of moments: II. Aerosol dynamics. *Journal of Aerosol Science*, **35**, 577–598 (2004)

[118] C. Yuan, R. O. Fox: Conditional quadrature method of moments for kinetic equations. *Journal of Computational Physics*, **230(22)**, 8216–8246 (2011)

[119] R. O. Fox: Higher-order quadrature-based moment methods for kinetic equations. *Journal of Computational Physics*, **228**, 7771–7791 (2009)

[120] H. Dette, W. J. Studden: *The theory of canonical moments with applications in statistics, probability, and analysis*: Wiley, New York (1997)

[121] R. Fan, D. L. Marchisio, R. O. Fox: Application of the direct quadrature method of moments to polydisperse gas-solid fluidized beds. *Powder Technology*, **139**, 7–20 (2004)

[122] T. L. Chan, Y. H. Liu, C. K. Chan: Direct quadrature method of moments for the exhaust particle formation and evolution in the wake of the studied ground vehicle. *Journal of Aerosol Science*, **41**, 553–568 (2010)

[123] B. Selma, R. Bannari, P. Proulx: Simulation of bubbly flows: Comparison between direct quadrature method of moments (DQMOM) and method of classes (CM). *Chemical Engineering Science*, **65(6)**, 1925–1941 (2010)

[124] L. Mazzei, D. L. Marchisio, P. Lettieri: Direct quadrature method of moments for the mixing of inert polydisperse fluidized powders and the role of numerical diffusion. *Industrial and Engineering Chemistry Research*, **49(11)**, 5141–5152 (2010)

[125] S. Ali, A. Vikhansky, T. Løvås: Direct quadrature conditional moment closure for modelling of turbulent combustion. *Flow, Turbulence and Combustion*, **87**, 493–509 (2011)

[126] A. Bruyat, C. Laurent, O. Rouzaud: Direct quadrature method of moments for multicomponent droplet spray vaporization. *7th International Conference on Multiphase Flow (ICMF)*, May 30–June 4, Tampa, Florida (2010)

[127] W. Gumprich, A. Sadiki, M. Sommerfeld: 3D simulation and analysis of dense turbulent sprays using an Eulerian approach coupled to the DQMOM. *13th International Conference on Numerical Combustion (ICNC)*, April 27–29, Corfu, Greece (2011)

[128] W. Gumprich, A. Sadiki, M. Sommerfeld: Numerical investigation of dense turbulent sprays with an Eulerian approach and DQMOM. *Proceedings in Applied Mathematics and Mechanics (PAMM)*, **11(1)**, 599–600 (2011)

[129] W. Gumprich, A. Sadiki: Numerical study of dense turbulent sprays using a coupling of the direct quadrature method of moments with an Eulerian multi-size

moment model. *12th Triennial International Conference on Liquid Atomization and Spray Systems (ICLASS)*, 1–8, September 2–6, Heidelberg, Germany (2012)

[130] C. Hollmann, E. Gutheil: Modeling of turbulent spray diffusion flames including detailed chemistry. *Proceedings of Combustion Institute*, **26(1)**, 1731–1738 (1996)

[131] C. Hollmann, E. Gutheil: Flamelet-modeling of turbulent spray diffusion flames based on a laminar spray flame library. *Combustion Science and Technology*, **135(1-6)**, 175–192 (1998)

[132] E. Gutheil, F. A. Williams: A numerical and asymptotic investigation of structures of hydrogen-air diffusion flames at pressures and temperatures of high-speed combustion. *Proceedings of Combustion Institute*, **23(1)**, 513–521 (1991)

[133] C. K. Law: Heat and mass transfer in combustion: Fundamental concepts and analytical techniques. *Progress in Energy and Combustion Science*, **10**, 295–318 (1984)

[134] W. A. Sirignano: Fluid dynamics of sprays. *Journal of Fluids Engineering*, **115(3)**, 345–378 (1992)

[135] W. Feller: *An introduction to probability theory and its applications,* Wiley mathematical statistics series: Wiley (1966)

[136] R. A. Sack, A. F. Donovan: An algorithm for Gaussian quadrature given modified moments. *Numerische Mathematik*, **18**, 465–478 (1971)

[137] R. O. Fox: Optimal moment sets for multivariate direct quadrature method of moments. *Industrial and Engineering Chemistry Research*, **48(21)**, 9686–9696 (2009)

[138] D. Choi, L. Schneider, N. Spyrou, A. Sadiki, J. Janicka: Evaporation of tetralin spray with direct quadrature method of moments and Eulerian multi-fluid method. *7th International Conference on Multiphase Flow (ICMF)*, 1–8, May 30–June 4, Tampa, Florida (2010)

[139] I. Langmuir: The Evaporation of Small Spheres. *Physical Review*, **12(5)**, 368–370 (1918)

[140] W. A. Sirignano: *Fluid dynamics and transport of droplets and sprays*: Cambridge University Press, New York (1999)

[141] N. A. Chigier: *Energy, combustion, and environment*: McGraw-Hill, New York (1981)

[142] R. Clift, J. R. Grace, M. E. Weber: *Bubbles, drops, and particles*: Academic Press, New York (1978)

[143] I. Glassman: *Combustion*: Academic Press, New York, 2nd Edition (1987)

[144] Lefebvre: *Atomization and sprays,*: Hemisphere, Washington, DC (1989)

[145] F. A. Williams: *Combustion theory: The fundamental theory of chemically reacting flow systems*: Benjamin/Cummings, Menlo Park, CA, 2nd Edition (1985)

[146] C. K. Law: Recent advances in droplet vaporization and combustion. *Progress in Energy and Combustion Science*, **8(3)**, 171–201 (1982)

[147] S. S. Sazhin: Advanced models of fuel droplet heating and evaporation. *Progress in Energy and Combustion Science*, **32**, 162–214 (2006)

[148] P. Atkins, J. D. Paula: *Atkins' physical chemistry*: Oxford Higher Education (2001)

[149] D. H. Charlesworth, W. R. Marshall Jr: Evaporation from drops containing dissolved solids. *AIChE Journal*, **6**, 9–23 (1960)

[150] Y. Sano, R. B. Keey: The drying of a spherical particle containing colloidal material into a hollow sphere. *Chemical Engineering Science*, **37**, 881–889 (1982)

[151] S. Nesic, J. Vodnik: Kinetics of droplet evaporation. *Chemical Engineering Science*, **46**, 527–537 (1991)

[152] G. Brenn: Concentration fields in drying droplets. *Chemical Engineering & Technology*, **27**, 1252–1258 (2004)

[153] P. Seydel, J. Blömer, J. Bertling: Modeling particle formation at spray drying using population balances. *Drying Technology*, **24(2)**, 137–146 (2006)

[154] S. El Golli, J. Bricard, P.-Y. Turpin, C. Treiner: The evaporation of saline droplets. *Journal of Aerosol Science*, **5**, 273–292 (1974)

[155] X. D. Chen: Heat-mass transfer and structure formation during drying of single food droplets. *Drying Technology*, **22**, 179–190 (2004)

[156] M. Farid: A new approach to modelling of single droplet drying. *Chemical Engineering Science*, **58**, 2985–2993 (2003)

[157] S. Nesic: The evaporation of single droplets: Experiments and modelling. *Drying*, **89**, 386–393 (1989)

[158] C. S. Handscomb, M. Kraft, A. E. Bayly: A new model for the drying of droplets containing suspended solids. *Chemical Engineering Science*, **64**, 628–637 (2009)

[159] N. Tsapis, E. R. Dufresne, S. S. Sinha, C. S. Riera, J. W. Hutchinson, L. Mahadevan, D. A. Weitz: Onset of buckling in drying droplets of colloidal suspensions. *Physical Review Letters*, **94**, 018302 (2005)

[160] B. Golman: Modeling of the drying kinetics of slurry droplet in spray drying. *ASEAN Journal of Chemical Engineering*, **11(2)**, 1–7 (2011)

[161] H. W. Cheong, G. V. Jeffreys, C. J. Mumford: A receding interface model for the drying of slurry droplets. *AIChE Journal*, **32**, 1334–1346 (1986)

[162] M. Mezhericher, A. Levy, I. Borde: Theoretical models of single droplet drying kinetics: a review. *Drying Technology*, **28**, 278–293 (2010)

[163] B. Adhikari, T. Howes, B. R. Bhandari, V. Truong: Experimental studies and kinetics of single drop drying and their relevance in drying of sugar-rich foods: A review. *International Journal of Food Properties,*, **3**, 323–351 (2000)

[164] R. Vehring, W. R. Foss, D. Lechuga-Ballesteros: Particle formation in spray drying. *Journal of Aerosol Science*, **38**, 728–746 (2007)

[165] Y. Sugiyama, R. J. Larsen, J.-W. Kim, D. A. Weitz: Buckling and crumpling of drying droplets of colloid-polymer suspensions. *Langmuir*, **22**, 6024–6030 (2006)

[166] A. L. Yarin, G. Brenn, O. Kastner, C. Tropea: Drying of acoustically levitated droplets of liquid-solid suspensions: Evaporation and crust formation. *Physics of Fluids*, **14**, 2289–2298 (2002)

[167] K. Alexander, C. J. King: Factors governing surface morphology of spray-dried amorphous substances. *Drying Technology*, **3**, 321–348 (1985)

[168] T. M. El-Sayed, D. A. Wallack, C. J. King: Changes in particle morphology during drying of drops of carbohydrate solutions and food liquids. 1. Effects of composition and drying conditions. *Industrial and Engineering Chemistry Research*, **29**, 2346–2354 (1990)

[169] D. A. Wallack, T. M. El-Sayed, C. J. King: Changes in particle morphology during drying of drops of carbohydrate solutions and food liquids. 2. Effects on drying rate. *Industrial and Engineering Chemistry Research*, **29**, 2354–2357 (1990)

[170] G. Brenn, L. J. Deviprasath, F. Durst: Computations and experiments on the evaporation of multi-component droplets. *9th Triennial International Conference on Liquid Atomization and Spray Systems (ICLASS)*, Sorrento, Italy (2003)

[171] O. Kastner: *Theoretische und experimentelle Untersuchungen zum Stoffübergang von Einzeltropfen in einem akustischen Rohrlevitator.* PhD Thesis, Friedrich-Alexander University of Erlangen-Nürnberg, Germany, (2001)

[172] S. R. Gopireddy, E. Gutheil: Numerical simulation of evaporation and drying of a bi-component droplet. *International Journal of Heat and Mass Transfer*, **66**, 404–411 (2013)

[173] M. Mezhericher, A. Levy, I. Borde: Theoretical drying model of single droplets containing insoluble or dissolved solids. *Drying Technology*, **25**, 1035–1042 (2007)

[174] C. T. Crowe, M. Sommerfeld, Y. Tsuji: *Multiphase flows with droplets and particles*: CRC Press (1998)

[175] G. K. Batchelor: *An introduction to fluid mechanics*: University Press London (1967)

[176] L. Schiller, A. Z. Neumann: A drag coefficient correlation. *VDI Zeitschrift*, **77**, 318–320 (1933)

[177] J. O. Hinze: *Turbulence*: McGraw-Hill, New York (1975)

[178] M. Pilch, C. A. Erdman: Use of breakup time data and velocity history data to predict the maximum size of stable fragments for acceleration-induced breakup of a liquid drop. *International Journal of Multiphase Flow*, **13(6)**, 741–757 (1987)

[179] R. D. Reitz: Modeling atomization processes in high-pressure vaporizing sprays. *Atomisation and Spray Technology*, **3**, 309–337 (1987)

[180] P. J. O'Rourke, A. A. Amsden: The TAB method for numerical calculation of spray droplet breakup. *SAE Paper*, 872089 (1987)

[181] F. X. Tanner: Liquid jet atomization and droplet breakup modeling of non-evaporating diesel fuel sprays. *SAE Tchnical Paper*, 970050 (1997)

[182] R. D. Reitz, Z. Liu, S. S. Hwang: Breakup mechanisms and drag coefficients of high-speed vaporizing liquid drops. *Atomization and Sprays*, **6**, 353–376 (1996)

[183] E. A. Ibrahim, H. Q. Yang, A. J. Przekwas: Modeling of spray droplets deformation and breakup. *AIAA: Journal of Propulsion and Power*, **9**, 651–654 (1993)

[184] G. H. Ko, H. S. Ryou: Modeling of droplet collision-induced breakup process. *International Journal of Multiphase Flow*, **31**, 723–738 (2005)

[185] C. Planchette, G. Brenn: Liquid encapsulation by binary collisions of immiscible liquid drops. *11th Triennial International Conference on Liquid Atomization and Spray Systems (ICLASS)*, Vail, Colorado USA (2009)

[186] P. J. O'Rourke: *Collective drop effects on vaporizing liquid sprays.* PhD Thesis, Mechanical and Aerospace Engineering, Princeton University, (1981)

[187] P. Villedieu, J. Hylkema: Une méthode particulaire aléatoire reposant sur une équation cinétique pour la simulation numérique des sprays denses de gouttelettes liquides. *Mathematical Problems in Mechanics (Numerical Analysis), C. R. Acad. Sci. Paris, t. 328*, **1**, 323–328 (1997)

[188] R. Courant, K. Friedrichs, H. Lewy: Über die partiellen Differenzengleichungen der mathematischen Physik. *Mathematische Annalen*, **100**, 32–74 (1928)

[189] B. Perthame: *Kinetic formulation of conservation laws*: Oxford University Press, Oxford (2002)

[190] O. Desjardins, R. O. Fox, P. Villedieu: A quadrature-based moment method for dilute fluid-particle flows. *Journal of Computational Physics*, **227**, 2514–2539 (2008)

[191] S. R. Gopireddy, R. M. Humza, E. Gutheil: Modeling and simulation of evaporating spray flows with coalescence in an Eulerian framework. *Chemie Ingenieur Technik*, **84(3)**, 349–356 (2012)

[192] J. Anderson: *Computational fluid dynamics: The basics with applications* McGraw-Hill Series in Aeronautical and Aerospace Engineering: McGraw-Hill Education, New York (1995)

[193] B. Fornberg: Generation of finite difference formulas on arbitrarily spaced grids. *Mathematics of Computation*, **51**, 699–706 (1988)

[194] W. Gautschi: *Numerical analysis: An introduction*: Birkhäuser, Boston (MA) (1997)

[195] S. V. Patankar: *Numerical heat transfer and fluid flow.* Series in computational methods in mechanics and thermal sciences: Taylor & Francis (1980)

[196] W. R. Marshall: *Atomization and spray drying,* Chemical engineering progress monograph series: American Institute of Chemical Engineers (1954)

[197] M. Stieß: *Mechanische Verfahrenstechnik-Partikeltechnologie 1*: Springer, New York, 3rd Edition (2008)

[198] S. R. Gopireddy, R. M. Humza, E. Gutheil: Numerical simulation of an evaporating spray using direct quadrature method of moments. *24th European Conference on Liquid Atomization and Spray Systems (ILASS)*, 1–8, September 5–7, Estoril, Portugal (2011)

[199] S. R. L. Werner: *Air suspension coating of dairy powders: A micro-level process approach.* PhD Thesis, Massey University, Palmerston North, New Zealand, (2005)

[200] S. R. Gopireddy, R. M. Humza, E. Gutheil: Application of direct quadrature method of moments in modeling of evaporating spray flows. *5. Symposium Produktgestaltung in der Partikeltechnologie, Band 5*, 275–284, May 19–20, Fraunhofer ICT, Pfinztal, Germany (2011)

[201] T. Allen: *Particle size measurement: Volume 1: Powder sampling and particle size measurement,* Powder Technology Series: Springer (1996)

[202] S. R. Gopireddy, R. M. Humza, E. Gutheil: Numerical simulation of evaporating sprays in a convective flow field. *SPRAY - 2012*, 1–8, May 21–22, Berlin, Germany (2012)

[203] S. R. Gopireddy, R. M. Humza, E. Gutheil: Numerical simulation of evaporating sprays in a convective flow field. *12th Triennial International Conference on Liquid Atomization and Spray Systems (ICLASS)*, 1–8, September 2–6, Heidelberg, Germany (2012)

[204] A. Tratnig, G. Brenn: Drop size spectra in sprays from pressure-swirl atomizers. *International Journal of Multiphase Flow*, **36(5)**, 349–363 (2010)

[205] S. R. Gopireddy, R. M. Humza, E. Gutheil: Euler–Euler and Euler–Lagrangian simulations of a water/air spray in a convective flow field. *8th International Conference on Multiphase Flow (ICMF)*, 1–8, May 26–31, Jeju, South Korea (2013)

[206] E. Wimmer, G. Brenn: Personal communication (2011)

[207] H. E. Albrecht, N. Damaschke, C. Tropea: *Laser Doppler and phase Doppler measurement techniques*: Springer-Verlag, Berlin (2003)

[208] J. C. Wheeler: Modified moments and Gaussian quadratures. *Rocky Mountain Journal of Mathematics*, **4**, 287–296 (1974)

[209] S. R. Gopireddy, R. M. Humza, E. Gutheil: Modeling and simulation of water and PVP/water evaporating spray flows using the direct quadrature method of moments. *Atomization and Sprays*, submitted (2013)

[210] Aa. Fredenslund, R. L. Jones, J. M. Prausnitz: Group-contribution estimation of activity coefficients in non-ideal liquid mixtures. *AIChE Journal*, **21**, 1086–1099 (1975)

[211] T. Oishi, J. M. Prausnitz: Estimation of solvent activities in polymer solutions using a group-contribution method. *Industrial & Engineering Chemistry Process Design and Development*, **17(3)**, 333–339 (1978)

[212] D. C. Kannan, J. L. Duda, R. P. Danner: A free-volume term based on the van der Waals partition function for the UNIFAC model. *Fluid Phase Equilibria*, **228-229**, 321–328 (2005)

[213] A. Correa, J. F. Comesana, A. M. Sereno: Use of analytical solutions of groups (ASOG) contribution method to predict water activity in solutions of sugars, polyols and urea. *International Journal of Food Science and Technology*, **29(3)**, 331–338 (1994)

[214] A. Striolo, J. M. Prausnitz: Vapor-liquid equilibria for some concentrated aqueous polymer solutions. *Polymer*, **41**, 1109–1117 (2000)

[215] A. Bondi: *Physical properties of molecular crystal, liquids and glasses.*, New York: Wiley (1968)

[216] R. P. Danner, M. S. High: *Handbook of polymer solution thermodynamics*: DIPPR Project, AIChE, New York (1993)

[217] T. E. Daubert, R. P. Danner: *Data compilation of properties of pure compounds*: DIPPR Project, AIChE, New York (1992)

[218] A. Kleinhans: Personal communication (2012)

[219] E. Littringer, M. Koester, N. Urbanetz: Personal communication (2012)

[220] A. Z. Dakroury, M. B. S. Osman, A. W. A. El-Sharkawy: Properties of solutions of polyvinylpyrrolidone. *International Journal Thermophysics*, **11**, 515–523 (1990)

[221] Z. A. Metaxiotou, S. G. Nychas: Experimental measurement of diffusion in aqueous polyvinylpyrrolidone solutions. *AIChE Journal*, **41**, 812–818 (1995)

[222] I. S. Grigoriev, E. Z. Meylikhov: *Physical values handbook*: EnergoAtomIzdat, Moscow (1991)

[223] G. L. Hubbard, V. E. Denny, A. F. Mills: Droplet evaporation: Effects of transients and variable properties. *International Journal of Heat and Mass Transfer*, **18**, 1003–1008 (1975)

[224] R. Sedelmayer, M. Griesing, A. Halfar, H.-U. Moritz: Personal communication (2012)

[225] S. R. Gopireddy, E. Gutheil: Numerical investigation of PVP/water spray flows in an Eulerian framework. *25th European Conference on Liquid Atomization and Spray Systems (ILASS)*, 1–7, September 1–4, Chania, Greece (2013)

[226] S. R. Gopireddy, K. Martin, E. Littringer, A. Mescher, P. Walzel, N. Urbanetz, E. Gutheil: Numerical and experimental study mannitol/water droplet evaporation and drying. *25th European Conference on Liquid Atomization and Spray Systems (ILASS)*, 1–7, September 1–4, Chania, Greece (2013)

[227] S. Ghosh, J. C. R. Hunt: Induced air velocity within droplet driven sprays. *Proceedings of Royal Society London*, **A 444**, 105–127 (1994)

[228] A. C. S. B. Silva, J. A. B. Cunha Neto, R. Lamberts: Modelling spray vaporization for evaporative cooling of buildings. *Building Services Engineering Research and Technology*, **25(4)**, 351–361 (2004)